Active Stabilisation of Buckling in Composite Laminates

Jared P. Welham

A thesis submitted in partial fulfilment
of the requirements for the degree of
Master of Engineering
in
Mechanical Engineering
at the
University of Canterbury,
Christchurch, New Zealand.

25 January 2004

Abstract

The active suppression of elastic buckling has the potential to significantly increase the effective strength of thin-wall structures. Despite all the interest in smart structures, the active suppression of buckling has received comparatively little attention. This research further develops analytical and experimental techniques for the optimal control of columns and plates using piezo-ceramic actuators. Previous work in this area has included numerous theoretical studies and a very limited number of experiments.

Numerical models are formulated to simulate both the structure and its active control system. The inclusion of mixed continuous-discrete control simulations for active laminate design is unique to this research and provides insight into issues that arise when trying to implement a continuous control strategy for this unstable system with a discrete controller subject to sensor and noise error. Therefore, limitations such as sensor uncertainty and noise, actuator saturation and control architecture are included in the model. Three active plate strips and a pneumatic compression loading system are implemented based on simulation results and optimal controller design, to command the structure to deform in ways that interfere with the development of buckling mode shapes. Due to the importance of early detection, the relative effectiveness of active buckling control is shown to be strongly dependent on the performance of the sensing scheme, as well as on structure specific characteristics.

Initial experiments highlight the difficulties involved in obtaining ideal buck-

ling behaviour in a practical environment. Correction of initial curvature in laminates is successfully implemented, resulting in buckling curves closely resembling finite element results. Active control is combined with the constant actuator offset required to correct for initial curvature to obtain further gains in effective strength.

Current experimental results show a 37% increase in the measured buckling load from 2.1 to 2.9 kN and simulations indicate that the controlled critical load can be further increased given higher actuator authority. These results are significant because they stabilise a structure approximately 30 times stiffer than in any other published results, where this high stiffness has introduced additional difficulties mainly due to the faster dynamics of the structure. They are also the first known experimental results to successfully stabilise an active laminate plate structure.

Acknowledgements

There are numerous people whom I would like to thank for their valuable support during the course of this research. First, to my supervisors; Dr J. Geoffrey Chase who has provided substantial support and expertise and Dr Emilio Calius who has always been on hand to answer all of my questions. Without their time and effort this project would not have been successful. The financial support of Industrial Research Ltd. has been greatly appreciated and I would like to thank Graeme Finch who was instrumental in organising this funding, and for providing open access to resources. Andy Skeates and Jonathan Bergh have both made contributions to the experimental part of this research with their time and advice. Also, thanks to Mark Carey for his effort and programming skills during the coding of the finite element model. Thanks are also extended to Dr Thomas Sors for his time and contributions on the examining committee.

Contents

List of Figures

List of Tables

Nomenclature

A	state space plant matrix
a	length of element
B_1	state space control mapping matrix
b	width of element
C	element damping matrix
C_1	measurement mapping matrix
$C_{1:11}$	proportional portion of measurement mapping
$C_{1:22}$	derivative portion of measurement mapping
D	control mapping matrix
D_{bend}	material flexural stiffness matrix
E	material stiffness / modulus
F	blocked actuator force
F_S	discrete sampling rate
G	control gain matrix
G_x,G_y	material shear stiffness / modulus
G_1	proportional portion of control gain matrix
G_2	derivative portion of control gain matrix
I	second moment of area
K	structural stiffness matrix
K_G	geometric stiffness matrix
K_{Tot}	combined stiffness matrix

l	length of plate
M	element mass matrix
M	blocked actuator moment
$\overline{M}$	blocked actuator moment per node
N	elemental shape functions
P	compressive load magnitude
S	material compliance matrix
t	laminate thickness
T_S	discrete sample period
U	translational degrees of freedom
v	physical deflections
w	width of plate
X	state space vector containing variables
x	vector of physical displacements and rotations
Y	state space measured output vector
y	physical measured output vector
ε	plane strain
λ	vector of eigenvalues
γ	shear strain
ν	Poison's ratio
Φ	vibration mode shapes used for contraction
ρ	material density
θ	rotational degrees of freedom

Annotations:

$\overline{A}$	contracted modal coordinate system
A'	matrix transose
$\dot{A}$	differential
$\ddot{A}$	second differential
A^{-1}	matrix inverse
$\hat{A}$	equivalent flexural properties

Subscripts:

A_x,A_y	plate coordinate system
A_1,A_2	ply or material coordinate system
A_ξ,A_η	normalised isoparametric coordinate system
A_G	global finite element matrix
A_{CL}	closed-loop
A_{CR}	critical

Abbreviations

CLT	classical laminate theory
CL1	critical buckling load (mode 1)
CL2	critical buckling load (mode 2)
CL3	critical buckling load (mode 3)
CR	control ratio
CSM	chopped strand mat
DOF	degree of freedom
FEA	finite element analysis
FEM	finite element model
FIR	finite impulse response
IIR	infinite impulse response
LMI	linear matrix inequality
OOP	out-of-plane
PZT	lead zirconate titanate
SMA	shape memory alloy
SNR	signal-to-noise ratio
ZOH	zero-order hold

Chapter 1

Introduction

The quest for structural efficiency, cost-effectiveness and high performance is leading to increasing use of thinner, more slender structures in applications ranging from micro-machines to civil engineering as developments in materials, manufacturing methods, and analytical knowledge make it possible. At the same time, many of these structures must withstand significant compression and shear loads. Examples include aircraft wing and control surface skins, boat hulls and yacht masts, and cable-stayed bridges. There are further important opportunities for slender structures at the micro-scale, involving micromechanical devices for use in fields from telecommunications equipment to micro-fluidic and biomedical devices.

Thin, slender structures have additional failure modes beyond those that result from material yielding, cracking and fracture, and these involve the geometrical instability known as buckling. Since the compression buckling strength is often but a fraction of the material strength, this can be an important limitation. The development of buckling instabilities involves small lateral deflections early on, but these grow quickly. Relatively small moments and deformations are required to bring the structure back into alignment, provided that action is taken quickly enough. This makes buckling suppression a suitable application for smart structures technology, as the limited authority available from conventional

actuator materials, such as Lead Zirconate Titanate (PZT) piezoceramics, can be leveraged to have a substantial impact on effective structural strength.

This thesis contains a detailed account of modelling, design and construction of an active laminate, the design and simulation of an active buckling controller, and validation experiments that were performed in the laboratory.

Chapters 2 and 3 provide an overview of the buckling phenomenon and prior research work in this topic. Chapter 4 considers the design and optimisation of an active laminate plate. The important characteristics are discussed and a final plate design is specified to maximise the performance of active buckling control. Chapter 5 discusses the generation of a finite element model, and provides results for linear and nonlinear analysis of the final laminate plate design in the absence of control. The design and optimisation of the controller is discussed in Chapter 6, while the results from numerous simulations of active buckling control are presented in Chapter 7.

Chapter 8 looks at the construction of three active plate strips and the results from modelling and simulation. These active plate strips were constructed for experimental work and differed from the laminate plate designed in Chapter 4 primarily in their reduced width and reduced number of sensors and actuators. This simpler structure was considered to be an essential stepping stone to experimentation with a more complex fully constrained plate. Hardware and loading issues were explored using this simple structure and discrepancies with modelling and simulation assumptions were identified. The design of an experimental loading rig and associated hardware and sensors is explained in detail through Chapter 9. Chapter 10 presents the results from testing the three active plate strips and discusses experimental issues that arose during this section of work. Chapters 11 and 12 draw conclusions from the research and consider the direction of future work in this area.

Chapter 2

The buckling phenomenon

Uniaxial buckling of plates occurs when the flexural stiffness of a structure is reduced through the application of a compressive load. When this load reaches the buckling load the effective flexural stiffness becomes zero and buckling will occur given the smallest perturbation.

Buckling plays a large part in the design of thin members and plate structures. Examples of such structures are aeroplane wings, missiles and yacht masts. When designing these structures the material and geometry choices are often dictated by the buckling load, which is often much lower than the loads required for material failure. Therefore, if it is possible to control the buckling phenomenon, then structures could be designed thinner giving a reduction in both weight and material usage.

2.1 Linear buckling theory

Although buckling is an essentially nonlinear process, the equilibrium equations can be linearised near the buckling point and linear control principles applied to the problem. The following eigenvalue equation is the basis for linear buckling theory:

$$[K - \lambda K_G]\ v = 0 \tag{2.1}$$

where K is the material stiffness matrix and K_G is the geometric stiffness matrix. λ is the linear buckling eigenvalue, which corresponds to a positive compressive loading per unit width (P_{CR}) and v is the eigenvector that defines the mode shape corresponding to that critical load. While this first order formulation is not exact, it captures the majority of dynamics necessary for control of fundamental buckling. For any given compressive load (P) the total stiffness (K_{Tot}) can be written:

$$K_{Tot} = K - P\,K_G \tag{2.2}$$

which will become singular if P equals one of the buckling eigenvalues (λ).

Chapter 3

History and prior work

Given the extensive research and publication activity in active control and suppression of sound and structural vibration, it is surprising to note that until recently relatively little attention has been paid to the related topic of active control and suppression of buckling [1, 2, 3, 4, 5, 6, 7]. Most published research on the buckling of structures containing piezoelectric or shape memory alloy (SMA) material consists of theoretical studies. For example, Sun [8] addressed the theory of linear buckling in piezoelectric structures in terms of general tensor equations, and established a fundamental mathematical basis for active stabilisation, but made no predictions directly applicable to plates. All of the active buckling suppression experiments that have been reported in the literature [9, 10, 11, 12, 13, 14, 15] have been carried out on beam strips. In Thompson's experiments on plates the embedded SMA wires were activated only after the test specimen had buckled, rather than to prevent or delay buckling [6].

Berlin [9, 10] demonstrated experimentally that surface bonded 0.25mm thick PZT ceramic patches can be used to actively stabilise a simply supported 300mm tall thin steel strip under axial compression. By actively suppressing both its first and second column buckling modes, the critical load was increased by a factor of up to 5.6 for short periods of time. However, the required control gains had to be developed empirically through manual adjustments. In later work Chase

et al. [13, 14, 15] developed a control design methodology that optimises the gains based on the linear buckling eigenvalues. Using this optimal control design technique, a critical load of 2.94 times the passive buckling load P_{CR} was achieved experimentally for a 457mm long strip of 2.36mm thick fiberglass laminated with longitudinal PZT active fiber composite actuators on both surfaces. Although lower than that achieved by Berlin, probably due to vibrations in the loading mechanism, the $2.9P_{CR}$ load could be sustained indefinitely. In both these tests, the active material covered most of the strip surface. Thompson (S.P.) and Loughlan's experiment [12] measured the increased stability under axial compression of 3 column strips with a single pair of surface bonded 0.19mm thick PZT ceramic wafer patches that covered only some 14% of the strip surface. Depending on the specimen's layup, actively countering lateral deflection increased the buckling load by 20% to 37%, although only in the last case was the specimen able to exceed its theoretical linear buckling load. In this example, much of the gains were achieved by actively compensating for the imperfections and misalignments that can severely curtail real buckling loads, and thus allowing an imperfect structure to approach its theoretical limits.

There have been a number of theoretical studies of the active buckling control of flat plates. In one of the first such studies, Thompson (D.M.) and Griffin [16] concluded from their finite element analysis that pairs of widely spaced SMA wires increased the buckling load of 2.54mm thick stiffened aluminum panels by up to 12%. Although small, these increases were significant in relation to the low fraction of active material deployed. More complete studies of the mechanics of SMA wire stiffening in plates were later carried out by Ro and Baz [17, 18], and Birman [19]. However, although using SMA based actuation is advantageous because of their high induced force capabilities, their main limitation besides their slow response time, is that they can only provide compressive forces. As a result, SMA based buckling stiffening concepts rely on anchor points external to the

structure and the sliding of SMA wires in tubes embedded along the mid-surface, which would be of limited practicality for most real-world applications. In other early work, Chandrashekhara & Bhatia [20] presented one of the first studies based on piezoceramic (PZT) actuators, although their results predicted a rather modest increase in the critical buckling load of less than 5%. More recently, Batra and Geng [4] investigated small, square composite plates with PZT patches that covered most of the surface. In their simulations, the application of a uniform voltage proportional to the central lateral deflection of the plate enhanced the dynamic buckling load by less than 1% for plates with a thickness between 2 and 3mm, although higher values were obtained when the plate thickness was reduced so that it approached the PZT patch thickness. Much more important improvements were achieved by Chase and coworkers [2, 3, 21] by extending their optimal control design method to the two dimensional plate buckling case. As a result of their simulations of active stabilisation of 2.54mm thick composite plates using PZT patches, the buckling strength of a square plate was increased by 51%; while that of a rectangular plate, which was loaded parallel to its longest side, was raised by 62% [21]. Under combined axial and shear loading, the square plate's buckling strength was raised by 50% [2, 3].

Chapter 4

Active laminate design and optimisation

The goal of this research was to design and build an active laminate, which would display increased compressive strength over an equivalent passive specimen. Before the control system was designed it was necessary to design a composite laminate specifically tailored to this application. This laminate design dictated the success of the experiments given practical limits such as actuator numbers, size and authority, and also limitations on the compressive loading rig used for testing.

4.1 Properties of an ideal experimental laminate

The laminate was designed to maximise the effectiveness of the experiment, while keeping the total forces to a manageable level for experimental work. The actuators, which have a relatively high stiffness, were embedded in the plate laminate to ensure a constant flexural stiffness throughout the plate. If the actuators were mounted on the surface they would increase the stiffness in that area, which could subsequently change the dynamic and buckling characteristics of the specimen.

Important characteristics of experimental plate design:

1. Low buckling load; defines the type and size of the loading rig

2. High control ratio; a measure of the ability to control the plate

3. Practical plate dimensions; suitable size for manufacture and testing

4.2 Actuators

The plate was designed with actuation in mind. The limited actuation force provided by commercially available Lead Zirconate Titanate (PZT) strain actuators requires careful design of the plate to make best use of the available force. Buckling modes such as those shown in Figure 5.4 can be suppressed by generating restoring bending moments using the combined action of a pair of actuators operating out of phase, as illustrated in Figure 4.1.

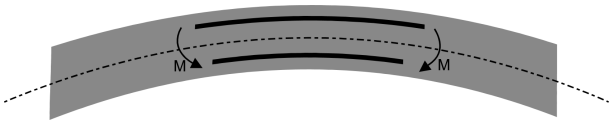

Figure 4.1 Schematic of restoring moment produced by a pair of actuators embedded in the plate.

The modelled actuators were ACX Quickpack® QP10 actuators. Simple calculations utilising blocking force were used to provide an estimation of the maximum control authority. Blocking force calculations estimate the force generated by an actuator from the consideration of an internal induced strain and the mechanical properties of the actuator. It was assumed that this actuator was bonded to a surface that could resist the applied force, as free expansion will not generate a force in the plate.

The actuators are much stiffer than the composite plate material, and therefore needed to be embedded to achieve a uniform flexural stiffness over the plate. A uniform flexural stiffness requires the value of EI to remain constant over the entire plate. A routine was written to determine the correct actuator embedding depth to maintain a uniform flexural stiffness equal to that of the passive plate.

Figure 4.3 shows the results of this analysis given a plate stiffness of 15GPa, an actuator stiffness of 60GPa and PZT wafer thickness of 0.381mm.

4.3 The control ratio: a performance estimate

The control ratio (CR), which is a function of sensor resolution and actuator authority, is a useful estimate of the closed-loop performance of the active laminate system.

$$CR = \frac{MaximumActuatorDeflection}{MinimumDetectableDeflection} \tag{4.1}$$

A larger control ratio will increase the ability to control a certain system. From experience, a control ratio over ten is desirable [15]. The control ratio was used to assess the performance of the system considering the dependencies on geometry, actuator location, and material properties. The control ratio can also be thought of as the number of sensing increments available before the control system does not have the authority to return it to equilibrium.

4.4 Discussion of optimisation variables

4.4.1 Laminate thickness

Increasing the laminate thickness would also increase the required buckling loads. An upper limit of 5kN was considered to be manageable under experimental conditions, which imposed a limit on laminate thickness. As seen in Tables 4.1 and 4.2 reducing the plate thickness from 3mm to 2mm (case h to j) would reduce the critical load from 11.5 to 3.4kN/m, which was desirable considering the loading mechanism design, but outweighed by the inability to achieve constant flexural stiffness by embedding actuators.

Table 4.1 Effect of laminate thickness on the lowest 3 eigenvalue buckling loads for a range of laminate stiffnesses. **Max** ε_X is a measure of the maximum strain for a normalised OOP deflection.

	t mm	E_X **GPa**	E_Y **GPa**	v_{xy}	v_{yx}	**CL1** N/m	**Max** ε_X ε	**CL2** N/m	**CL3** N/m
a	6	15	5	0.27	0.09	92195	0.0249	122282	205830
b	6	60	20	0.27	0.09	300757	0.0249	422496	759722
c	4	15	5	0.27	0.09	27317	0.0166	36232	60987
d	4	30	10	0.27	0.09	47911	0.0166	65845	115589
e	4	48	16	0.27	0.09	72631	0.0166	101439	181271
f	4	60	20	0.27	0.09	89113	0.0166	125184	225103
g	4	100	33.3	0.3	0.009	144014	0.0166	204353	371296
h	3	15	5	0.27	0.09	11524	0.0125	15285	25729
i	3	60	20	0.27	0.09	37595	0.0125	52812	94965
j	2	15	5	0.27	0.09	3415	0.0083	4529	7623
k	2	60	20	0.27	0.09	11139	0.0083	15648	28138

Table 4.2 Effect of laminate thickness on actuator embedding distance, maximum actuated deflection and control ratio using a single pair of PZT actuators.

	t mm	E_X **GPa**	**Embedded Distance** mm	M_Y **Nm**	$\overline{M}_Y$ **Nm/node**	M_X **Nm**	$\overline{M}_X$ **Nm/node**	**Min Detect Deflection** mm	**Max Actuated Deflection** mm	**Control Ratio**
a	6	15	1.120	0.477	0.079	0.953	0.087	0.0384	0.0742	1.93
b	6	60	0.381	0.664	0.111	1.328	0.121	0.0384	0.0324	0.84
c	4	15	1.000	0.254	0.042	0.507	0.046	0.0577	0.1330	2.31
d	4	30	0.654	0.341	0.057	0.682	0.062	0.0576	0.1030	1.79
e	4	48	0.458	0.391	0.065	0.782	0.071	0.0576	0.0785	1.36
f	4	60	0.381	0.411	0.068	0.821	0.075	0.0576	0.0676	1.17
g	4	100	0.246	0.445	0.074	0.889	0.081	0.0576	0.0456	0.79
h	3	15	0.920	0.147	0.025	0.294	0.027	0.0766	0.1850	2.42
i	3	60	0.381	0.284	0.047	0.567	0.052	0.0765	0.1110	1.45
j	2	15	0.810	0.048	0.008	0.096	0.009	0.1153	0.2060	1.79
k	2	60	0.381	0.157	0.026	0.314	0.029	0.1152	0.2080	1.81

As deflection due to buckling was measured using pairs of strain gauges, increasing the plate thickness improved the minimum detectable displacement as a thicker laminate provided larger bending strains at the surface (Figure 4.2). A final effect of increasing laminate thickness was that the actuators would need to be embedded deeper into the laminate. More important was the moment arm (distance between embedded actuators), which is a function of embedding depth and plate thickness, as see in Figure 4.3.

4.4.2 Material properties

During the laminate optimisation stage and early finite element analysis the plate model was based on an orthotropic material. This reduced the number of optimisation variables, as otherwise it would have been necessary to specify individual plies. After an optimal solution was found for the orthotropic material, a laminate

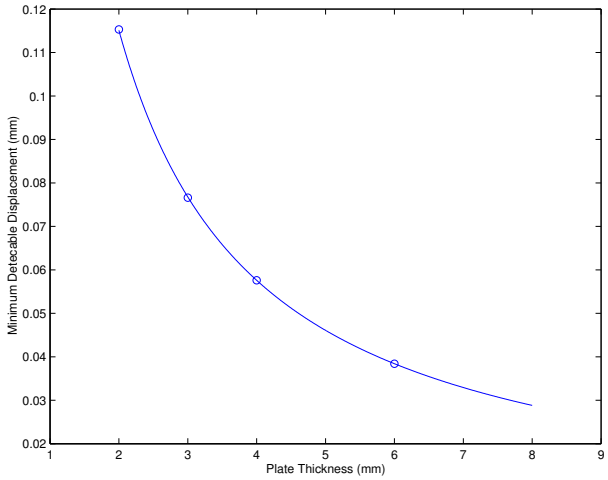

Figure 4.2 Minimum detectable displacement based on expected resolution of strain gauges.

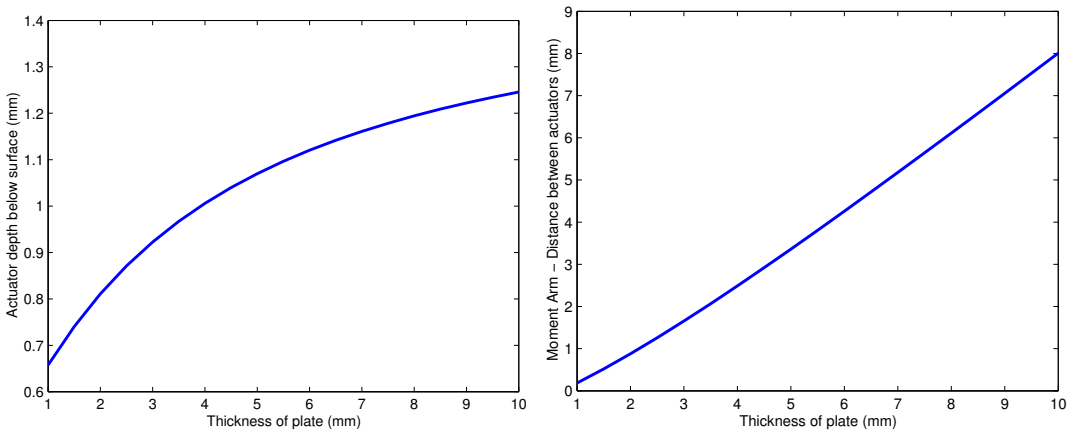

Figure 4.3 Embedded depth for constant flexural stiffness and resulting moment arm for a pair of actuators.

would be designed to match this definition. The material stiffness also affected the embedding distance of the actuators. The lower the stiffness of the plate, the greater the embedding distance required to obtain an equivalent bending stiffness due to the high relative stiffness of the PZT actuators. This increased depth results in a reduced moment arm, and therefore lowers control authority.

Table 4.3 shows the effect of different ratios of E_X to E_Y. Considering the results shown in this table it is apparent that the fundamental buckling load is more influenced by the lower stiffness. Figure 4.4 shows a graph of these same results, where it is easier to see the effect of the moduli ratio on the difference between buckling modes one to three. As the control is anticipated to correct the lowest two buckling modes, the ideal controlled case would fail at the third buckling load. Therefore, a large ratio between modes one and three will provide a larger percentage increase of buckling strength due to active control.

It was also observed that in the cases where the ratio of $\frac{E_x}{E_Y}$ was reduced to less than 1 (i.e. stiffer in the transverse direction), the resulting first mode shape changed from a half to a whole sine wave. This shape results in lower strains, which reduce the minimum detectable out-of-plane displacement by approximately 65%. This change would also make actuation more difficult as more locations would be required to actuate this higher order mode.

Table 4.3 Effect of laminate moduli ratio on eigenvalue buckling loads.

	Material Properties						Ansys Buckling				
Case	E_1/E_2	E_1 GPa	E_2 GPa	G_{12} GPa	v_{12}	v_{21}	**CL1** N/m	**CL2** N/m	**CL3** N/m	**CL2/CL1**	**CL3/CL1**
a	5	15	3	3	0.27	0.054	10157	14621	24988	1.44	2.46
b	4	15	3.75	3	0.27	0.0675	10669	14867	25258	1.39	2.37
c	3	15	5	3	0.27	0.09	11524	15285	25728	1.33	2.23
d	2	15	7.5	3	0.27	0.135	13237	16142	26728	1.22	2.02
e	1	15	15	3	0.27	0.27	18319	18855	30200	1.03	1.65
f	0.50	7.5	15	3	0.135	0.27	11707	12895	18301	1.10	1.56
g	0.33	5	15	3	0.09	0.27	9418	10425	14976	1.11	1.59
h	0.25	3.75	15	3	0.0675	0.27	8281	8963	12372	1.08	1.49
I	0.20	3	15	3	0.054	0.27	7595	8021	10644	1.06	1.40

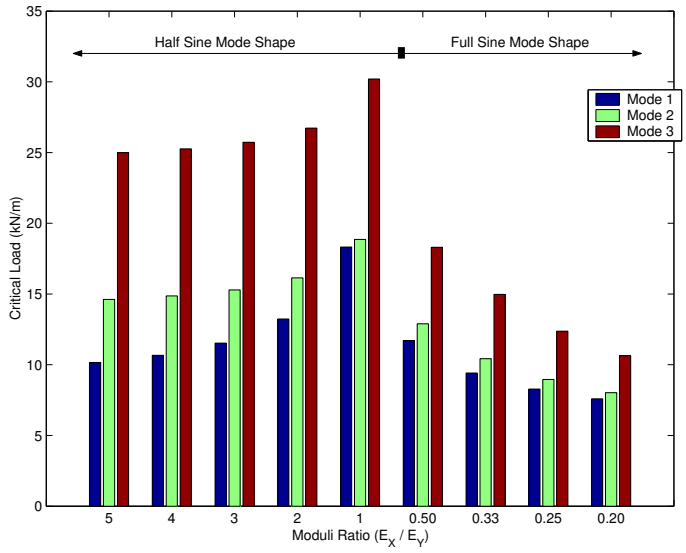

Figure 4.4 The effect of moduli ratio on critical load and shape. Loaded edges were fixed and other edges simply supported.

4.4.3 Plate dimensions

An initial plate size of 300 x 500 mm was used for the optimisation procedure. Both the plate dimensions, and material stiffness combine to determine the buckling and vibration mode shapes. The effect of increasing the width of the plate to 500 by 500 mm (i.e. a square plate) can be seen in Table 4.4. This is quite a large width increase and decreases the buckling load approximately 30%. The trade off is that by increasing the plate area by almost 70%, more actuators would be required to cover a similar proportion of the plate. Another potential concern is that the plate becomes more difficult to manage in a practical sense at these larger sizes.

As shown in Tables 4.5 and 4.6 by reducing the plate dimensions to 200 by 300 mm the required buckling load will increase, as will the control ratio. As the number of available actuators is limited, reducing the dimensions of the plate will result in a larger percentage of the plate surface area covered with actuators. In this analysis $E_X = 3GPa$ and $E_Y = 15GPa$. Results are given for this smaller plate for both 3 and 4 mm thicknesses. The buckling load for the 3mm

Table 4.4 Effect of increasing laminate surface area on fundamental buckling load. Critical buckling loads were evaluated using *Gibbs and Cox* method.

	E_1	E_2	G_{12}	**t**	v_{12}	v_{21}	**300 by 500 mm CL1**		**500 by 500 mm CL1**		**Reduction of CL1**
	GPa	GPa	GPa	mm			N/m	N	N/m	N	%
a	15	15	3	3	0.27	0.27	19119	5735.7	8669	4334.5	24.4
b	15	5	3	3	0.27	0.09	11285	3385.5	6952	3476	-2.7
c	5	15	3	3	0.09	0.27	10849	3254.7	4648	2324	28.6
d	5	5	3	3	0.27	0.27	8347	2504.1	3600	1800	28.1
e	15	15	3	2	0.27	0.27	5665	1699.5	2568	1284	24.4
f	15	5	3	2	0.27	0.09	3343	1002.9	2060	1030	-2.7
g	5	15	3	2	0.09	0.27	3214	964.2	1377	688.5	28.6
h	5	5	3	2	0.27	0.27	2473	741.9	1066	533	28.2

plate has increased to 5.5kN compared to 3.5kN in the 300 by 500 mm plate. The fourteen actuators on this smaller plate cover 29% of the surface. To have approximately the same coverage for the larger plate (300 by 500 mm) would require 36 actuators.

Table 4.5 Buckling Loads for smaller laminate of dimensions 200 by 300mm.

	t	**CL1**		**Max ε_X**	**CL2**	**CL3**
	mm	**N/m**	**N**	ϵ	**N/m**	**N/m**
l	4	65512	13102.4	0.0297	94454	163295
m	3	27638	5527.6	0.0223	39848	68890

Table 4.6 Performance of control for smaller laminate of dimensions 200 by 300mm.

	t	**Embedded Distance**	$\overline{M}$	**Min Detect Deflection**	**Max Actuated Deflection**	**Control Ratio**
	mm	**mm**	**Nm/node**	**m**	**m**	
l	4	1.00	0.0442	2.152E-05	6.150E-04	28.6
m	3	0.92	0.0255	2.865E-05	8.410E-04	29.3

4.4.4 Location of actuators

The optimum location and number of actuators was considered and simulated for a number of configurations. Different configurations were compared using the resulting maximum out-of-plane deflection found using a static finite element analysis. Little performance difference was found between having a large number of actuators covering the majority of the plate surface, or a few actuators carefully located to fit mode shapes. The best actuator locations were places of high strain for mode shapes where actuation was desired. Finally, a configuration was

required to be able to actuate both the first and second buckling modes.

4.4.5 Example of control ratio calculation

It was assumed that $10\mu\varepsilon$ is the minimum detectable strain given experience with ambient noise levels in experimental strain gauge signals. The maximum actuator authority was determined by a static analysis using Ansys®. Assuming the strain gauges are located at the point of maximum strain, $10\mu\varepsilon$ correlates to a central out-of-plane (OOP) deflection of $62\mu m$.

A pair of ACX QP10N actuators can produce a maximum in-plane strain of $262\mu\varepsilon$ in both x and y directions. Blocked force and moment for a pair of embedded actuators located 0.58mm from center plane of the laminate was calculated:

$$F_X = 126.8N \quad M_Y = 0.147Nm$$
$$F_Y = 253.5N \quad M_X = 0.294Nm$$

Solving a static finite element analysis using the blocked moments found for a single pair of actuators located in the center of the plate it was possible to determine a central OOP deflection of 0.094 mm. Therefore, the control ratio was defined:

$$\text{Control Ratio} = \frac{0.94E{-}4}{62E{-}6} = 1.52$$

Calculations using fourteen actuators showed that it was possible to increase the control ratio to 8.31.

4.5 Alternative actuators

Alternative actuators have recently become available. PZN-PT actuators can produce larger strains than the PZT actuators but have a lower stiffness of 15

GPa. This lower modulus better matches the stiffness of the laminate and therefore would not have to be embedded as much. The blocking force is also reduced by the lower actuator stiffness. If it is assumed that these actuators can produce an in-plane strain of $4000\mu\varepsilon$, and are 50 x 25 x 0.5 mm, then the blocking moment for a 3mm thick plate with actuators embedded 0.5mm is defined:

$$F_X = 750N \qquad M_Y = 1.5Nm$$
$$F_Y = 1500N \qquad M_X = 3Nm$$

The maximum resulting deflection was found using Ansys® and compared to that obtained for the PZT actuators. The PNZ-PT actuators create a deflection approximately ten times that of the PZT actuators. This value results in the same increase to the control ratio. One of the major reasons for this substantial increase is that the PZN-PT actuators do not need to be embedded nearly as far into the laminate, due to their lower modulus, and therefore have a larger moment arm.

4.6 Summary of optimisation results

Figures 4.3 and 4.2 showed that there were several factors related to the plate thickness that affected the control ratio. These effects combine to form a complex relationship, which can be seen in Figure 4.5. This plot shows that a relatively thick plate is more desirable for this specific control problem.

In summary, it is desirable to use the thickest, most flexible plate possible. However, there is a limit to the compression force that can be easily be generated in the laboratory therefore limiting the allowable stiffness and thickness of the laminate. It is considered that 7kN for the first mode is an achievable limit for a laboratory experimental rig. This value would require an available compression force of approximately 16kN to load the plate up to the third mode critical load, assuming the first two modes are successfully controlled.

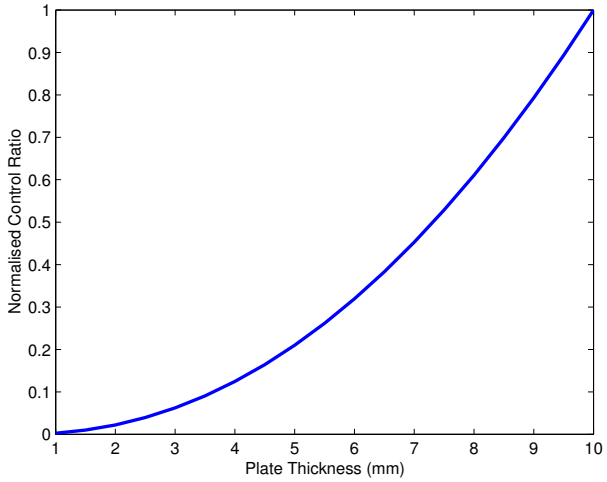

Figure 4.5 The combination of minimum detectable deflection and moment arm to show the effect of plate thickness on control ratio.

Figure 4.6 shows a representation of the plate design space. There are three limits shown on the plot, along with the specifications of the chosen plate and an indication of control ratio relationship. The following limits are illustrated:

1. It is not possible to manufacture a composite laminate with an equivalent flexural stiffness lower than 5 GPa. Given the desired 3:1 ratio between E_x and E_y this sets a lower limit of 15 GPa on E_x.
2. The lower limit on plate thickness occurs when the thickness of material between embedded actuators reaches less than 0.5mm. It is deemed that below this value the plate will become impractical to manufacture and prone to failure at the location of embedded actuators.
3. The upper limit on the thickness is determined by the buckling load becoming too large and therefore unmanageable in a laboratory environment. Considering the size and availability of pneumatic actuators it was necessary to impose this limit as for a high control ratio a large thickness was required. The limit of 7kN on the first mode results in approximately 16kN being required to buckle into the third mode shape, assuming that the goal of controlling the first two modes is achieved.

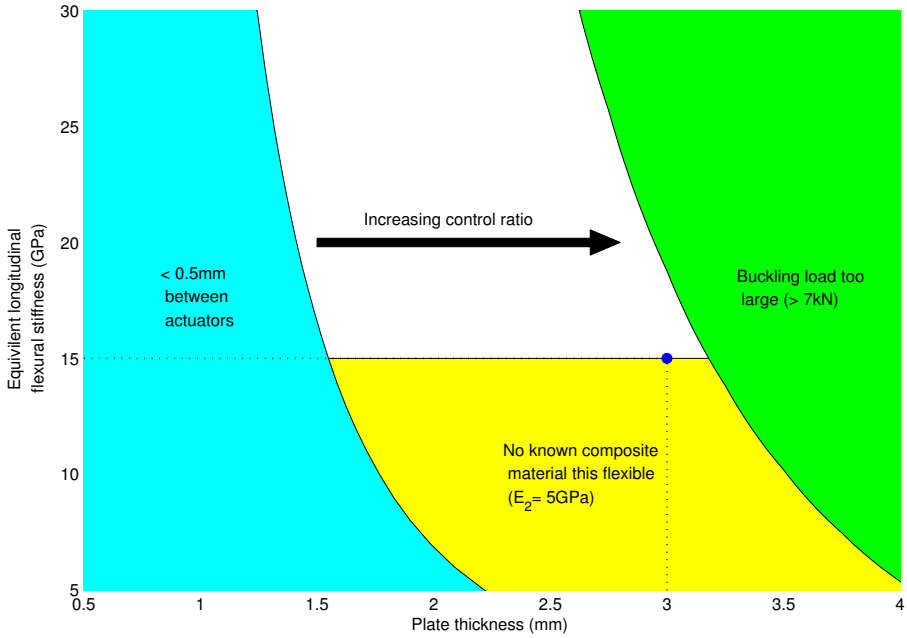

Figure 4.6 Laminate plate design space. The chosen plate properties are indicated by a circle at a thickness of 3mm and a stiffness of 15GPa.

Given that the control ratio increases with increasing plate thickness, it is desirable to choose the thickest plate that falls within the allowable design window. The chosen plate is shown on the plot with a thickness of 3mm and a stiffness of 15GPa.

4.7 Optimised plate specifications

Table 4.7 lists the parameters of the optimised laminate plate design. A schematic of the plate and boundary conditions can be seen in Figure 4.7.

Table 4.7 Summary of optimised laminate plate parameters.

Plate Dimensions:	300 by 200 mm
Plate Thickness:	3 mm
Material Properties:	$E_x = 15GPa$, $E_y = 5GPa$, $G_{xy} = 3GPa$
	$\nu_{xy} = 0.27$, $\rho = 1200kg/m^3$
Damping Parameters:	Rayleigh model
	3% of critical at mode 1
	12% of critical at mode 10
Boundary Conditions:	Fixed on two loaded edges
	Simply supported on two unloaded edges

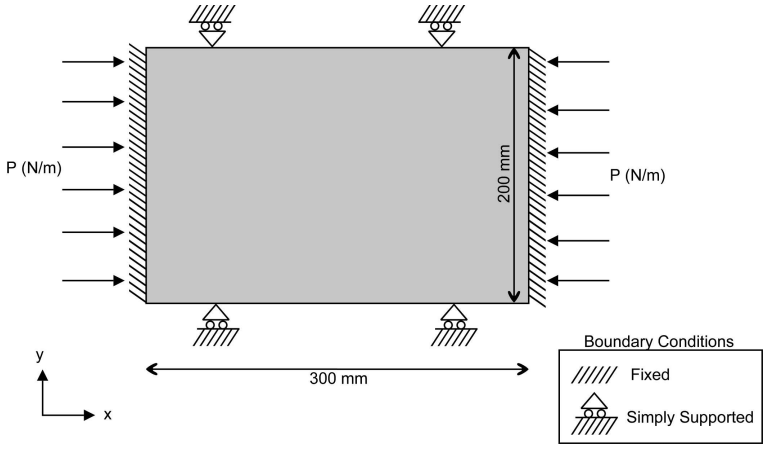

Figure 4.7 Schematic of optimised laminate plate showing boundary conditions and loading orientation.

Chapter 5

Finite element analysis

The first step in developing the optimal feedback controller was to create an accurate finite element model (FEM). The finite element model served two purposes in this research. First, the control system design utilises an optimisation method that is based directly on the FEM for the plant model, sensor location and actuator architecture. Second, it is important to know the mechanical properties of the plate, including expected static deflections, dynamic vibration modes and buckling modes, for experimental design. A displacement based FEM model was created in Matlab®. This model was verified with both a commercial finite element package and classical solutions.

5.1 Model background and theory

For small deflections in flat plates, bending and in-plane deformations are uncoupled and can therefore be considered separately. For this application only the bending degrees of freedom were used, which can describe the flexural behavior important to buckling analysis. The plate was modelled using a four-node, 12 degree of freedom element. The three degrees of freedom (DOF) per node are:

1. U_Z - Out-of-plane translation

2. θ_x - In-plane rotation along x

3. θ_y - In-plane rotation along y

The following assumptions were made to reduce the number of variables in the control design optimisation and the computational size of the global model:

1. The global coordinate system was equivalent to the elemental system. Therefore, no transformation was required.

2. All quad elements were rectangular and of equal dimensions which results in faster model formulation and assembly.

3. Material was approximated to be specially orthotropic so that the material coordinate system is equivalent to that of the elemental system.

4. The material properties and plate thickness were constant throughout the laminate.

5.1.1 Element formulation

The element formulation made use of higher order Hermitian shape functions (Boxer-Fox-Schmit)[21, 22]. Polynomials were bicubic, and Hermite polynomials were first-order:

$$N_1(\xi,\eta) = \left(1 - 3\xi^2 + 2\xi^3\right)\left(1 - 3\eta^2 + 2\eta^3\right) \tag{5.1}$$

where ξ and η are normalised isoparametric coordinates. Several routines for mesh generation and global assembly were adapted from the work of Carey [23]. The mass matrix was consistent, and a two-frequency Rayleigh method was used to create the damping matrix. The Rayleigh damping curve can be seen in Figure 5.1.

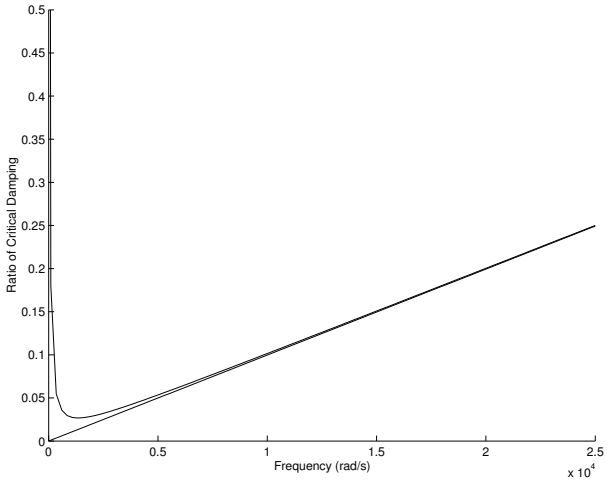

Figure 5.1 Frequency response of Rayleigh damping.

5.1.2 Mesh size and convergence

The element size was dictated by the ability to measure and apply loads to specific local points and small areas rather than being optimised for reduced computation. Figure 5.2 shows the convergence of several static and eigenvalue analyses, with increasing mesh density. For control design the number of elements was not dictated by convergence, but rather more elements than necessary were used to give accurate positioning capability for actuators. Most models used 300-400 elements for a 200 x 300mm plate, for which the convergence error margin was less than 0.5%.

5.2 Material properties

The finite element model used a specially orthotropic definition for material properties and the material compliance matrix (S) is defined:

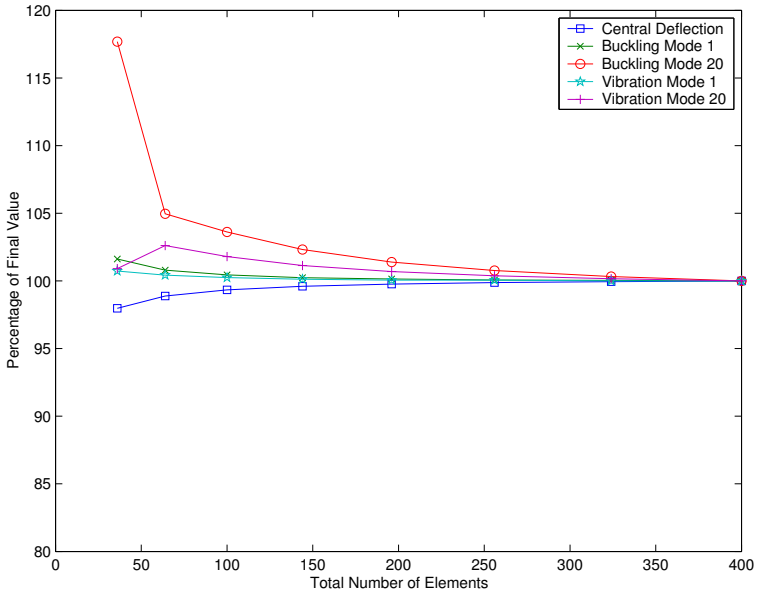

Figure 5.2 Convergence of finite element model.

$$S = \begin{bmatrix} \frac{1}{E_1} & \frac{-v_{21}}{E_2} & 0 \\ \frac{-v_{12}}{E_1} & \frac{1}{E_2} & 0 \\ 0 & 0 & \frac{1}{G_{12}} \end{bmatrix} \tag{5.2}$$

where E is the plane stiffness, G is the shear stiffness and v is Poisons' ratio. Subscripts 1 and 2 refer to both model and laminate longitudinal and transverse orientations as the material is specially orthotropic. The flexural stiffness matrix (D_{bend}) is defined:

$$D_{bend} = \frac{t^3}{12}\left[S^{-1}\right] \tag{5.3}$$

where t is the laminate thickness.

5.3 Model verification

To verify the finite element code a special case was considered so that comparison could be made to both classical analytical solutions and Ansys®. The comparison

included static loading, dynamic vibration modes and buckling modes. The case was a square isotropic plate, fixed on all four edges. The analytical solution was obtained from Roark and Young [24]. Table 5.1 lists the specific model parameters:

Table 5.1 Verification model parameters.

Plate Dimensions:	200mm by 200mm
Plate Thickness:	3mm
Material Properties:	$E = 5GPa, G = 2GPa, \nu = 0.27, \rho = 500kg/m^3$
Damping Parameters:	Rayleigh model
	0.2 % at 1Hz
	0.2 % at 5kHz
Boundary Conditions:	Fixed on all edges
Mesh Size:	400 Elements

For the static loading case an out-of-plane (OOP) load with unit magnitude was applied at the center of the plate. Table 5.2 shows the comparison of results for this static analysis with only minor differences. The frequency and buckling eigenvalues are compared in Table 5.3. The mode shapes were found to be equivalent, and overall buckling loads and eigenfrequencies exhibited good agreement, with differences of only a few percent.

Table 5.2 Results of static comparison.

	Matlab®	Ansys®	Classical
Central Deflection (mm)	0.0179	0.0185	0.0181

Table 5.3 Results of eigenvalue solutions for buckling and free vibration.

	Dynamic Frequency [Hz]		Buckling Load λ [N/m]	
	Matlab®	Ansys®	Matlab®	Ansys®
Mode 1	262	258	29017	27595
Mode 2	554	546	41469	39725
Mode 3	604	596	71092	68565
Mode 4	880	860	87805	82433
Mode 5	1083	1077	95905	91061

5.4 Nonlinear analysis

Nonlinear analysis was performed using Ansys® to verify the eigenvalue analysis and to get an idea of the sensitivity to initial conditions (curvature) of the plate. The reaction forces and deflections were also useful for design of the test rig. A geometrically nonlinear analysis was performed in Ansys®. Load was effectively ramped over time through gradually displacing one end of the supported plate. The central out-of-plane deflection was used to determine the point of buckling. A perturbation is required to initiate buckling in a nonlinear analysis and was applied in the form of a point force at the center of the plate. The magnitude of this force was varied to gain an understanding of the maximum allowable initial curvature that could be present without substantially reducing the buckling load or changing its behaviour.

Figure 5.3 shows an example of the deflection resulting from a ramped load and an initial perturbation of 1N. This force is equivalent to an out-of-plane displacement of 0.024mm at the center of the plate. Eigenvalue analysis for this case predicts a fundamental buckling load of 5.5kN.

Table 5.4 summarises a range of initial perturbations and the resulting load to cause buckling. These results show that for an initial perturbation force in the range of 0.2 to 10N, which corresponds to a central OOP deflection of $4.9\mu m$ to $0.24mm$, the plate will buckle at a load between 4.4 and 5.4kN. This range compares well to the eigenvalue prediction of 5.5kN, which will always be an upper limit to the nonlinear analysis determined practical buckling loads.

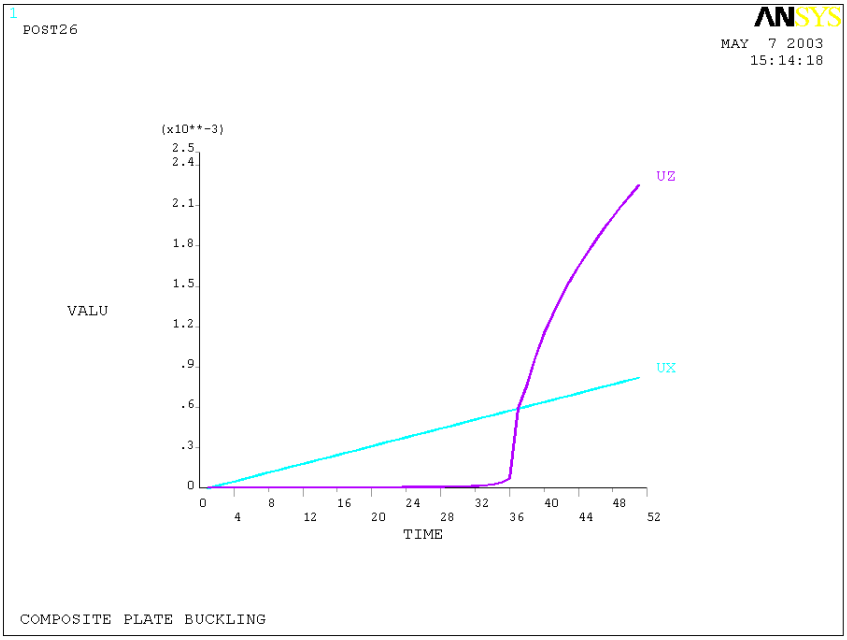

Figure 5.3 Nonlinear results given a central OOP initial perturbation of 1N. UZ refers to the in-plane end deflection, and UX the central OOP deflection.

Table 5.4 Nonlinear buckling analysis results

Central Perturbation Force N	Equiv. UZ mm	Time Step s	Applied Load N	UX (end) mm	UZ (central) mm
0.05	1.2E-05	*Failed to buckle due to perturbation too small*			
0.2	4.87E-03	8	4224.2	0.14	0.017
		9	4827.5	0.16	0.033
		10	5428.4	0.18	0.200
		11	5784.1	0.20	1.400
1	0.024	5	3620.3	0.12	0.065
		6	4524.3	0.15	0.120
		7	5377.6	0.18	0.670
		8	5908.7	0.21	1.800
10	0.24	4	2693.8	0.09	0.440
		5	3576.8	0.12	0.620
		6	4413.2	0.15	0.980
		7	5120.8	0.18	1.600
		8	5690.6	0.21	2.300
100	2.4	*Initial Buckling before application of end load*			

5.5 Results for optimised plate model

The following solution is for the optimised plate model as described in Table 4.7 and Figure 4.7. Figures 5.4 and 5.5 show the first four buckling and free vibration mode shapes respectively. Both the dynamic frequencies and the buckling loads change when feedback control is added to the system. The dynamic frequencies also decrease when the plate is loaded compressively in a similar way that loosening a guitar string causes a decrease in frequency.

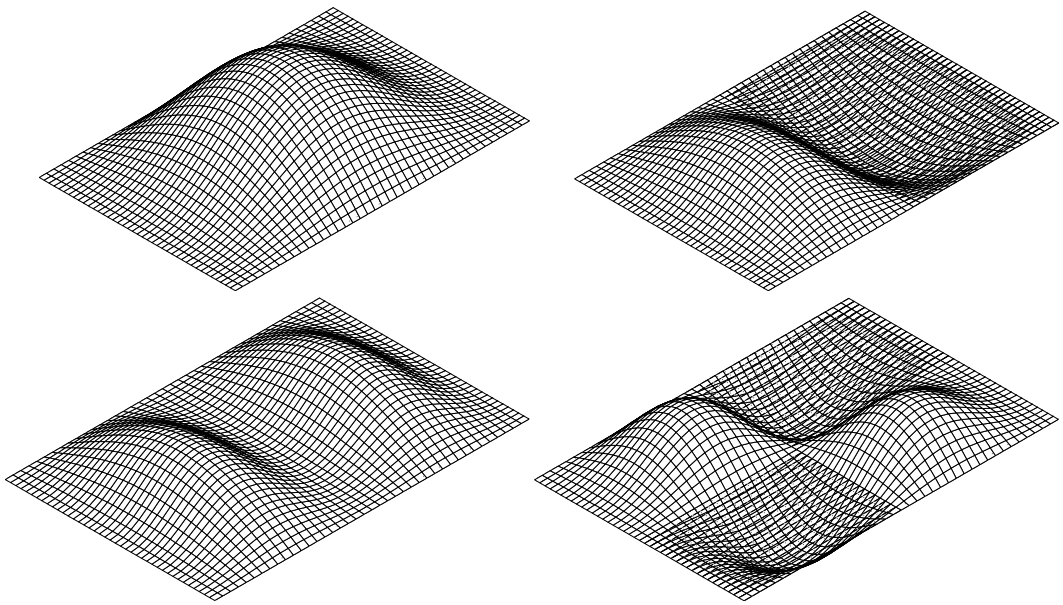

Figure 5.4 The lowest 4 buckling mode shapes computed by finite element analysis. From left to right and top to bottom, these are mode 1 (29 kN/m), mode 2 (41 kN/m), mode 3 (71 kN/m), and mode 4 (88 kN/m)

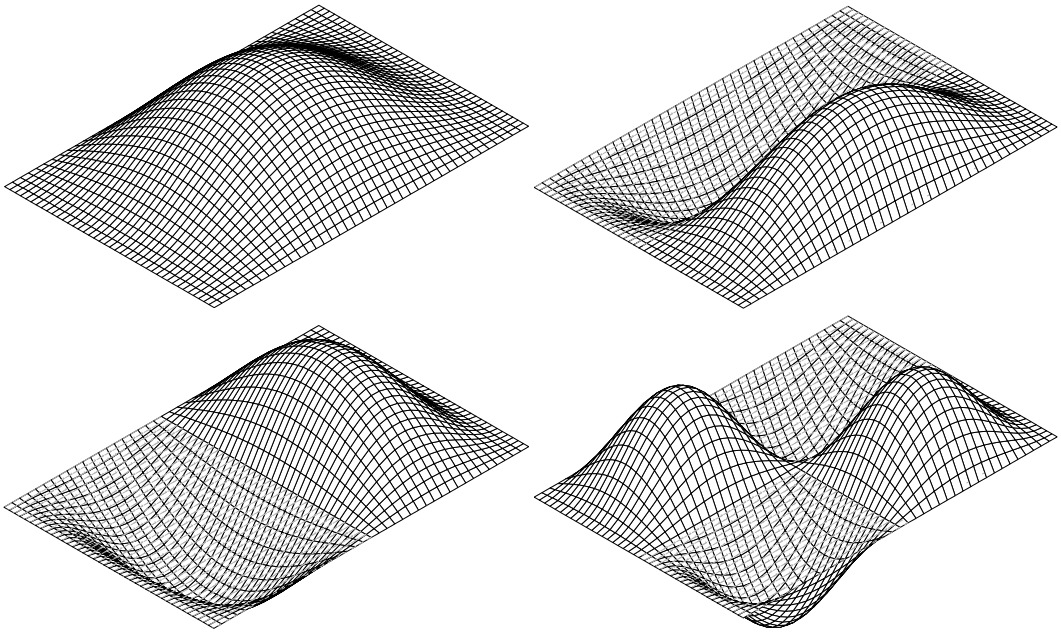

Figure 5.5 The lowest 4 free vibration mode shapes computed by finite element analysis. From left to right and top to bottom, these are mode 1 (169 Hz), mode 2 (358 Hz), mode 3 (390 Hz), and mode 4 (570 Hz)

Chapter 6

Optimal control design

6.1 Background theory

Optimal control is made possible because of the linear approximation made with respect to buckling theory. This approximation enables a nonlinear, unstable system to be approximated by a set of linear eigenvalue equations that can subsequently be constrained and optimised. Although this linear approximation does not capture the exact buckling behavior in its entirety, it is adequate for control design purposes.

The buckling eigenvalue problem forms a basis for the design of the active buckling controller. Control gains are found using a linear matrix inequality (LMI) formulation in a semi-definite linear solver space[26]. A state space definition of the model can be created for control analysis purposes. The plant matrix is defined:

$$A(P) = \begin{bmatrix} 0 & I \\ -M^{-1}\left(K - PK_G\right) & -M^{-1}C \end{bmatrix} \tag{6.1}$$

where C is the structural damping matrix, M is the structural mass matrix, K is the structural stiffness matrix, K_G is the geometric stiffness matrix, P is a scalar compressive load magnitude and I is an identity matrix of the appropriate size.

The state space control mapping matrix B_1 is defined:

$$B_1 = \begin{bmatrix} 0 \\ M^{-1}D \end{bmatrix} \tag{6.2}$$

where D maps the control actuation outputs to actuated degrees of freedom. Using static output feedback the control input is defined:

$$u(t) = -Gy(t) = -GC_1x(t) \tag{6.3}$$

where $y(t)$ is the vector of measured outputs, G is the control gain matrix, and $y(t) = C_1x(t)$ maps the states, $x(t)$, to the measured outputs. Equation 6.3 leads to the closed loop plant matrix:

$$A_{CL} = A\,(P) - B_1GC_1 \tag{6.4}$$

Assuming a block diagonal structure allows both the control gain matrix G and the measurement matrix C_1 to be separated into their proportional and derivative parts: G_1, G_2 and $C_{1:11}$, $C_{1:22}$ respectively.

$$G = [G_1, G_2] \tag{6.5}$$

$$C_1 = \begin{bmatrix} C_{1:11} & 0 \\ 0 & C_{1:22} \end{bmatrix} \tag{6.6}$$

One multiple objective definition can be used to describe the control problem that is to be optimised. Equation 6.7 defines the objective function and constraints passed to the optimisation routine. The formulation has been contracted to modal space to reduce the required computational effort [21, 2, 3].

$$
\begin{aligned}
\text{minimize} \quad & \alpha P + \beta\lambda_c + \gamma\theta \\
\text{subject to} \quad & \overline{\Phi}^T \left[(K + DG_1C_{1:11}) + PK_G\right]\overline{\Phi} > 0 \\
& \overline{\Phi}^T \left[(C + DG_2C_{1:22}) + \lambda_c I\right]\overline{\Phi} > 0 \\
& \begin{bmatrix} \theta I_m & G \\ G^T & I_n \end{bmatrix} \geq 0 \\
& P < -P_{desired}
\end{aligned}
\tag{6.7}
$$

where Φ is a matrix containing the first m vibration mode shapes. λ_c and θ are measures of the closed loop damping and control effort. α, β and γ are scalars which weight the objective in terms of closed loop buckling load, damping and control effort respectively. The eigenvalues of Equation 6.7 are now negative and the goal of the optimisation routine is to minimise (make more negative) the maximum eigenvalue. The three objectives are to minimise the control effort, maximise the structural damping and converge to the desired closed loop buckling load. The details of the derivation of this formulation have been published previously [3].

6.2 Dynamic contraction

The plate model was transformed into modal space to contract the set of linear equations to a size that is feasible for optimising Equation 6.7. The computational effort required of the solver grows geometrically with the size of the system of linear equations at a cubic or higher rate [25]. This contraction was performed using the lowest twenty dynamic mode shapes, as the first twenty modes are able to represent the dynamics and first three buckling modes of the physical system to a sufficient level of accuracy. Performing this contraction reduces the size of

Table 6.1 Sample of script file for SDP optimisation.

```
%Script file for input to SDPSOL.
%Generated through Matlab to solve plate buckling control optimisation

%Written by J. Welham, 28/8/02
variable G1(q,r); variable G2(q,r); variable P, lambdaC, theta; G=[G1,G2];

initialize G1=zeros(q,r); initialize G2=zeros(q,r); initialize lambdaC=0; initialize theta=1;

phi' * [(K + D * G1 * C11) + P * Kg] * phi > 0;
phi' * [(C + D * G2 * C22) + lambdaC * eye(n)] * phi > 0; P < -PDesired;

lambdaC < 0;

[theta * eye(q), G;
G', eye(2 * r)] > 0;

minimize obj_value = alpha * P + beta * lambdaC + gamma * theta;
ABSTOL=0.000003; RELTOL=0.000003;
```

the problem to be solved from approximately 1000 degrees of freedom to 20 modal coordinates.

6.3 Semi-definite linear optimisation

Spdsol is a stand-alone semi-definite optimisation problem solver, written by Stephen Boyd and Shao-Po Wu [26]. The solver inputs and outputs are Matlab® binary workspace files, and it requires a text script file containing the optimisation definition. Tables 6.1 and 6.2 show a sample script file and screen output from the solver as it was used for this application.

6.4 Closed-loop control formulation

The state space closed-loop control system can be represented in state space form using the state description $x(t)$:

$$x(t) = \left\{ \begin{array}{c} v(t) \\ \dot{v}(t) \end{array} \right\} \tag{6.8}$$

where $v(t)$ and $v\dot{(}t)$ are the physical deflections and velocities. The resulting state space equations comprise a complete description of the closed-loop system in a

Table 6.2 Sample output from SDP solver.

This is sdpsol, version beta. Copyright (c) 1996, Shao-Po Wu and Stephen Boyd.
Compilation log messages:
script.txt:6 declare 2x2 primal variable G1.
script.txt:7 declare 2x2 primal variable G2.
script.txt:8 declare 1x1 primal variable P.
script.txt:8 declare 1x1 primal variable lambdaC.
script.txt:8 declare 1x1 primal variable theta.
script.txt:16 specify 20x20 LMI constraint.
script.txt:17 specify 20x20 LMI constraint.
script.txt:18 specify 1x1 LMI constraint.
script.txt:20 specify 1x1 LMI constraint.
script.txt:23 specify 6x6 LMI constraint.
Compilation completes without error.
bigMsp: initial x given is not strictly primal feasible (min e.v. -58204.3): start phase 1.

primalobj.	*dualobj.*	*dual.gap*
$6.40e+04$	$-1.75e+05$	$2.39e+05$
$6.76e+04$	$-8.49e+04$	$1.53e+05$
$4.76e+04$	$-5.21e+04$	$9.96e+04$
$3.34e+04$	$-7.43e+03$	$4.09e+04$
$8.84e+03$	$-2.41e+03$	$1.12e+04$
$3.03e+03$	$-4.09e+02$	$3.44e+03$
$7.93e+02$	$-9.71e+01$	$8.90e+02$
$2.33e+02$	$-2.25e+01$	$2.55e+02$
$5.44e+01$	$-7.79e+00$	$6.21e+01$
$1.59e+01$	$-3.75e+00$	$1.96e+01$
$2.99e+00$	$-2.24e+00$	$5.23e+00$
$1.09e+00$	$-8.36e-01$	$1.93e+00$
$1.89e-01$	$-3.10e-01$	$4.99e-01$
$7.51e-02$	$-8.14e-02$	$1.56e-01$
$1.22e-02$	$-2.24e-02$	$3.45e-02$
$4.82e-03$	$-5.49e-03$	$1.03e-02$
$6.92e-04$	$-1.54e-03$	$2.24e-03$
$2.20e-04$	$-4.46e-04$	$6.66e-04$
$-2.43e-05$	$-1.83e-04$	$1.58e-04$

bigMsp: phase 1 is feasible. bigMsp: start phase 2.

primalobj.	*dualobj.*	*dual.gap*
$1.95e+10$	$-6.43e+07$	$1.95e+10$
$1.95e+10$	$-1.29e+10$	$3.24e+10$
$8.15e+09$	$-9.05e+09$	$1.72e+10$
$1.14e+08$	$-6.67e+09$	$6.78e+09$
$1.14e+08$	$-1.72e+09$	$1.83e+09$
$7.96e+06$	$-4.65e+08$	$4.73e+08$
$7.96e+06$	$-1.18e+08$	$1.26e+08$
$5.45e+05$	$-3.16e+07$	$3.21e+07$
$5.29e+05$	$-7.98e+06$	$8.51e+06$
$3.47e+04$	$-2.12e+06$	$2.15e+06$
$-6.71e+03$	$-5.53e+05$	$5.46e+05$
$-3.00e+04$	$-1.74e+05$	$1.44e+05$
$-3.76e+04$	$-8.78e+04$	$5.03e+04$
$-3.91e+04$	$-4.70e+04$	$7.91e+03$
$-3.96e+04$	$-4.25e+04$	$2.85e+03$
$-3.97e+04$	$-4.02e+04$	$4.14e+02$
$-3.98e+04$	$-3.99e+04$	$1.44e+02$
$-3.98e+04$	$-3.98e+04$	$2.90e+01$
$-3.98e+04$	$-3.98e+04$	$8.97e+00$
$-3.98e+04$	$-3.98e+04$	$2.20e+00$
$-3.98e+04$	$-3.98e+04$	$6.00e-01$
$-3.98e+04$	$-3.98e+04$	$1.58e-01$
$-3.98e+04$	$-3.98e+04$	$3.94e-02$

*** Problem: script.txt
11 variables LMI size: 48-by-48 5 diagonal blocks SDP problem.
** Algorithm parameters:
ABSTOL = 3e-06 RELTOL = 3e-06 BIGM = 5.8399e+07 NU = 10 MAXITER = 100
** Optimization result
OPTIMAL after 22 iterations, sdpsol stopped because RELATIVE TOLERANCE was reached.
** Objective value
objvalue = -39779.1

*** Variables

$$G1 = \begin{bmatrix} 3.0352 & 2.3898 \\ 3.0352 & -2.3898 \end{bmatrix} \quad G2 = \begin{bmatrix} 0.0001 & 0.0001 \\ 0.0001 & -0.0001 \end{bmatrix}$$

$P = -58204.3$
$lambdaC = -7.48624e-06$
$theta = 18.4251$

Result of "script.txt": OPTIMAL after 22 iterations, sdpsol stopped because RELATIVE TOLERANCE was reached.

---

format that can be directly simulated:

$$\begin{array}{rcccccc} \dot{x(t)} & = & A_{CL} & x(t) & + & B & u(t) \\ y(t) & = & C & x(t) & + & D & u(t) \end{array} \tag{6.9}$$

where $y(t)$ is the measured output, $u(t)$ is the control input, and A_{CL} is the closed-loop plant matrix which is defined along with the other system matrices (B,C,D):

$$\begin{aligned} A_{CL} &= \begin{bmatrix} 0 & I \\ -M^{-1}(K - PKg) & -M^{-1}C \end{bmatrix} \\ B &= \begin{bmatrix} 0 \\ -M^{-1}D \begin{bmatrix} G_1 & G_2 \end{bmatrix} \end{bmatrix} \\ C &= \begin{bmatrix} C_{1:11} & 0 \\ 0 & C_{1:22} \end{bmatrix} \\ D &= \begin{bmatrix} 0 \\ 0 \end{bmatrix} \end{aligned} \tag{6.10}$$

As discussed in Section 6.2 a coordinate transform was performed to convert the system into modal space. This was achieved by pre-multiplying and post-multiplying structural matrices by a matrix of the first m dynamic eigenmodes, Φ. For example, the structural mass matrix, $M_{[n,n]}$, after contraction becomes $(\Phi' M \Phi)_{[m,m]}$, where $m << n$ to reduce size and complexity without sacrificing any ability to capture the buckling and vibration dynamics of interest. The modal state space system matrices are annotated with an overbar and are defined:

$$\begin{aligned}
\overline{A_{CL}} &= \begin{bmatrix} 0 & I \\ -(\Phi' M \Phi)^{-1}\Phi'(K - PKg)\Phi & -(\Phi' M \Phi)^{-1}\Phi' C \Phi \end{bmatrix} \\
\overline{B} &= \begin{bmatrix} 0 \\ -(\Phi' M \Phi)^{-1}\Phi' D \begin{bmatrix} G_1 & G_2 \end{bmatrix} \end{bmatrix} \\
\overline{C} &= \begin{bmatrix} C_{1:11}\Phi & 0 \\ 0 & C_{1:22}\Phi \end{bmatrix} \\
\overline{D} &= \begin{bmatrix} 0 & 0 \\ 0 & 0 \end{bmatrix}
\end{aligned} \tag{6.11}$$

Considering the real time discrete implementation with r inputs and q measured outputs the system can be represented in various domains. The control input is therefore defined in the continuous time domain:

$$u(t)_{[q,1]} = \mathbf{G}_{1_{[q,r]}} \overline{v}(t)_{[r,1]} + \mathbf{G}_{2_{[q,r]}} \dot{\overline{v}}(t)_{[r,1]} \tag{6.12}$$

$$\frac{U(s)_{[q,1]}}{V(s)_{[r,1]}} = \mathbf{G}_{1_{[q,r]}} + s\mathbf{G}_{2_{[q,r]}} \tag{6.13}$$

where G_1 and G_2 are the proportional and derivative feedback gains, and $\overline{v}$ and $\dot{\overline{v}}$ are the modal displacement and velocity. A laplace transform yields the transfer function matrix, relating the control input and modal displacements in the frequency domain. The discrete time domain definition using a sampling rate, T_s, and a simple two point difference method for velocity estimation is therefore defined:

$$u(k)_{[q,1]} = \mathbf{G}_{1_{[q,r]}} \overline{v}(k)_{[r,1]} + \mathbf{G}_{2_{[q,r]}} \left(\frac{\overline{v}(k)_{[r,1]} - \overline{v}(k-1)_{[r,1]}}{T_s} \right) \tag{6.14}$$

Chapter 7

Dynamic simulation

7.1 System specifications

The control architecture designed for the active laminate consists of two output channels, each of which drives two pairs of piezoceramic actuators that provide the desired restoring moments. The locations of these four pairs of actuators are shown in Figure 7.1. The original design featured up to fourteen pairs of actuators, but control ratio analysis in Section 4.4.4 showed that by careful placement this number could be reduced to four pairs with little loss of performance. The actuator locations were chosen to maximise their combined effect on the first two buckling modes. The symmetry of these mode shapes allows the pairs of actuators that are located symmetrically relative to the plate loading axis to be driven off the same control channel, thus reducing the number of independent control outputs to two. As well as simplifying the control optimisation process this reduction in the number of actuators allows the response time to be reduced for specified current limits on the high voltage piezo amplifier as described in Section 9.2.1. This closed loop system architecture has been optimised to suppress the two lowest buckling modes and obtain a compressive loading capacity of 2.3 times the uncontrolled buckling load P_{CR}, which is 29 kN/m.

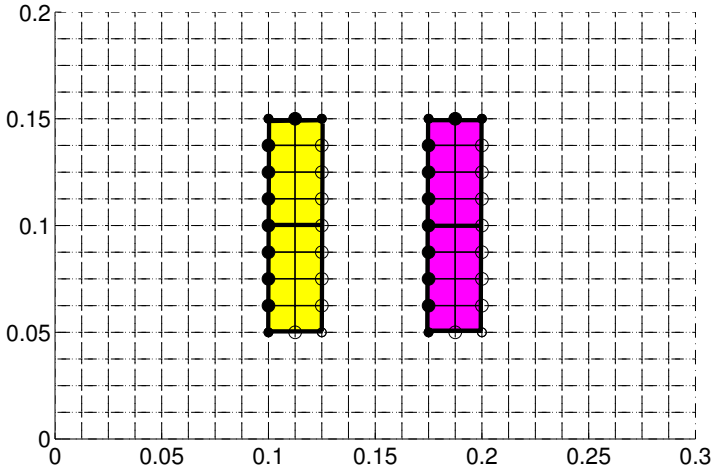

Figure 7.1 Location of actuators on plate.

7.2 Closed-loop dynamics

The dynamics of the closed-loop system can be defined by the linear equation of motion, which incorporates the control feedback terms:

$$M\,\ddot{x} + (C + DG_2C_{1:22})\,\dot{x} + (K + DG_1C_{1:11} - PK_G)\;x = 0 \qquad (7.1)$$

where the vector x represents the nodal translations and rotations; $\dot{x}$ and $\ddot{x}$ are the velocities and accelerations respectively.

This dynamic system was simulated in Matlab® using the Simulink® environment. The control feedback loop was separated from the free dynamics as shown in Figure 7.2 to allow the feedback control system to incorporate features like discrete sampling, noise and filtering, while the plant model is a continuous system. This mixed discrete-continuous system is the most accurate representation of an actual implementation and enables the determination of design tradeoffs for filtering and other necessary elements. Hence, although it is possible to derive velocity measurements from accelerometers or other rate sensors, in this

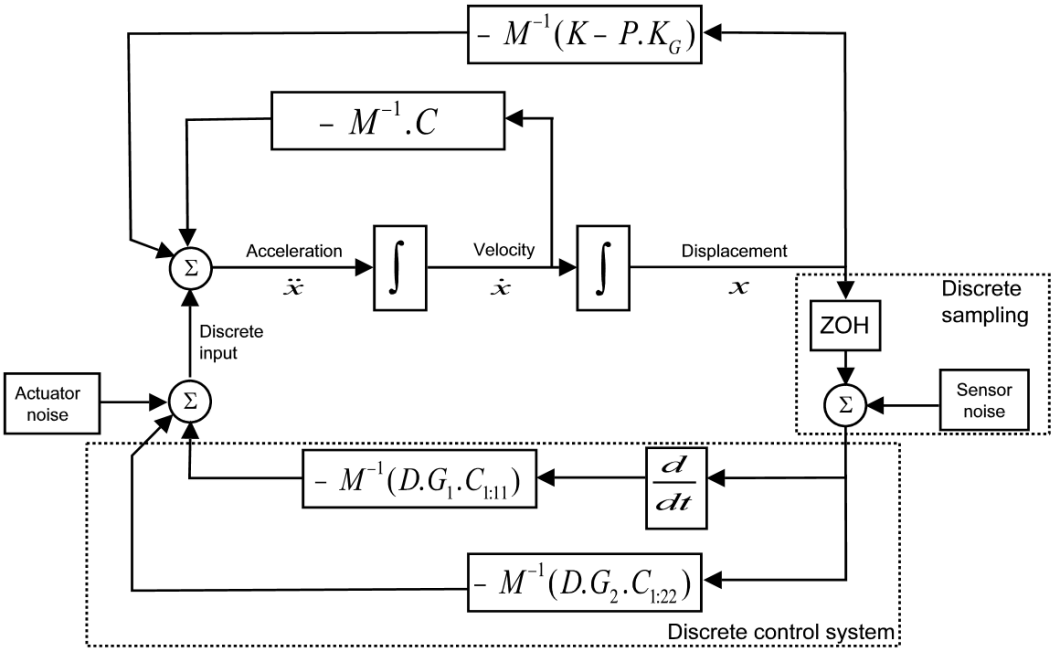

Figure 7.2 Schematic of the active plate simulation.

mixed formulation velocity is estimated and filtered from displacement measurements, to represent experiments using strain or displacement sensing only. For this simulation velocity is calculated using a simple two-point difference method. This relatively simple method was chosen as more complex and accurate methods generally introduce greater lag into the signal path. Hence the tradeoff in determining velocity is between noise and signal lag due to filtering.

As mentioned in Section 6.2 this model was contracted using the free vibration eigenmodes of the plate to reduce the number of simultaneous equations from approximately 1000 (degrees of freedom) to 20 (modes) [21]. Noise was introduced into the sampled measurements to test the robustness of the control system. Band-limited white noise was used to achieve this task and provides a normally distributed random output. The generated noise amplitude is defined using a parameter which sets the height of the power spectral density.

To represent the discretisation required for a digital control system, the con-

tinuous model is sampled using a zero-order hold (ZOH) function. This function replicates the use of an analogue to digital convertor in that it samples the continuous system at a specified sampling rate and holds the returned value between samples.

By simulating the essential features of the discrete controller with the continuous system it was possible to determine the effects of sampling rate, quantisation and velocity estimation. This information is valuable as a discrete controller will be used in any actual controlled system as in the experiments presented in this research. This mixed formulation is unique in the design of this type of active laminate.

Various continuous solver algorithms are available in the Simulink® environment and the default, ODE45, was found to be best. Other algorithms were either substantially slower, or failed to converge. The solver was used with a variable time step and default automatic tolerances. Simulations were evaluated either until the system became unstable, determined by the saturation of integrator blocks, or for a maximum simulation time of 0.25 seconds.

7.3 Sensors and noise levels

Pairs of strain gauges mounted on the laminate surface were used to measure in-plane strain during experiments and then converted to bending strain by taking the difference between the two readings. However, this subtraction operation resulted in twice the noise amplitude seen in each strain measurement because each sensor was assumed to have independent noise inputs.

The Simulink® white noise generator is parameterised by a noise power level. Noise was summed into the simulation control feedback path, which is in units of modal amplitude, and therefore it was necessary to convert a given level of noise in a bending strain measurement to the equivalent modal amplitude. This

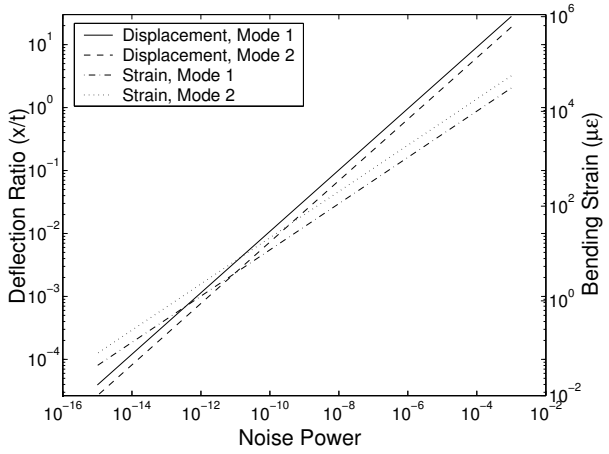

Figure 7.3 Plate deflection and plate surface strain versus noise power for buckling modes 1 and 2.

relationship can be seen in Figure 7.3, and the raw data can be found in Table 7.1. The conversion from nodal deflections to elemental strain is based on the general isoparametric quad as derived by Cook [27]:

$$\begin{bmatrix} \varepsilon_x \\ \varepsilon_y \\ \gamma_{xy} \end{bmatrix} = \sum_{i=1}^{N} \begin{bmatrix} 0 & -zA_i & 0 \\ 0 & 0 & -zB_i \\ 0 & -zB_i & -zA_i \end{bmatrix} \begin{Bmatrix} w_i \\ \theta_{xi} \\ \theta_{yi} \end{Bmatrix} \tag{7.2}$$

where ε_x, ε_y and γ_{xy} are the elemental plane and shear strains, w_i, θ_{xi} and θ_{yi} are the nodal deflections and rotations for the ith node, z is the distance from the neutral axis to the strain gauge, and A_i and B_i are defined:

$$\begin{aligned} A_i &= \tau_{11}\frac{\delta N_i}{\delta \xi} + \tau_{12}\frac{\delta N_i}{\delta \eta} \\ B_i &= \tau_{21}\frac{\delta N_i}{\delta \xi} + \tau_{22}\frac{\delta N_i}{\delta \eta} \end{aligned} \tag{7.3}$$

where τ is the inverse Jacobian:

$$\tau = J^{-1} = \begin{bmatrix} \frac{\delta x}{\delta \xi} & \frac{\delta y}{\delta \xi} & 0 \\ \frac{\delta x}{\delta \eta} & \frac{\delta y}{\delta \eta} & 0 \\ 0 & 0 & 1 \end{bmatrix} = \begin{bmatrix} \frac{1}{a} & 0 & 0 \\ 0 & \frac{1}{b} & 0 \\ 0 & 0 & 1 \end{bmatrix} \tag{7.4}$$

Table 7.1 Conversion between noise power, average noise amplitude and equivalent strain and deflections for the lowest two buckling modes.

Noise Power (Modal)	Approximate Noise Amplitude (Modal)	Equivalent Max Deflection Mode 1: mm	Equivalent Max Bend. Strain Mode 1: $\mu\varepsilon$	Equivalent Max Deflection Mode 2: mm
1E-3	5	28	31000	19
0.5E-3	3	16.8	18600	11.4
1E-4	1.5	8.4	9300	5.7
0.5E-4	1	5.6	6200	3.8
1E-5	0.6	3.36	3720	2.28
0.5E-5	0.3	1.68	1860	1.14
1E-6	0.18	1.008	1116	0.684
0.5E-6	0.1	0.56	620	0.38
1E-7	0.06	0.336	372	0.228
0.5E-7	0.03	0.168	186	0.114
1E-8	0.02	0.112	124	0.076
0.5E-8	0.01	0.056	62	0.038
1E-9	0.005	0.028	31	0.019
0.5E-9	3E-3	0.0168	18.6	0.0114
1E-10	2E-3	0.0112	12.4	0.0076
0.5E-10	1.2E-3	0.00672	7.44	0.00456
1E-11	6E-4	0.00336	3.72	0.00228
0.5E-11	3.5E-4	0.00196	2.17	0.00133
1E-12	2E-4	0.0012	1.24	0.00076
0.5E-12	1E-4	0.00056	0.62	0.00038
1E-13	6E-5	0.000336	0.372	0.000228
0.5E-13	3E-5	0.000168	0.186	0.000114
1E-14	1.8E-5	0.0001008	0.1116	6.84E-5
0.5E-14	1.2E-5	6.72E-5	0.0744	4.56E-5
1E-15	7E-6	3.92E-5	0.0434	2.66E-5

where a and b are the elemental length and width. As rectangular elements are used in this model, A_i and B_i can be simplified:

$$A_i = \frac{1}{a}\frac{\delta N_i}{\delta \xi} B_i = \frac{1}{b}\frac{\delta N_i}{\delta \eta} \tag{7.5}$$

By substituting these new definitions of A_i and B_i into Equation 7.2 the specific relationship between nodal deflections and elemental strain becomes:

$$\begin{bmatrix} \varepsilon_x \\ \varepsilon_y \\ \gamma_{xy} \end{bmatrix} = \sum_{i=1}^{N} \begin{bmatrix} 0 & 0 & -\frac{z}{a}\frac{\delta N_i}{\delta \xi} \\ 0 & -\frac{z}{b}\frac{\delta N_i}{\delta \eta} & 0 \\ 0 & -\frac{z}{a}\frac{\delta N_i}{\delta \xi} & \frac{z}{b}\frac{\delta N_i}{\delta \eta} \end{bmatrix} \begin{Bmatrix} w_i \\ \theta_{xi} \\ \theta_{yi} \end{Bmatrix} \tag{7.6}$$

7.4 Actuator authority

Actuator authority is a limiting factor in the performance of active buckling controllers. Blocked force calculations were performed on actuator pairs to estimate actuator authority, and the results were incorporated in control simulations. Table 7.2 shows the actuator specifications for the following example actuator authority calculation. Blocked forces (F) and moments (M) were calculated:

$$\begin{aligned} F_X &= E_{pzt} \times \varepsilon_{mx} \times l_W \times t_W \\ &= 60 \times 10^9 \times 262 \times 10^{-6} \times 0.0459 \times 0.254 \times 10^{-3} \\ &= 183.3N \end{aligned} \tag{7.7}$$

Table 7.2 Specifications for QP10N actuators.

Actuator dimensions	l_A x w_A x t_A	50.8 x 25.4 x 0.381 mm
PZT wafer dimensions	l_W x w_W x t_W	45.9 x 20.5 x 0.254 mm
Maximum actuation strain	ε_{mx}	262 $\mu\varepsilon$
Maximum rated voltage	V_{mx}	200 Volts
Capacitance	Cap	0.06 μF
PZT Stiffness	E_{pzt}	60 GPa
Moment Arm	z	1.6 mm **

** The moment arm is defined as the material thickness between the two embedded actuators.

$$\begin{aligned} F_Y &= E_{pzt} \times \varepsilon_{mx} \times w_W \times t_W \\ &= 60 \times 10^9 \times 262 \times 10^{-6} \times 0.0205 \times 0.254 \times 10^{-3} \\ &= 81.9N \end{aligned} \tag{7.8}$$

$$\begin{aligned} M_X &= F_Y \times z \\ &= 81.9 \times 0.0016 \\ &= 0.131Nm \end{aligned} \tag{7.9}$$

$$\begin{aligned} M_Y &= F_X \times z \\ &= 183.3 \times 0.0016 \\ &= 0.293Nm \end{aligned} \tag{7.10}$$

Considering the actuator incorporates eight elements in the finite element model, as shown in Figure 7.4, the blocked moment per node ($\overline{M}$)can be calculated:

$$\begin{aligned} \overline{M_X} &= 0.131/2 \\ &= 0.0655Nm/node \end{aligned} \tag{7.11}$$

$$\begin{aligned} \overline{M_Y} &= 0.293/4 \\ &= 0.0733Nm/node \end{aligned} \tag{7.12}$$

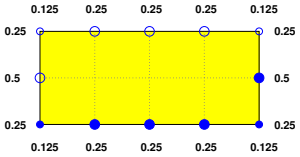

Figure 7.4 Nodal moment application factors for a single pair of patches covering eight elements.

7.5 Actuator location

The actuator locations were chosen based on the shape of the buckling modes to be controlled. Actuators were placed at locations of high strain, for both modes to be controlled. In this case the locations also account for the symmetry required to actuate into both modes 1 and 2 using the same actuators.

A limited number of simulations were performed to confirm the locations chosen were optimal. The axial (x) and transverse (y) distance between actuators were independently varied, as shown in Figure 7.5. Results from these simulations are shown in Figure 7.6. By moving the actuators apart in the transverse direction (increasing y) by even a small amount, the performance of the closed-loop system drops substantially. Any increase in x results in a critical load ratio of approximately 1, which means that the controller has failed to add any stiffness above the critical load. Reducing x causes reduced controller performance and so the chosen location is seen to be optimal.

7.6 Dynamic response simulations

Multiple sets of simulations were conducted to explore the effect of varying the control sampling rate, noise level and actuator authority on the performance of a closed loop system designed to prevent buckling for loads of up to 2.3 P_{CR}. Each set of simulations typically consisted of several thousand individual simulations, which were combined to form a single three-dimensional surface or contour plot

showing the closed-loop critical loads for various initial conditions.

These simulations all started with a perfectly flat plate, in static equilibrium under an axial compressive load P. A perturbation consisting of an initial combination of displacement and velocity in the shape of the lowest buckling mode was then applied, as a perfectly flat plate will never buckle. These initial conditions were intended to represent imperfections in plate manufacture and loading, and any outside disturbance impulses. A stable system response oscillates back to zero displacement and velocity, whereas an unstable system response grows exponentially. For a given set of initial conditions, simulations were performed with increasing load P until an unstable load was found. A bisection method was then used to accurately locate the critical load for the given conditions. Contour or surface plots, similar to those seen in Figure 7.7 were used to display the highest achievable closed-loop critical buckling load for a range of initial conditions.

7.6.1 Discretisation of control loop

As discussed above, the control feedback loop was discretised to represent the digital nature of the controller hardware presented in this research. These simulations were used to determine the effect of the control system sampling frequency

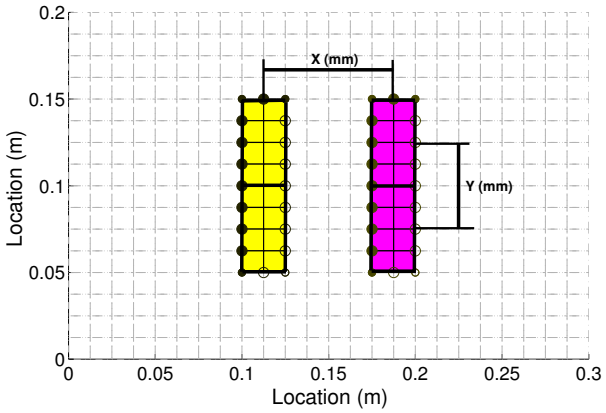

Figure 7.5 Optimal actuator location.

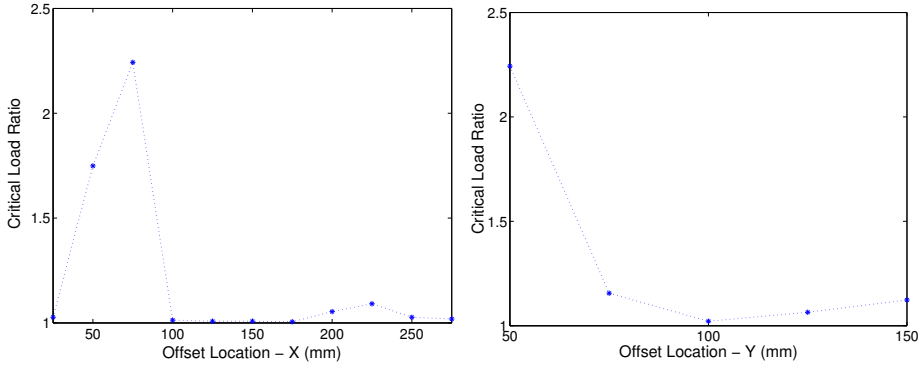

Figure 7.6 Results of simulations where actuator location has been varied in the longitudinal (left) and transverse (right) directions. The minimum location offset is defined by the finite size of the actuators.

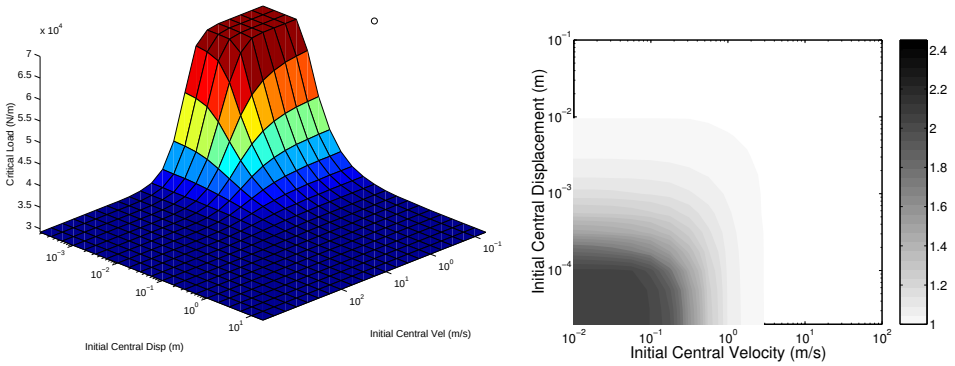

Figure 7.7 Example of simulation surface results.

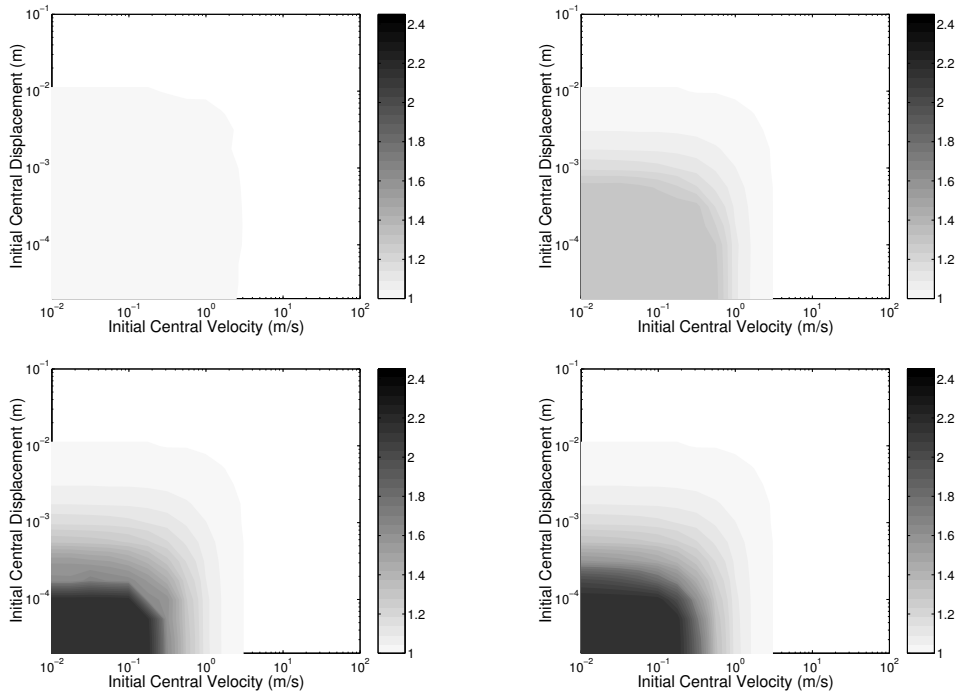

Figure 7.8 Contour plots of peak stable closed-loop buckling load ratio P/P_{CR} as a function of out-of-plane perturbation size and velocity at the center of the plate for different discretised controller frequencies F_s. From left to right and top to bottom, these plots correspond to frequencies of 1, 7, 10 and 100kHz respectively.

(F_s) on the magnitude of the compressive load (P) that could be sustained under closed-loop control, and the results are shown in Figure 7.8 and Table 7.3.

It is apparent from Table 7.3 that a sampling rate of 10 kHz is required for the controller to stabilise the full design closed-loop control load of 65 kN/m, or 2.3 times P_{CR}. These results indicate that even if the modal amplitudes are measured perfectly, in order to achieve the designed control performance the sensor scanning rate needs to be at least 3 times the frequency of the highest eigenmode used to model the active plate dynamics, and about 20 times the frequency of the eigenmode whose mode shape corresponds to the highest buckling mode being suppressed. Reducing the control loop sampling frequency both reduces the controller bandwidth, and increases the inherent delay caused by the sampling operation. It is not obvious which of these two effects dominates the performance drop of the controller at sampling frequencies below 10kHz as seen in Figure 7.8.

Table 7.3 The peak controllable closed-loop buckling load P and its ratio to the open loop buckling load P_{CR} versus different discretised controller frequencies F_s.

F_s [kHz]	P [kN/m]	$\frac{P}{P_{CR}}$
1	30	1.03
3	32	1.10
5	35	1.21
7	39	1.34
10	66	2.30
100	66	2.30

7.6.2 Transport delay

Delays through the control loop often play a critical part on the effectiveness of a control system. Simulations were performed where a transport delay, in addition to the inherent delay associated with sampling, was introduced into the feedback path. The control loop was operating at a rate of 30kHz, which implies an inherent delay due to sampling of approximately $\frac{T_S}{2}$ or $17\mu s$. Table 7.4 and Figure 7.9 show the results of this simulation on the height of the upper plateau (closed-loop buckling load). It can be seen that an additional transport delay over $10\mu s$ will result in a substantial degradation of the achievable closed-loop buckling load.

Table 7.4 Effect of transport delay on closed-loop performance.

Delay (μs)	Plateau (kN/m)
10000	29.3
5000	29.3
1000	29.7
500	30
100	34.8
50	43.8
10	66
5	66
1	66

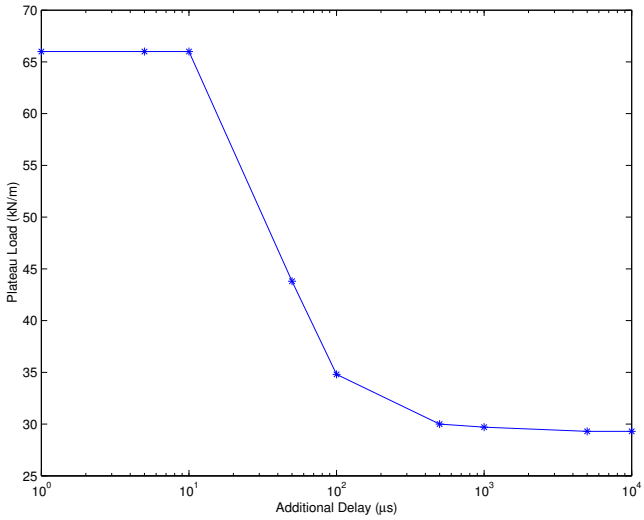

Figure 7.9 Effect of additional transport delay on closed-loop performance.

7.6.3 Noise

Noise was introduced into the model to test the robustness of the control system in realistic conditions, where sensors have a finite accuracy that is often dictated by electrical noise. The average modal noise power can be converted to an equivalent central deflection or strain measurement as described in Section 7.3. Figure 7.3 shows this relationship for the two lowest modes over a range of noise power.

The peak stable closed-loop load, P, that could be maintained was then calculated for various levels of this noise power by running simulations with a control loop sampling rate of 10kHz. This sampling rate was used as a baseline for simulations as slower rates would not achieve the optimised closed-loop buckling loads. Noise does not interact with the sampling rate directly, but rather through the filtering that is possible at higher sampling rates. Noise reduces the controller's ability to determine the exact plate deflection, and that inexactitude will be greater for the velocities calculated from these deflections. As a result, the active plate will be less able to stabilise a given compressive load.

Figure 7.10 shows the results for both sensor and actuator noise. These two

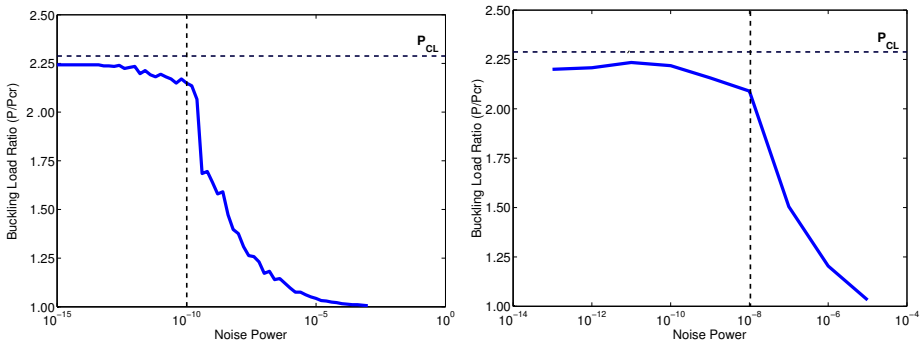

Figure 7.10 Peak stable closed-loop load P versus noise power (sensor noise on left and actuator noise on right).

cases refer to the addition of noise at different points of the control feedback loop as seen in Figure 7.2. The sensor noise represents unavoidable electrical noise present in measured strain signals. Actuator noise represents both the electrical noise present at the piezo amplifier output and due to the hysteresis and nonlinearity of the piezo actuators. Sensor and actuator noise were simulated independently.

Considering the sensor noise plot, the maximum controllable load P decreases rapidly as the noise level is increased from 10^{-10} to 10^{-9}, which correspond to central deflections of 28 and $11\mu m$ respectively as listed in Table 7.1. Below 10^{-10} the buckling load becomes relatively independent of noise, indicating that to control the first two modes the noise power in the control loop must be less than or equal to 10^{-10}. As shown in Figure 7.3, this threshold noise is equivalent to an average strain amplitude of some $12\mu\varepsilon$ for mode 1, and $22\mu\varepsilon$ for mode 2, at their respective mode shape peaks; or peak deflections of $11\mu m$ for mode 1 and less than $8\mu m$ for mode 2. To put these values in context, MEMS extensometers have a resolution of approximately $1\mu\varepsilon$, while micromachined silicon resistive strain gages can achieve resolutions of a few microstrain. On the deflection side, commercially available non-interferometric laser distance sensors have resolutions between 1 and $10\mu m$, while capacitive distance sensors range from less than

$0.001\mu m$ to a couple of μm, depending on various factors including surface flatness and finish. It can then be concluded that current strain and displacement sensor technology can provide a resolution well within these limits of uncertainty and of sufficient accuracy for this controller.

The actuator noise plot shows a similar trend to the sensor noise. The critical noise power for in this case is 10^{-8}, which corresponds to approximately 25% of the actuator authority. The actuator noise is therefore considered to be less crucial to control performance than that of the sensors.

7.6.4 Actuator authority

The actuator authority is a limit on the available bending moment generated by each pair of piezoceramic patches. Conventional 0.25mm thick piezoceramic patches, such as ACX Quickpack®, provide a blocked force of approximately $4N/mm$, which corresponds to a moment of $0.08Nm$ per node in the finite element model, and this value was chosen as a baseline. Simulations were run with several levels of actuator authority, both above and below the baseline, using a discretised control loop sampling rate of 10kHz.

The top right contour plot in Figure 7.11, which represents the expected control limit given the available actuators, shows the actively controlled system to be stable for an initial central deflection of up to $0.1mm$ and an initial velocity of up to $0.2m/s$. The two bottom plots in Figure 7.11 show that since the controller has been optimised to suppress a certain set of buckling modes, increasing the available actuator authority well past the baseline value does not increase maximum load. The design limit cannot be exceeded, unless the controller is re-optimised for a higher load $P_{desired}$ and thus to account for higher modes. Although the additional authority does not raise the height of the plateau, it does allow the system to tolerate larger out-of-plane perturbations, which increases its

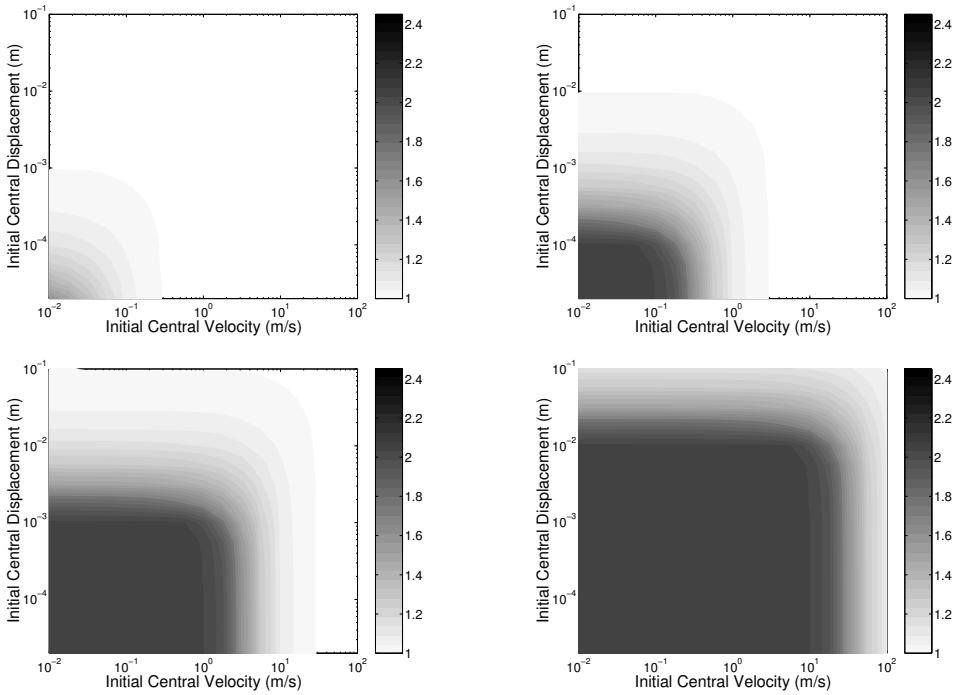

Figure 7.11 Contour plots of peak stable closed-loop buckling load ratio P/P_{CR} as a function of out-of-plane perturbation size and velocity at the center of the plate for different actuator authorities in the absence of noise. From left to right and top to bottom, they correspond to force levels of 0.008, 0.08, 0.8 and 8 Nm per node respectively.

robustness.

In the presence of noise, the ability of actuator authority to compensate for this uncertainty is indicated by Figure 7.12. Note that the assumed noise power level of 10^{-9} is orders of magnitude higher than what is expected in practice, as discussed previously and shown in Table 7.1. Even under these conditions, the baseline actuators can maintain a buckling load of approximately 1.7 times P_{CR}, a reduction of 26%. An increase in authority restores performance almost to the level of the corresponding lower left plot in Fig. 7.11.

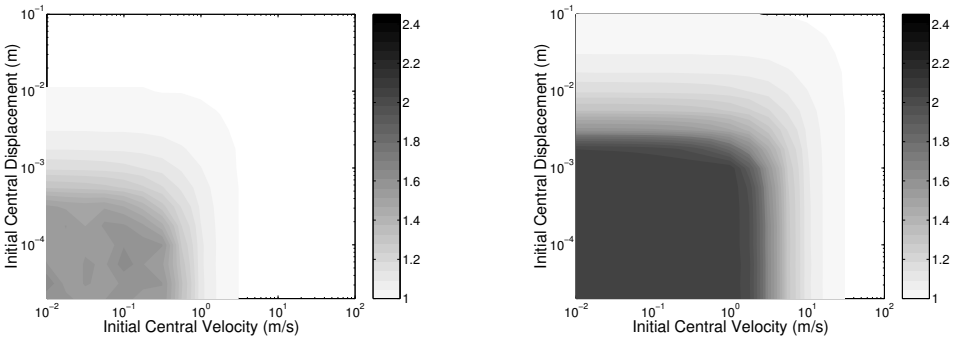

Figure 7.12 Contour plots of peak stable closed-loop buckling load ratio P/P_{CR} as a function of out-of-plane perturbation size and velocity at the center of the plate in the presence of a noise power of 10^{-9}. These plots correspond to actuator authorities of 0.08 (left) and 0.8 N/m per node (right).

7.6.5 Alternative solver results

To verify the results obtained from the Simulink® ODE45 solver, a Newmark-Beta numerical integration scheme was implemented in Matlab®. Newmark-Beta is unconditionally stable [28] and was tested with fixed time steps between 7 and $20\mu s$. Different sampling rates for the actuation and measurement were also incorporated so that the measured signals could be filtered to reduce noise if necessary. Of particular interest was verifying the instabilities that occur when the control loop sampling rate was reduced below 7kHz.

Newmark-Beta integrated simulation results were consistent with those obtained using Simulink® and the closed-loop system was only stable when the control loop sampling rate was greater than 7kHz. Figure 7.13 shows the response of the closed loop system to the same perturbation at 5kHz and at 10kHz. At 5kHz the closed-loop system was unstable, while at 10kHz it is stable. For each case six plots are shown. The plots on the left consist of the dynamic response of the structure, while the plots on the right show the discrete controller inputs and outputs.

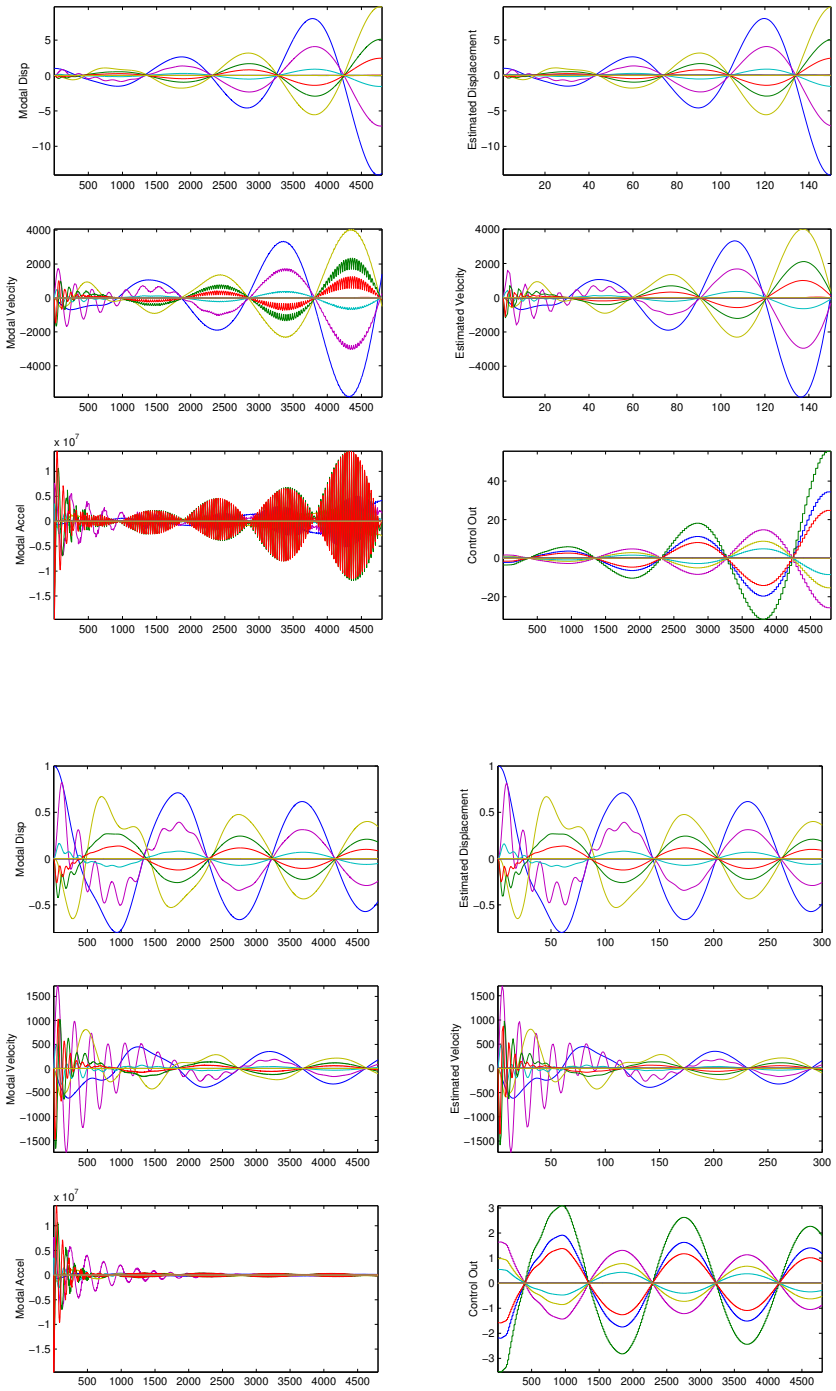

Figure 7.13 Newmark Beta results (5kHz at top and 10kHz below) where all plots are in units of modal amplitude. Each plot consists of the lowest twenty dynamic modes, of which modes 1,2 and 3 are blue, green and red.

7.7 Ramped loading simulations

The results presented in Section 7.6 indicate that the active control system can maintain the stability of the plate while under steady state compression at more than double P_{CR}. In practice, to reach this steady state load, the plate will have to dynamically pass through all the lower compression load states. The ability of the active stabilisation system to handle the transition from the region of stability below P_{CR} into the unstable buckling states around and above P_{CR} is of crucial importance. Also important is its performance during the ramp from P_{CR} up to the target steady state load P_{CL}.

A number of simulations were conducted to examine the performance of the active stabilisation system under different loading rates. In these simulations the compression loading process started from a steady state below P_{CR} and was ramped up continuously at a constant rate until buckling occurred. An initial condition consisting of an out-of-plane point load that forced the plate to assume a deformed shape similar to the first buckling mode was held constant throughout the compression loading ramp. This out-of-plane perturbation served as an imperfection to trigger buckling in these simulations.

Solving these ramped load cases was computationally expensive, as one simulation second required approximately ten hours of solution time on a 1.2 GHz Athlon with 768 Mbyte of RAM using the Simulink® based model. A starting load of 0.85 P_{CR} was used to reduce overall simulation time. In addition, a high loading rate was used in the first simulations to reduce computational time, but was gradually reduced in subsequent cases.

The results from the ramped simulations for a range of loading rates, in the presence of a noise power level of 10^{-10}, can be seen in Figure 7.14. These results demonstrate the active buckling control system's effectiveness for the intermediate load states in the region from P_{CR} to near P_{CL}. At the highest loading rate of

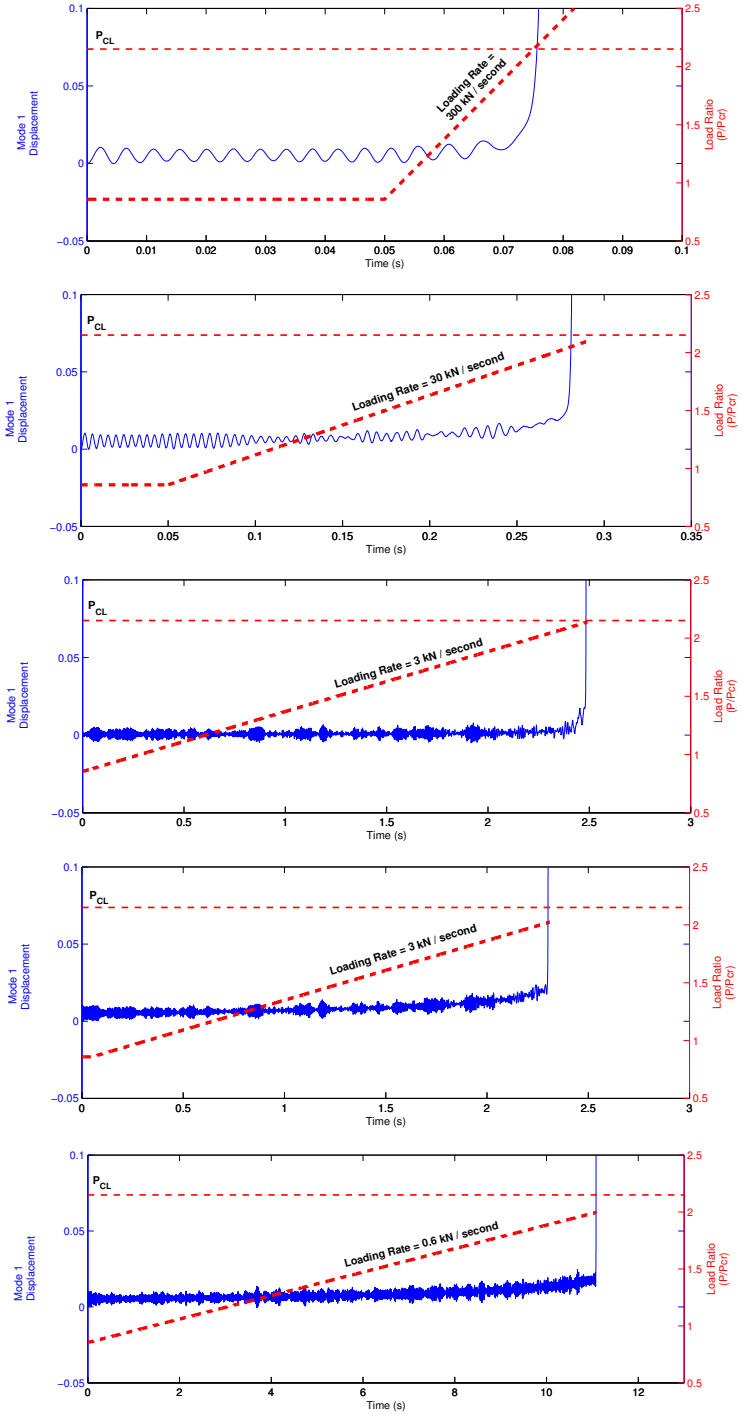

Figure 7.14 Results from ramped loading simulations for various loading rates and initial conditions. From top to bottom loading rates reduce from 300 kN/sec down to 0.6 kN/sec. There are two plots for the 3 kN/sec loading rate, corresponding to out-of-plane perturbation accelerations that differ by a factor of 10.

300kN/s, the design buckling load would be reached in 0.044 seconds. A buckling load slightly in excess of P_{CL} was achieved, but it is clear that there was a race between the buckling mode development and the application of load. At a much lower loading rate of 3kN/s it would take 4.4 seconds to reach P_{CL}. With a small imperfection the active plate reached a load very near P_{CL} before stability was lost, and even when the imperfection was increased by a factor of 10 the plate achieved a buckling load of about twice P_{CR}. At the slowest loading rate of 0.6kN/s the total loading time would still be well under a minute while the active plate buckling load with the larger imperfection was still about twice P_{CR}, so further reductions of the loading rate were not expected to affect the achievable buckling load.

7.8 Summary

Numerous simulations of active buckling control were performed, with the aim of predicting the likely success of anticipated experiments. The simulation model contained both continuous and discrete time elements to represent the continuous plant and the discrete controller. Practical limitations such as sensor noise, transport delay, finite sampling rates and actuator authority were investigated.

Results from the simulations show that by using four pairs of actuators, it is possible to control the first two buckling modes, which can result in buckling strength increases of up to 130 percent. Deflections will be measured via pairs of strain gauges bonded to the laminate surface. The results from ramped loading simulations add confidence that active buckling control of plates is possible.

Chapter 8

Active laminate plate strip specimen development

In order to validate the assumptions and theories used in the active plate modelling and simulation described in the preceding chapters, a simplified experiment was conceived based on active plate strips. This experiment was also intended to serve as a testbed for the development of the active control hardware and software that would be used in active buckling control of stiff structures. In addition it allowed a new load application mechanism and load control system to be evaluated for its suitability in testing the buckling of active plates and strips.

The active plate strip specimens used in these validation experiments can be visualized as vertical strips taken from the center 54mm of the active plate of Section 4.7. They differ from the plate described in Chapter 4 primarily in their reduced width and unconstrained sides. Note that effect of the lateral edge support conditions is local and therefore the behaviour of a vertical strip in the middle of the plate is not greatly affected by them. Also the number of sensors and actuators was reduced, as the objective was only to control the first buckling mode, which places an upper limit of 2.1 times P_{CR} on the achievable buckling load under active stabilisation.

8.1 Laminate construction

The laminate manufacturing technique was empirically developed through the construction of a number of plate specimens. All plates consisted of four plies; two of glass chopped strand mat (CSM) and two of unidirectional glass. Both polyester and epoxy resins were trialled.

The layup in Plate 1 consisted of CSM as the outer plies and unidirectional glass plies on the inside. A general purpose epoxy resin was used. The laminate was cured under vacuum, which improves compaction and reduces void content, ensuring more uniform material properties and improved repeatability. The conventional vacuum bagging technique was problematic as without a top mould surface it was difficult to achieve a uniform, accurate thickness over the entire plate. The thickness of Plate 1, which had a nominal thickness of 3mm, varied from 2.6 to 3.2mm. The density was measured as $1166kg/m^3$. Mechanical testing was performed on samples from Plate 1 to determine the tensile and flexural stiffness of the laminate. Results from this testing can be seen in Table 8.1.

Plate 2, and all subsequent plates used a polyester resin, as it provides a lower modulus combined with a higher strain to failure. High strain to failure is desirable for this application, as the specimen will undergo substantial deformation during repeated buckling experiments. A top and bottom plate were used to manufacture Plate 2 and Plate 3 with 3mm spacers between these two plates to control the laminate thickness. The vacuum resulted in extremely resin dry laminates as a substantial volume of resin was extracted during the curing of these two plates. These porous laminates did not have consistent properties and could not be used for active buckling control.

Vacuum curing was not used for Plate 4 and therefore the construction technique became similar to a moulding operation. The result was a high quality laminate, with a good surface finish and constant, accurate thickness. Longi-

Table 8.1 Results of mechanical testing on laminates.

Plate #	Layup	Direction	Inplane Modulus (GPa)	Flexural Modulus (GPa)	Resin
1	$[\text{CSM / Uni}]_S$	x	11	18	Epoxy
		y	4.5	4	Epoxy
4	$[\text{CSM / Uni}]_S$	x	12.5	6.5	Polyester
		y	4.5	5.5	Polyester

Figure 8.1 Plate 4 and the mechanical testing longitudinal and transverse specimens that were cut from it.

tudinal and transverse specimens for mechanical testing were cut from Plate 4 (Figure 8.1) and tested in the same way as the specimens for Plate 1. The results from their testing are also given in Table 8.1.

Material stiffness for individual plies can be estimated from the measured laminate stiffness using classical laminate theory (CLT) [29]. The simultaneous equation can be solved independently for both longitudinal and transverse stiffness:

$$\begin{bmatrix} t_{Uni} & t_{CSM} \\ I_{Uni} & I_{CSM} \end{bmatrix} \begin{bmatrix} E_{Uni} \\ E_{CSM} \end{bmatrix} = \begin{bmatrix} E_{Lam}t_{Lam} \\ E_{Lam}I_{Lam} \end{bmatrix} \tag{8.1}$$

where E is the modulus (flexural or in-plane), t is the thickness and I is the second moment of area. Given the measured stiffness for Plate 4, which had a measured thickness $t_{Lam} = 3.4mm$, and using the manufacturer supplied ply thicknesses: $t_{Uni} = 1mm$ and $t_{CSM} = 2.4mm$, it is possible to solve for E_{CSM} and E_{Uni}:

$$\begin{aligned} E_{CSM_{Long.}} &= 5.7GPa & E_{Uni_{Long.}} &= 28.8GPa \\ E_{CSM_{Transv.}} &= 5.7GPa & E_{Uni_{Transv.}} &= 1.6GPa \end{aligned}$$

These results were used to predict laminate properties when the layup was re-ordered or ply thicknesses were changed. Plates 5, 6 and 7 were manufactured to achieve the same mechanical properties as Plate 4, using the same method. Specimens were cut from these additional plates and used for buckling and active control experiments.

8.1.1 Layup design and materials

During plate design certain laminate mechanical properties were chosen which are listed in Table 4.7. A layup with these laminate properties was required so that the experimental plate strips matched the finite element model and the simulations. Given the relatively low stiffness required, glass reinforced laminates constructed using a wet layup process were the only option. Table 8.2 lists the in-plane and flexural stiffness properties, either estimated using CLT theory or measured through mechanical testing. Table 8.2 presents these laminates in the order that the layup was incrementally developed.

Figure 8.2 shows the stiffness calculated using CLT for several layups including the effect of the embedded PZT actuators. The reference plate profile is

Table 8.2 In-plane (E) and flexural ($\hat{E}$) stiffness results for various glass reinforced plate layups and materials. Plates a, b and c are modelled, while plates 1 and 4 were mechanically tested.

Description	Resin	Layup	E_X (GPa)	E_Y (GPa)	$\hat{E}_X$ (GPa)	$\hat{E}_Y$ (GPa)
Required properties	N/A	N/A	15.0	5.0	15.0	5.0
Plate a: designed (CLT)	Epoxy	$[\text{CSM/Uni}]_S$	14.5	6.8	7.5	6.7
Plate b: designed (CLT)	Epoxy	$[\text{Uni/CSM}]_S$	14.5	6.8	21.0	5.8
Plate 1: tested	Epoxy	$[\text{CSM/Uni}]_S$	11.0	4.5	18.0	4.0
Plate 4: tested	Polyester	$[\text{CSM/Uni}]_S$	12.5	4.5	6.5	5.5
Plate c: designed (CLT)	Polyester	$[\text{Uni/CSM}]_S$	12.5	4.5	16.2	3.0

based on measured properties for Plate 4, but the plies have been reordered. It was desired to have the longitudinal stiffness where the actuator is embedded the same as in the passive sections of the plate, and profile 2 achieves this goal.

8.1.2 Laminate manufacturing technique

A manufacturing method was developed to provide laminates of suitable characteristics to be used for active buckling control. Two stiff and polished plates of aluminum were used for the lower and upper mould surfaces. The plate used as the lower mould was approximately 1200 x 370 x 15mm and the upper plate 400 x 330 x 10mm. The plates were separated by 3mm spacers along their longer sides which controlled the thickness of the laminate. The laminate thickness was slightly larger than that of the spacers as glass strands and resin would always get caught between the contact surfaces. It was found that by having the two ends open (without spacers) it was much easier to roll the laminate and allow excess resin to flow out at the ends. Figure 8.3 shows Plate 7 curing in the mould. Approximately 500mls of resin was required to wet out a laminate of dimensions 400 x 300 x 3mm.

The specific manufacturing procedure is as follows:

1. The two plate mould surfaces were initially cleaned using acetone. Four coats of Frekote®releasing agent were subsequently applied and allowed to

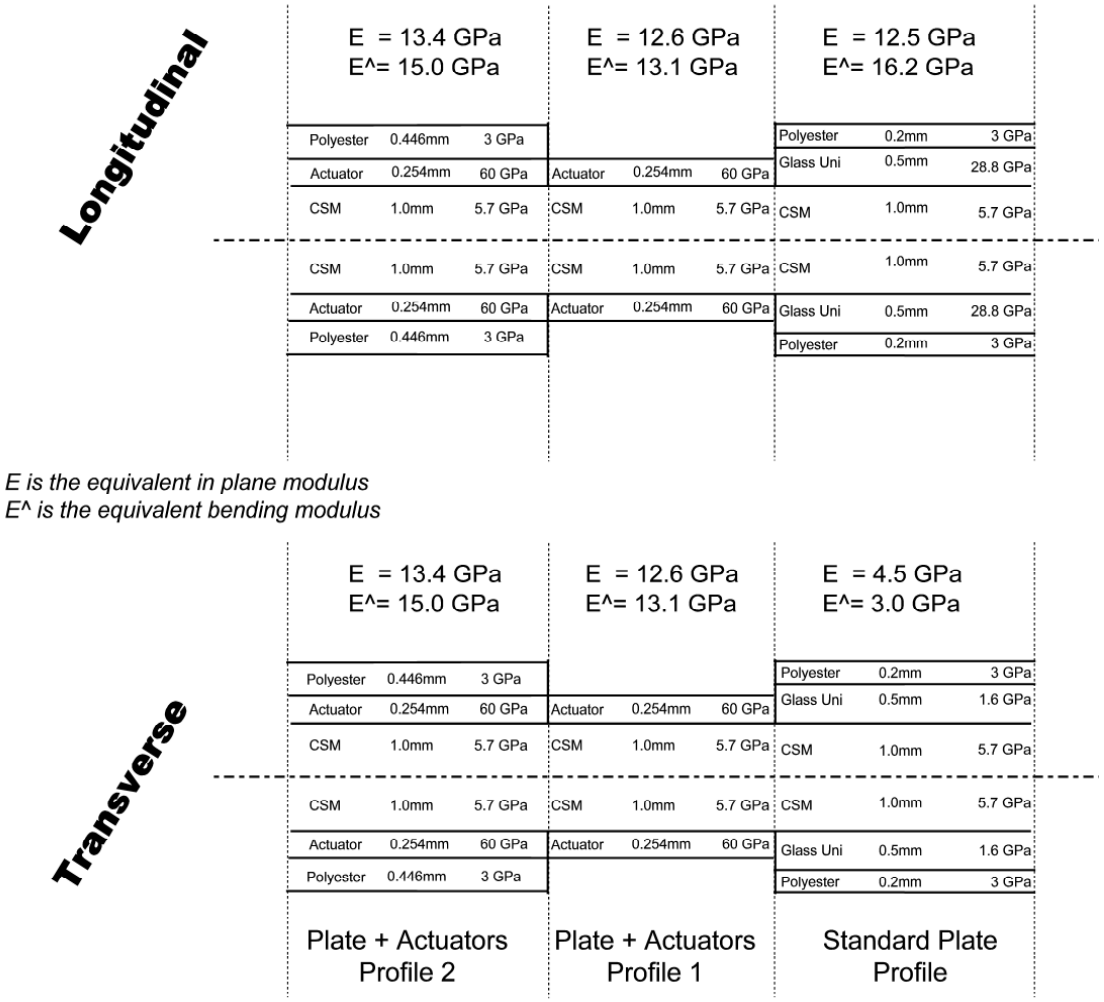

Figure 8.2 Schematic showing results for in-plane and flexural stiffness based on CLT calculations for the standard laminate and two additional layups with embedded actuators. Longitudinal results are shown at the top, and transverse below.

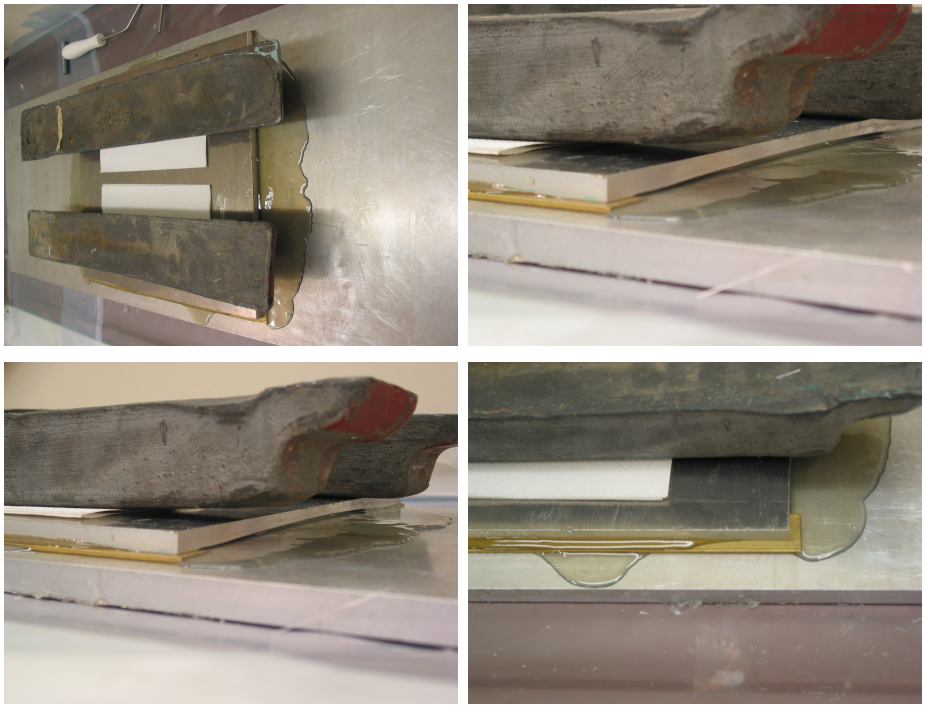

Figure 8.3 Laminate plate construction.

dry to ensure the laminate did not adhere to the mould.

2. The four glass plies were cut to approximately 400 x 300mm and equipment prepared before measuring resin and catalyst.

3. Three batches of resin (200ml) were measured, along with 0.6 percent catalyst (by weight), which provided a working time of around 20 minutes. Using multiple batches allows staggering of the time when different batches will gel, ensuring the resin still flows when the final plies are layed.

4. The lower mould surface was coated with resin to minimise voids present in the laminate surface. Individual plies were then placed, resin applied, and carefully rolled to spread resin and remove voids.

5. The top plate mould surface was also coated with resin before being placed upon the laminate. Approximately 40kg of weight was used to compress

the laminate. This ensures the thickness is correct and that excess resin is removed.

6. The laminate was left in the mould at room temperature for 7 days. This was to ensure that no warpage would occur in the plate after removal. The cure can be cured at temperature to reduce time but it must remain in the mould, otherwise warpage is likely to occur.

8.1.3 Manufactured plate specifications

After perfecting the manufacturing technique Plate 6 was used for subsequent experimentation. Three plate strips of dimensions 252 x 54mm were cut from the plate and actuators and sensors were added. Once cut from Plate 6 the three plate strips were labelled 6.1, 6.2 and 6.3. After actuators and gauges had been added the three active plate strips were designated A, C and B, in the order of their construction. Actuator embedding was achieved by machining cavities into the laminate and using a two part epoxy resin to bond actuators to the surface. Strain gauges were secured using Micro Measurements MBond 2000 cyanoacrylate adhesive. Table 8.3 lists the active plate strip properties and Table 8.4 the mechanical properties of Plate 6 estimated using CLT. The flexural moduli, which have a greater influence on buckling behaviour, can be compared to the desired orthotropic values from the active plate design: $E_X = 15$GPa and $E_Y = 5$GPa. Although Plate 6 is stiffer than desired in the longitudinal direction, it is slightly more flexible in the transverse direction. Small changes to the laminate definition result in large changes to the mechanical properties of the laminate and therefore Plate 6 is considered to be an acceptable approximation of the designed orthotropic plate.

Table 8.3 Common properties of active plate strips.

Material	Glass fibre with polyester resin
Layup	[Uni/CSM/CSM/Uni]
Laminate thickness	2.90 ± 0.05 mm
Nominal dimensions	207 x 54 mm
Catalyst level	0.6% by volume
Density	$1474 kg/m^3$

Table 8.4 Estimated laminate properties of active plate strips using classical laminate theory.

Ply thickness:	CSM	0.95	mm
	Uni	0.50	mm
Flexural Modulus:	$\hat{E}_X$	23	GPa
	$\hat{E}_Y$	2.9	GPa
In-plane Modulus:	E_X	13.7	GPa
	E_Y	4.5	GPa

8.2 Specimen description

Three plate strips were cut from Plate 6, as discussed in Section 8.1.3, to develop into active experimental specimens. Each had dimensions of 252 by 54mm. The test section length was 207mm, leaving 22.5mm at each end for clamping. These plate strips have an aspect ratio of approximately 4:1 so they are not pure Bernoulli bending columns, and will share some characteristics with plates.

8.2.1 Plate Strip A: Embedded actuators & strain gauges

Plate Strip A incorporates embedded Midé ACX QP10W Actuators and high sensitivity silicon strain gauges. The actuators are embedded to achieve a uniform flexural rigidity across the entire specimen. Cavities for the actuators were symmetrically machined into each face of the plate strip, and the actuators were bonded using an epoxy adhesive. Incorporating the actuators into the layup during the laminate manufacture was not attempted as it would have been very

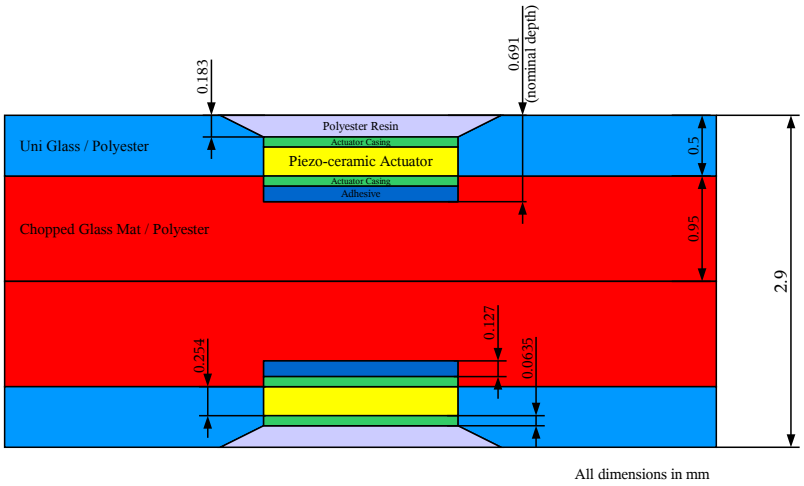

Figure 8.4 Schematic of Plate Strip A cross section at actuator location, showing actuator embedding details.

difficult to achieve accurate placement, especially in the through thickness direction, due to the wet layup process used in the laminate manufacture.

Figure 8.4 shows the cross section of the laminate at the actuator location, showing the embedding depth required to achieve uniform flexural stiffness over the plate. Adhesive and actuator encasing have also been included as they have same order of magnitude thickness and were considered during equivalent stiffness calculations. Figure 8.5 shows the plate strip at different stages of construction.

A pair of BLH SR-4 silicon strain gauges were bonded to the plate strip surface at both ends, approximately 5mm in from the clamp, one on each side of the laminate. The largest magnitude bending strain for a fixed-free plate strip will occur at the very end by the clamp, but this was not considered a suitable location for gauges due to the local 3D stresses around the clamp. The gauges have a nominal resistance of 1.17 kOhm, and a gauge factor of 143.7.

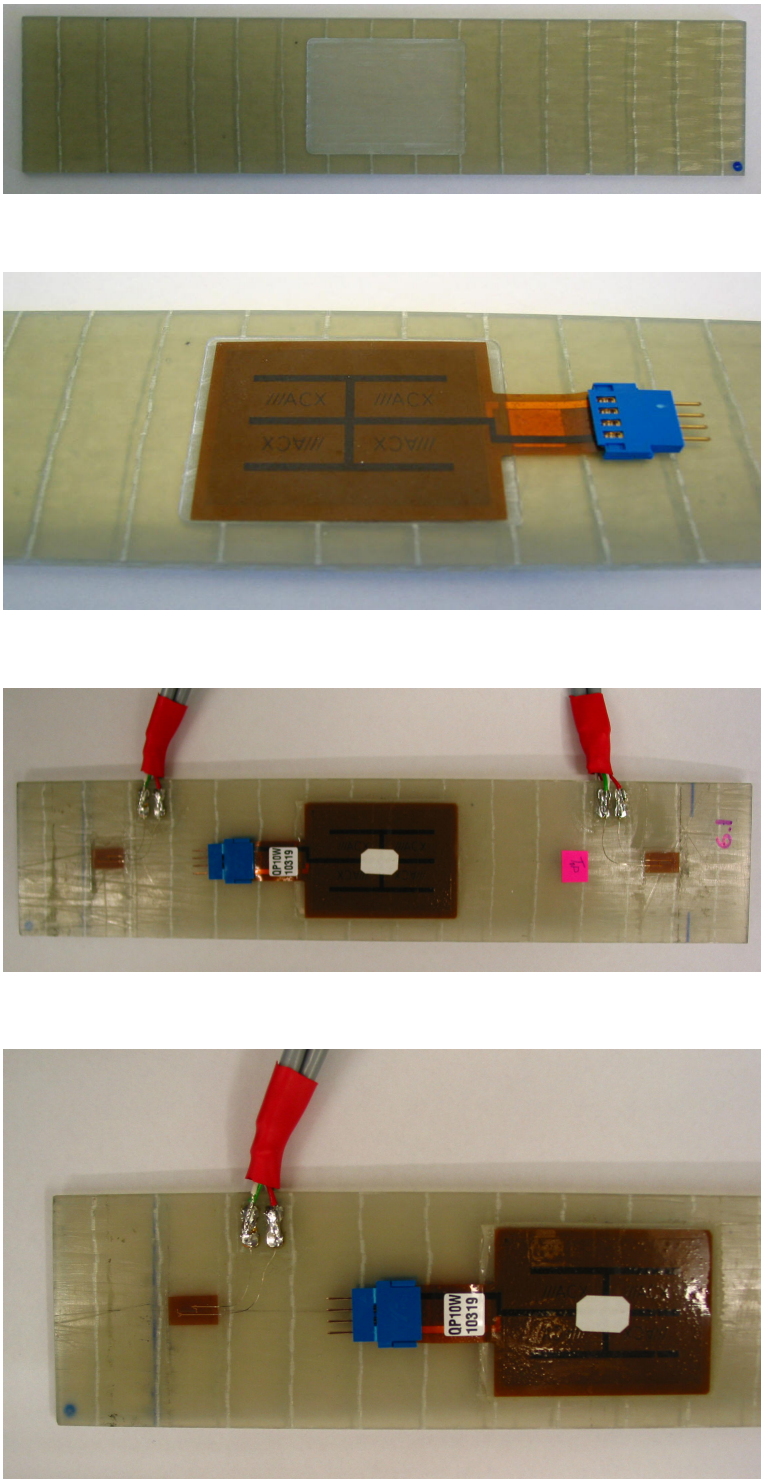

Figure 8.5 Photos of Plate Strip A during construction, starting with the machined blank at the top to the finished active plate strip at the bottom.

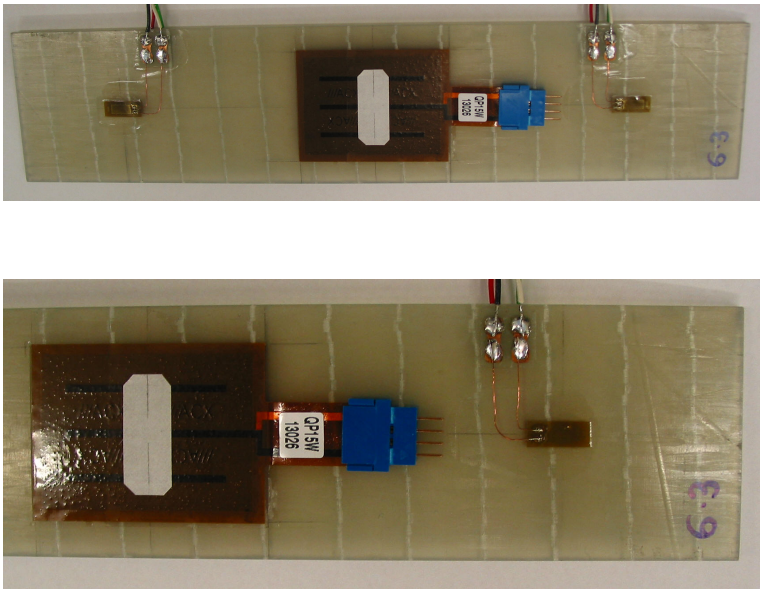

Figure 8.6 Photos of Plate Strip B illustrating actuator and strain gauge mounting.

8.2.2 Plate Strip B: Surface mounted actuators & strain gauges

The Midé ACX QP15W actuators used on Plate Strip B were bonded to the surface as shown in Figure 8.6. These actuators were half the thickness of the QP10W actuators used in Plate Strip A and were therefore rated to half the driving voltage. The available blocking moment has been reduced by approximately 23 percent when compared to Column A. The lower voltage range is beneficial as the amplifier (with a constant slew rate) will be able to traverse the full range faster, effectively increasing actuator responsiveness at higher frequencies.

Conventional metal foil strain gauges (Micro Measurements S2K-00-125AC-10C) were attached to Plate Strip B, and were approximately 70 times less sensitive then the silicon gauges used on Plate Strip A. The expected resolution is approximately $5\mu\varepsilon$. The gauges were wired in a half bridge configuration, so that the range is not reduced by the in-plane strain component, which at up to $5800\mu\varepsilon$ is 50% of full output range.

As the actuators are not embedded, the plate strip no longer has a constant flexural stiffness and is stiffer in its center region. This increase in stiffness results in increased buckling loads and dynamic frequencies compared to the finite element model. Although the load and frequencies will increase, the lower mode shapes remain essentially the same. The specimen end clamps used in testing on Plate Strip C and B were redesigned to remedy some of the alignment concerns found with the initial setup for Plate Strip A. Section 9.1.3 details these changes.

8.2.3 Plate Strip C: Twin actuators and displacement sensor

The actuator used for Plate Strip C had substantially increased authority, compared to those used in the previous two plate strips. The Midé ACX QP-20W actuators have two separate vertically stacked PZT wafers in each actuator as shown in Figure 8.7, which can be driven independently. The actuators are mounted on the surface. No strain gauges were included in this plate strip as the control system used the capacitive displacement sensor to measure the central out-of-plane deflection. Hence, one set can be used primarily to eliminate offset in the plate strip leaving the actuator authority of the remaining pair to be devoted to controlling buckling.

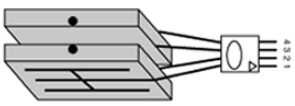

Figure 8.7 Schematic of Midé ACX QP20N Actuator with two PZT wafers encased in a single actuator. Image has been reproduced from the ACX catalogue.

Table 8.5 Properties of plate strip finite element model.

Dimensions	207 by 54 mm
Thickness	2.9 mm
Material Properties	E_X=23 GPa, E_Y=2.9 GPa
	G_{XY}=2.5 GPa, $\upsilon = 0.27$
Density	1474 kg/m^3
Boundary Conditions	Ends: Fixed, Sides: Free
Element Size	4.5 mm square
Damping Parameters	Frequencies: $w_1 = 100$, $w_2 = 25000$
	Damping Ratios: [0.18, 0.25]
Actuator Authority	0.0462 Nm per node (embedded QP10W)
	0.0356 Nm per node (surface QP15W)

8.3 Finite element model

The finite element model used for plate strip buckling simulations is based on the plate model, with several modifications:

- Width reduced to 54mm
- Lateral boundary conditions released (i.e. unloaded sides are free)
- Actuator and sensor configuration adapted to mode shape

The parameters used in the finite element model are listed in Table 8.5. The critical buckling loads, dynamic frequencies and mode shapes of the model can be seen in Table 8.6 and Figures 8.8 and 8.9. The actuator moment was spread over nine nodes so that each of the inner nodes see 0.0425Nm and the two outer nodes 0.0213Nm, as explained in Section 7.4.

Table 8.6 Results of plate strip finite element analysis.

Dynamic Frequency	1	276	Hz
	2	487	Hz
	3	760	Hz
	4	1089	Hz
	5	1490	Hz
Buckling Load	1	43.3	kN/m
	2	88.6	kN/m
	3	141.3	kN/m

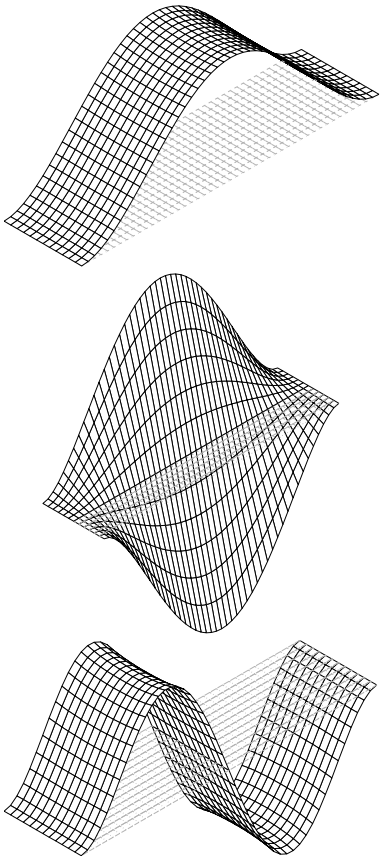

Figure 8.8 Plate strip model mode shapes for the first three dynamic modes, from mode 1 at the top to mode 3 at bottom.

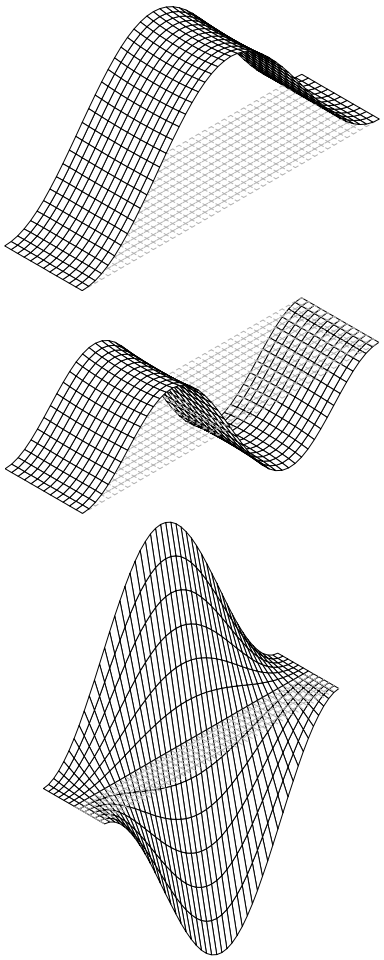

Figure 8.9 Plate strip model mode shapes for the first three buckling modes, from mode 1 at the top to mode 3 at bottom.

Table 8.7 Parameters used for plate strip control optimisation.

Desired load ratio $\frac{P_{CR}}{P_{CL}}$		1.5
Number of modes (contraction)		20
Optimisation weights:	α	1
	β	1
	γ	1000

8.4 Plate strip control optimisation

The plate strip controller was optimised with a desired load ratio $\left(\frac{P_{CR}}{P_{CL}}\right)$ of 1.5, and actuator placement as shown in Figure 8.10. The result of this optimisation was a closed loop critical load of 88.6kN/m, which corresponds to a load ratio of 2.05. This closed loop load is the upper limit to what could be achieved through controlling only the first mode, as it corresponds to the open loop second buckling mode load. The closed loop mode shapes can be seen in Figure 8.11 and the parameters used for optimisation are given in Table 8.7. Figure 8.12 shows the plane-strain deformation for the fundamental buckling mode, which was used to determine strain gauge locations and orientations.

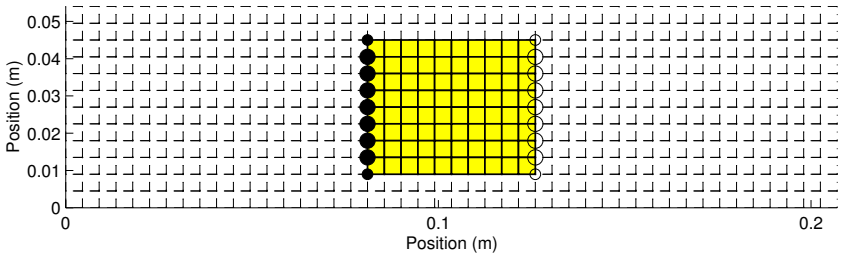

Figure 8.10 Actuator location on plate strip model where circles represent nodes where actuator generated moment is applied to the model. Filled circles represent positive moments, while hollow circles represent negative moments. The diameter of the circle is representative of the magnitude of the moment applied.

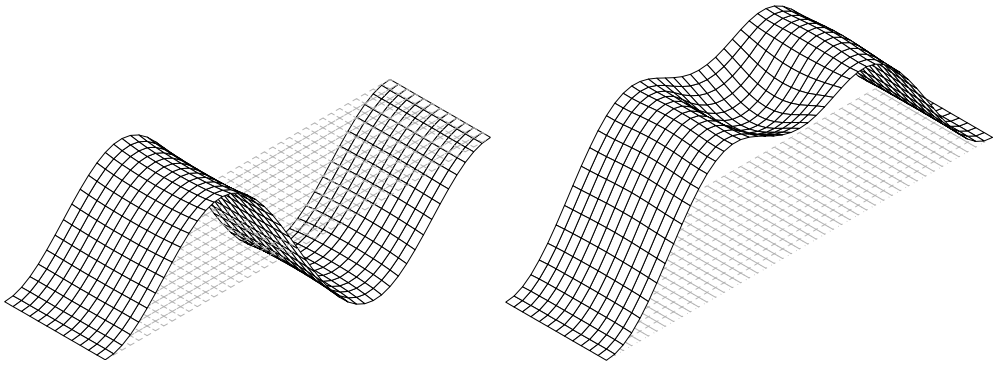

Figure 8.11 Deformed shapes for the first (88.6kN/m) and second (101.2kN/m) closed-loop buckling modes (left and right).

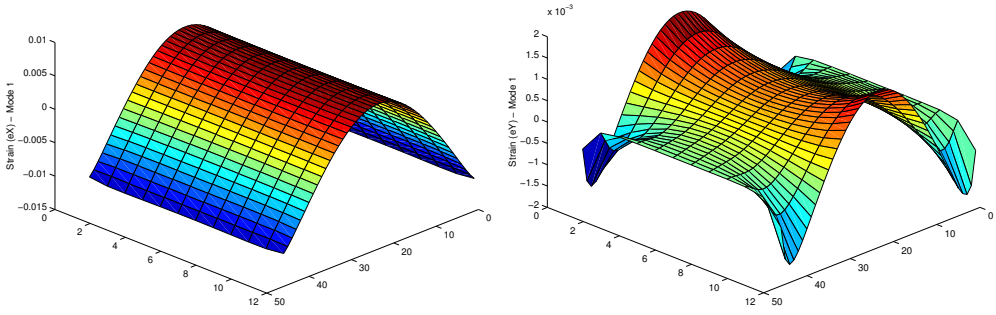

Figure 8.12 Lowest buckling mode strain components; ε_X (longitudinal) and ε_Y (transverse).

8.5 Simulation results

8.5.1 Plate Strip A

A control simulation was performed on Plate Strip A to ensure that the optimised controller could be successfully implemented given the hardware available. Table 8.8 shows the parameters used in this simulation. This simulation assumes the amplitude of mode one can be measured.

Table 8.8 Plate Strip A: Control simulation parameters.

Noise Power	5×10^{-11}
Actuator Authority	± 0.0462 N/m
Control Sampling Rate	10 kHz
Simulation Duration	0.25 seconds

The assumed noise power of 5×10^{-11} is equivalent to an amplitude of $10\mu\varepsilon$ in strain measurement, which is a conservative estimate. An initial transverse displacement imperfection equal to 5% of the plate strip thickness was assumed. The simulation proved to be stable up to 89kN/m, which is equal to the designed closed loop limit.

8.5.2 Plate Strip B

Dynamic simulations were performed on Plate Strip B to predict experimental performance. Two sets of results are presented.

The first set assumes 100% of the actuator rated force is available and the second assumes 20%. The lower actuator authority range represents the case where 80% of the actuator authority was required to constantly correct for an initial curvature in the plate strip. In these simulations it is the central out-of-plane deflection that is used as the sensor input. The noise level in this measurement is assumed to be $\pm 7.5\mu m$, which corresponds to a noise power of 10^{-15}. Table

Table 8.9 Plate Strip B: Control simulation parameters.

Noise Power	1×10^{-15}
Actuator Authority (100%)	± 0.0356 N/m
Optimised Load	70 kN/m ($1.62P_{CR}$)
Control Sampling Rate	50 kHz
Simulation Duration	0.25 seconds

8.9 shows the parameters used in the simulations. The results of these two simulations can be compared in Table 8.10 and Figure 8.13. Reducing the actuator authority to 20% is seen to have a large negative impact on the performance of the control system, with a drop to $\frac{P}{P_{CR}} = 1.28$.

Table 8.10 Results showing effect of lower available actuator authority due to initial constant voltage offset required to correct for initial curvature.

	Uncontrolled	20% Actuation	100% Actuation
P_{CR} (kN/m)	43.3	55.5	70
$\frac{P_{CL}}{P_{CR}}$	1.00	1.28	1.62
Max Init Disp (mm)	0	0.001	0.1
Max Init Vel (mm/s)	0	10	50

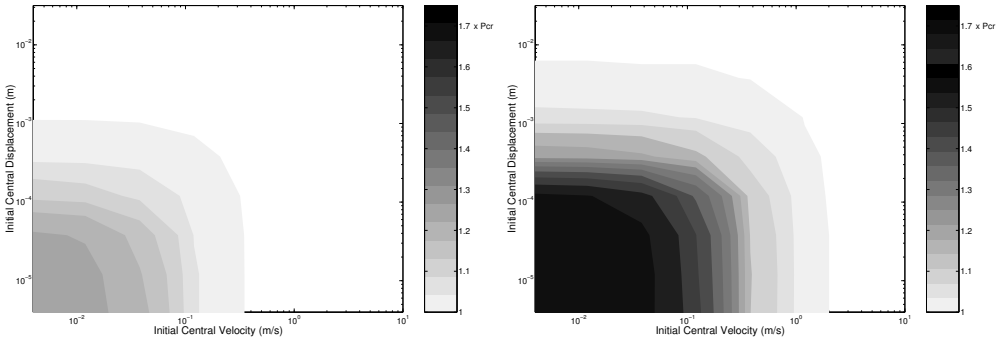

Figure 8.13 Plate Strip B: Simulation results for 20% (left) and 100% (right) actuator authority.

8.5.3 Frequency response analysis

The frequency response of the system, between the actuator input and sensor output, was simulated and subsequently measured using a white noise source and a spectrum analyser. This approach allowed comparison of the simulation model to the experimental system, which included transport delay through hardware. The gain and phase margins were determined to estimate the stability of the closed-loop system. A detailed explanation of the role of frequency response analysis in control system design is provided by Franklin [30]. Theoretically, it is enough that both the phase and gain margins be positive for stability. In practice a phase margin of more than 30° is considered desirable.

Figures 8.14 and 8.15 show the uncontrolled and controlled modelled frequency responses for the unloaded and loaded cases. The loaded case incorporates a load P=1.5P_{CR}, which is greater than the open-loop buckling load, but less than the closed-loop buckling load. The loaded but uncontrolled case should therefore be unstable as it is loaded past the critical load, while all other cases should be stable. Both figures use the central OOP deflection as a feedback error signal.

For the unloaded cases shown in Figure 8.14 the phase margin for the uncontrolled case is 7° and the gain margin is undefined as the phase does not fall below −180°. The unloaded and uncontrolled system is therefore stable as expected. The unloaded and controlled system is also stable with an improved phase margin of 18°, which is also as expected. The effect of control is to increase the stability and damping as seen in the increased phase margin. When a compressive load larger than the critical buckling load is applied, the uncontrolled case (Figure 8.15) becomes unstable. The phase margin reduces to 0°, and the gain margin to 0dB. As expected, the controlled case remains stable at this load with a phase margin of 20°.

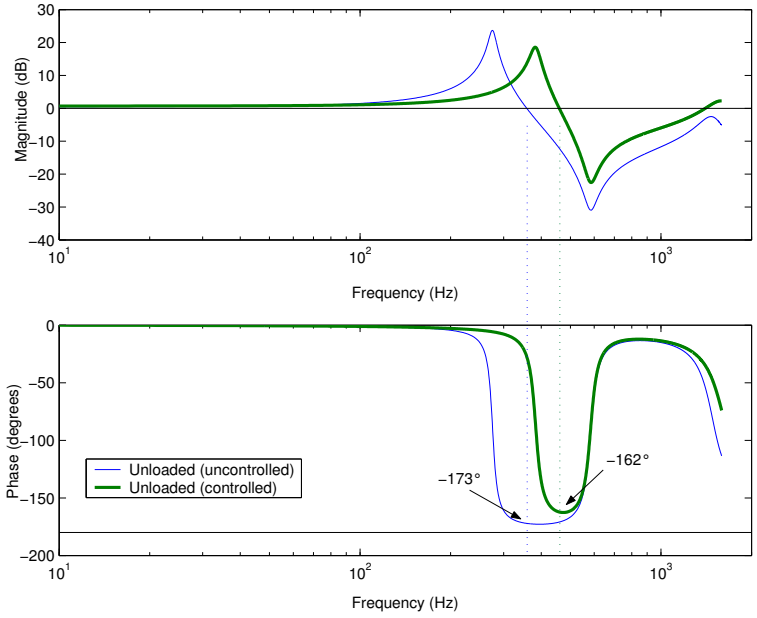

Figure 8.14 Controlled and uncontrolled simulated frequency response for an unloaded plate strip.

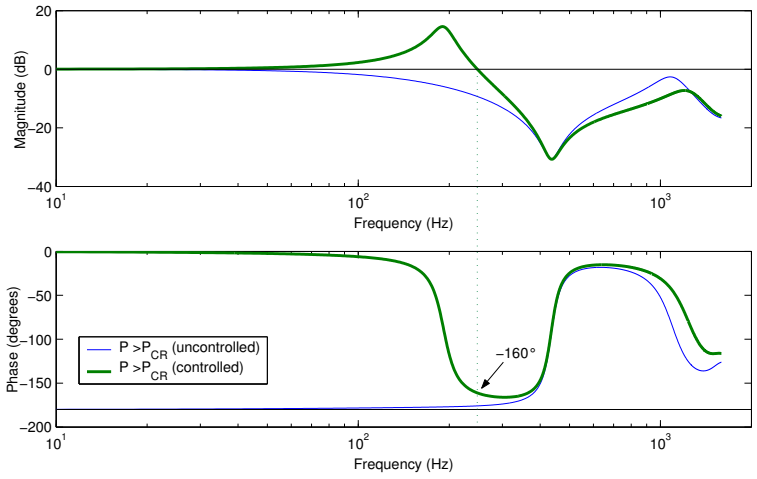

Figure 8.15 Controlled and uncontrolled simulated frequency response for a plate strip loaded in compression (P=1.5P_{CR}).

Chapter 9

Experiment design and construction

9.1 Compressive loading system design

A custom test rig for the compressive loading of active plate strips was built and required considerable design given the large loads required. Traditional compressive loading rigs consist of a sliding hydraulic or motorised screw crosshead. The sliding crosshead is usually located using expensive, precision linear bearings. Bearing stiction in this design is always a concern and can introduce jolts that make active control of an unstable system much more difficult. Compressive testing is also very intolerant of loading misalignment, as even a small off-axis loading will cause an initial curvature, which would dramatically reduce the effective compressive strength of the specimen.

The design that was developed for this research utilised a hinging crosshead to eliminate the need for sliding parts. A hinging system approximates in-plane loading for small end displacements, as the angle of loading is related to the hinge length and the crosshead displacement. For this application it was found that a crosshead displacement of less than $1mm$ was required to load the active plate strips to the designed closed-loop buckling loads. Figure 9.1 shows a concept sketch of such a test rig for a plate specimen.

Table 9.1 lists plate strip details and loading rig requirements for several active plate designs. Important figures are the equivalent end deflection of the

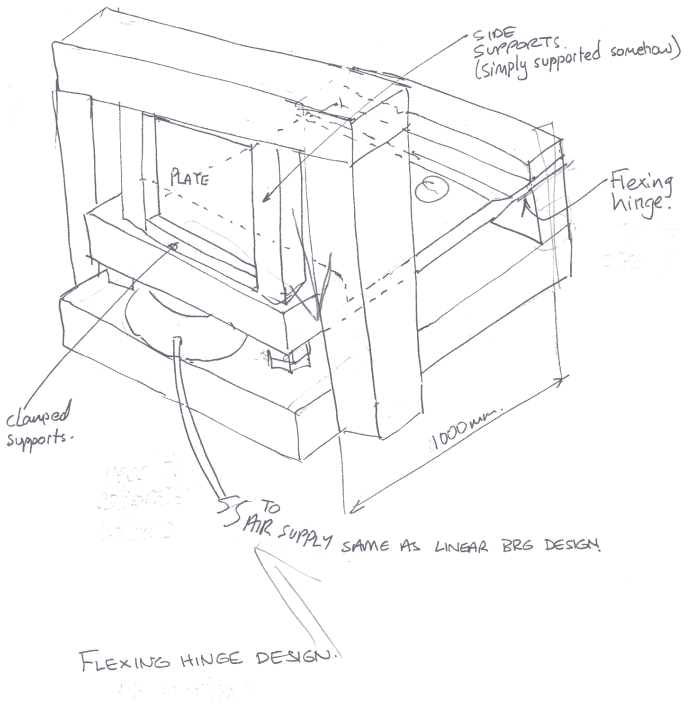

Figure 9.1 Test rig concept.

specimen under load, which dictates the maximum crosshead displacement, and the third mode buckling load, which is the maximum force required if control of the first two modes is achieved. The maximum force required and crosshead displacement can be seen to be in the range of $10 - 22kN$ and $1.8 - 2.8mm$ respectively.

It is desirable to have load based control for the compressive loading system as displacement based control might encounter problems around buckling loads and when interacting with the active stiffness controller operating on the plate strip. A pneumatic bellow was chosen for rig actuation as it will apply a relatively constant load, independent of small changes in bellow extension that may occur due to buckling and active control of the plate strip. The maximum loads required for the plate model are achievable from pneumatics, but are near the upper limit given standard line pressure and size constraints. The simplicity of a passive load

Table 9.1 Loading and deflection requirements of the loading rig.

	Nominal	Flexible Layup	Stiff Layup	Stiff Layup II
Thickness (mm)	3	3.4	3.4	3
Width (mm)	200	200	200	200
Length (mm)	300	300	300	300
In plane stiffness (GPa)	15	12.5	12.5	13.7
(kN/mm)	30.0	28.3	28.3	27.4
Out-of-plane stiffness (GPa)	15	6.3	16.2	22.2
Mode 1: Buckling load (kN)	5.82	5.84	7.96	6.48
Equivalent end disp. (mm)	0.194	0.206	0.281	0.236
Mode 3: Buckling load (kN)*	14.24	10.56	21.8	17.54
Equivalent end disp. (mm)**	0.475	0.373	0.769	0.640
BL3 / BL1	2.45	1.81	2.74	2.71

* Maximum force required
** Maximum stroke required

control system, such as pneumatic bellows, is an additional desirable feature.

9.1.1 Plate buckling reaction forces

A nonlinear buckling analysis was performed in Ansys®to determine the order of magnitude of the reaction forces and displacements that must be accommodated by the entire loading rig during operation. The loads were initially estimated using a linear buckling analysis, whose results are listed in Table 9.2. There are two main components to the overall reaction forces:

The first requirement is the out-of-plane force (FZ) which is transmitted from the plate to the support structure due to buckling deformation. This load will be spread over both the side and end constraints. Assuming control of the lowest two modes is successful, the nonlinear model has been perturbed with initial out-of-plane (OOP) loads that resemble the third mode shape, and has been constrained in the transverse direction at the center. The initial perturbation and resulting buckling mode can be seen in Figure 9.2, and the results from this analysis can

Table 9.2 Buckling load results from linear analysis.

Open Loop:	Mode 1	8	kN
	Mode 2	12.4	kN
	Mode 3	21.8	kN
Closed Loop:	Mode 1	17.7	kN

be seen in Table 9.3. The OOP loads are small at less than 100N and therefore will not require specific design detail. This analysis also shows an end load (FX) of 21.76kN which is the applied compressive load and corresponding reaction load at the two ends of the plate. A moment (MY) of 17.3Nm will need to be accommodated at each end constraint to ensure a fixed-fixed boundary condition is approximated.

Second, as the plate is simply supported along the unloaded edges it will expand across its width due to Poisson's ratio coupling these strains. A nonlinear analysis was performed on a flat plate with no perturbation to estimate this expansion. The plate was loaded to the critical load for the third mode, and the results are given in Table 9.4. The schematic in Figure 9.3 summarises the reaction loading requirements for the rig. To achieve the desired compressive load the plate contracts 0.66mm along its length and expands 0.12mm across its width. This free expansion across the width of the plate will need to be accommodated

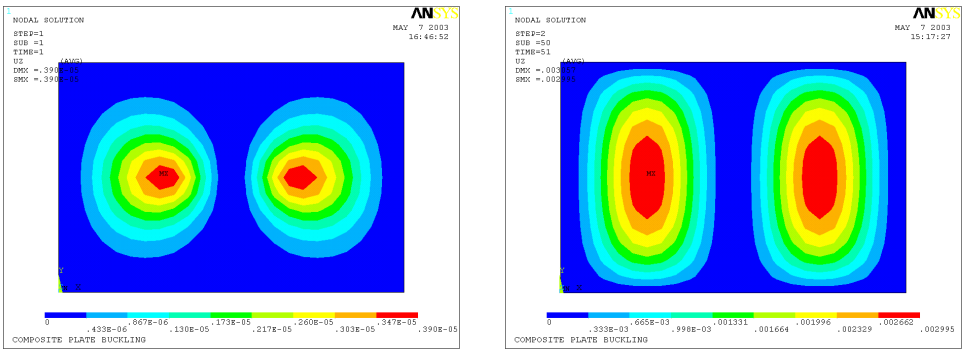

Figure 9.2 Resulting OOP deflection for nonlinear analysis with the initial perturbation (left) and final buckled deflection (right).

Table 9.3 Resultant forces on support structure at full load.

Maximum Loading Point:	Applied Load	21.76	kN
	UX	0.82	mm
	Max UZ	3.0	mm
	Max UY	0.0426	mm (center of each side)
Required Support Loads:			
End 1	FX	21, 764	N
	FZ	54	N
	MY	17.3	Nm
End 2	FX	-21, 764	N
	FZ	54	N
	MY	-17.3	Nm
Side 1	FZ	-72.8	N
Side 2	FZ	-72.8	N

** *The plate buckled after 36 seconds, when the load was 18.95kN*

within the rig so that no reaction force is applied in the transverse direction.

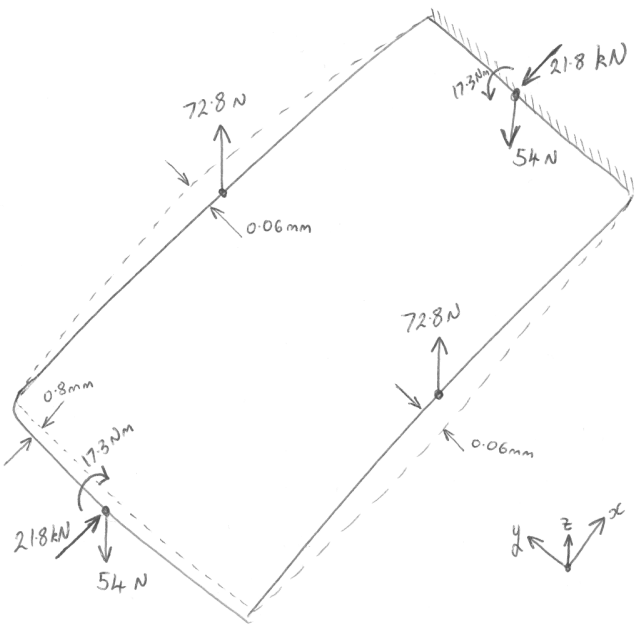

Figure 9.3 Summary of loading support forces.

Table 9.4 Results from nonlinear analysis of the loaded plate when no OOP perturbation is applied.

Applied Load	21.79	kN
End Compression	0.66	mm
Central OOP Deflection	0	mm
Side Expansion (each side at center)	0.0592	mm

9.1.2 Plate strip loading frame

Prior to construction of the plate strip loading rig, which applies fixed-free plate constraints, a more detailed analysis of the loading mechanism was performed. The nonlinear model in this analysis included both the plate strip and the loading rig hinge. This expanded model allowed the dimensions of the hinge to be optimised to avoid premature buckling due to a poor approximation of a fixed end constraint. The plate strip model was built using a laminate material definition to best approximate the actual plate strip. The finite element model of the laminate plate strip and steel hinge can be seen in Figure 9.4.

The result of a series of analyses was a hinge that incorporated a stepped thickness. The central region of the hinge, which is lightly shaded in Figure 9.4, has a thickness of $10mm$, while the outer area is $1mm$. This feature minimised rotation of the central region that otherwise caused premature buckling. The hinge extends 800mm in both directions from where the plate strip is clamped, and each end is fixed. The flexibility conferred by the thin section of the hinge lowers the overall hinge stiffness so that the majority of the load applied is transferred to the plate strip, rather than out through the hinge.

The maximum required loading for the plate strip as designed is 5kN. This value is approximately the second mode critical buckling load, assuming that the first mode is successfully controlled. The nonlinear model was loaded to this limit, and the plate strip perturbed to approximate the resulting defection and stress. Figure 9.5 displays the resulting deflections if the plate strip buckles. The

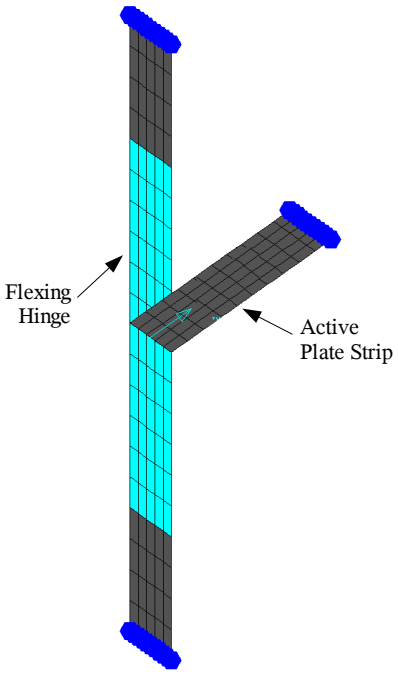

Figure 9.4 Nonlinear finite element model of the composite plate strip and the steel support hinge (vertical), where the lighter shaded region illustrates an area of increased thickness.

hinge was also analysed to ensure that it could withstand the entire 5kN load in the case that the plate strip failed. It was found that mechanical stops would need to be incorporated to restrain the hinge from taking the entire load as it would otherwise fail.

After the hinge design was optimised the surrounding support structure was designed using standard steel sections. A solid 3-D model of the resulting loading rig was created and used for manufacture. The solid model can be seen in Figure 9.6 and the loading rig as constructed in Figure 9.7.

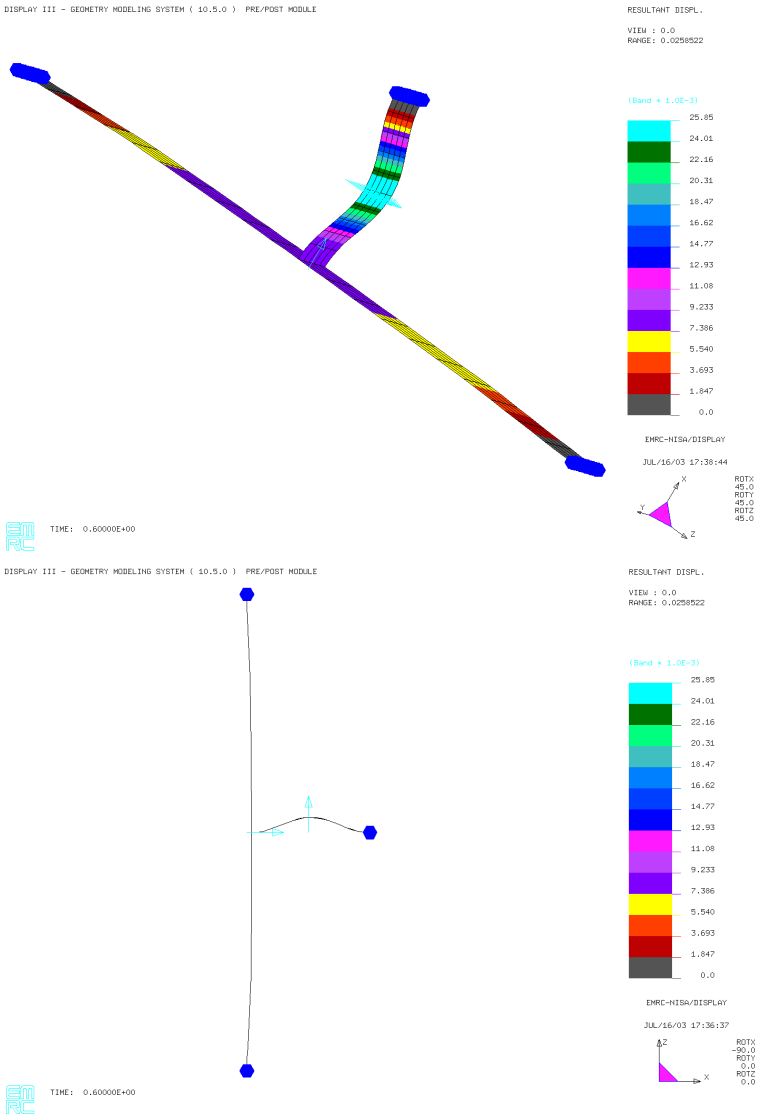

Figure 9.5 Resultant deflection of plate strip and hinge for nonlinear finite element analysis.

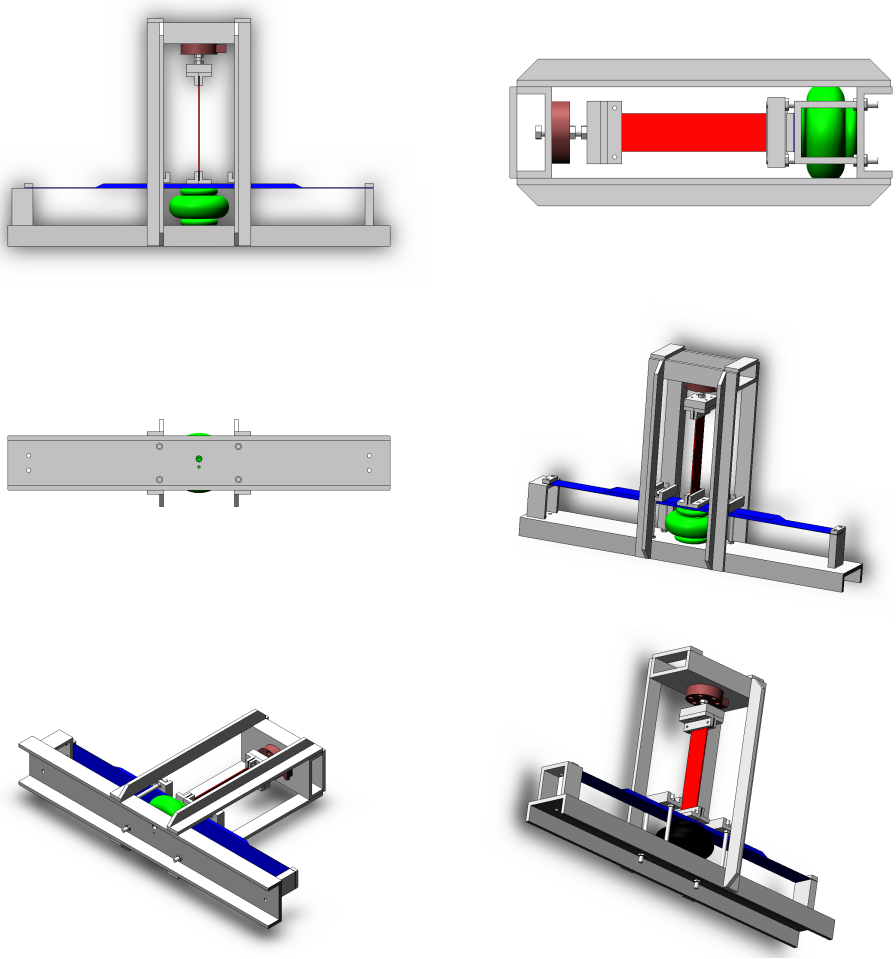

Figure 9.6 Solid model of buckling test rig.

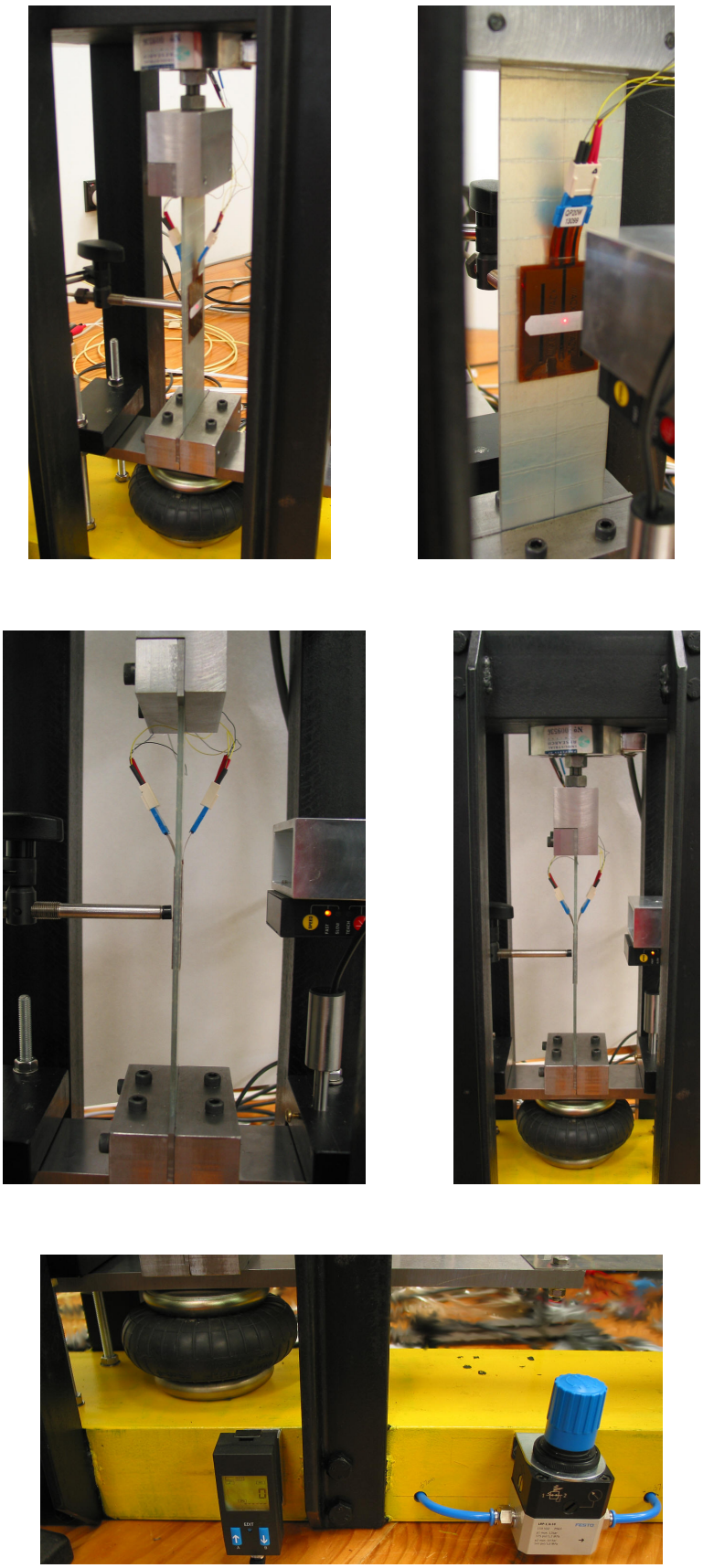

Figure 9.7 Photos of active plate strip in buckling rig during commissioning.

Figure 9.8 Buckling of a laminate plate strip in the test rig during initial experiments.

9.1.3 Loading rig clamp redesign

During initial testing of the plate strip test rig (Figure 9.8) it was found that the buckling behaviour was extremely sensitive to the setup of the two end clamps. Slight torque adjustments on the six bolts in each clamp caused large variations in out-of-plane bending behaviour. This variability is extremely undesirable as buckling experiments are not repeatable and ideal buckling behaviour is difficult to achieve due to the added applied moment. Hence, the top clamp was re-designed to use fewer parts and was machined to a higher tolerance. This change dramatically improved test repeatability, correlation to ideal buckling behaviour, and increased the repeatability. The drawings for the improved clamp can be found in Appendix A.1. Experiments with Plate Strip A used the original clamp, while Plate Strips B and C used the redesigned clamp.

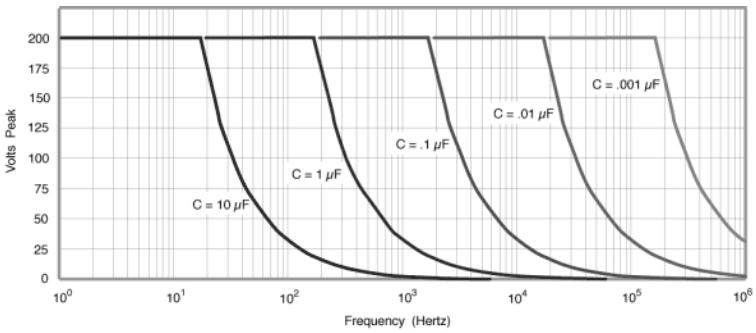

Figure 9.9 Dynamic response of the Piezo Systems EPA-102 amplifier.

9.2 Electronic hardware

9.2.1 Amplifier dynamics

Piezo actuators require driving voltages of up to ±200 volts to generate maximum blocking force. Piezo amplifiers have a maximum slew rate dependent on their peak current capability that, when adjusted for the capacitance of the actuator load, will result in a frequency response that resembles a low pass filter with a finite response time. Figure 9.9 shows the manufacturer supplied frequency response for the Piezo Systems EPA-102 amplifier used in all the experiments.

Testing was performed to confirm the frequency response specification provided by the manufacturer. The amplifier output was connected to the two actuators on Plate Strip B, as this setup provided a representative capacitive load on the amplifier. The Midé ACX QP15W actuators used in Plate Strip B have a combined capacitance of $0.32\mu F$ and a maximum operating voltage of ±100 volts. Figure 9.10 shows the frequency response measured using a white noise source between the amplifier input and high voltage output under load. The amplitude starts to drop off around 300Hz, while the datasheet in Figure 9.9 indicates it should be closer to 1kHz for $0.32\mu F$ at 100 volts. This difference is likely due to additional capacitance in the connections and wiring between the amplifier and actuator.

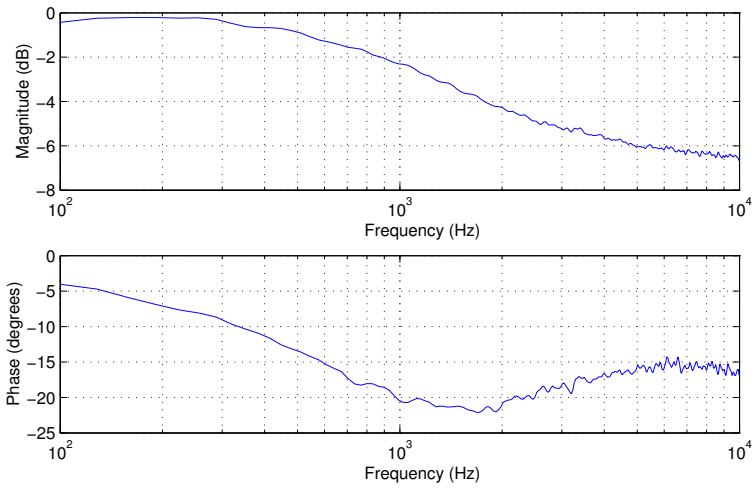

Figure 9.10 Measured frequency response of Piezo Systems EPA-102 amplifier.

9.2.2 Control hardware

A Sheldon Instruments® SI-C33DSP-PCI PC based digital signal processor (DSP) was used for signal processing, control implementation and data acquisition. The DSP card, programmed using Labview®, accommodates up to 64 input and 4 output channels, scanning 1-16 channels multiplexed at sampling rates of up to 250kHz.

9.3 Commissioning and calibration of test system

The first round of tests with Plate Strip A was used to calibrate the various sensors and actuator outputs, as well as the test rig. Details of the sensors and actuators used, along with operating ranges and calibration factors can be found in Appendix A.2.

9.3.1 Plate strip actuation and deflection sensing

Calibration was performed with the active plate strip unloaded, but clamped in the loading rig. A 100 volts peak to peak sinusoidal signal at 1 Hertz was

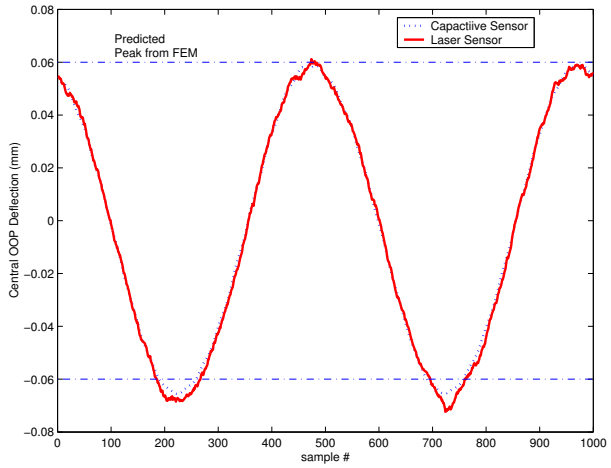

Figure 9.11 Central OOP deflection for a low frequency sinusoidal input of amplitude ±100 volts.

provided to the actuators. Central OOP deflection was measured using both the laser and capacitance distance sensors. A finite element analysis predicts a central OOP deflection amplitude of ±0.06 mm. Figure 9.11 shows the results of this experiment. The central deflection measured by the capacitive and laser sensors are overlaid and seen to have very good correlation with results between -0.07 and $0.06mm$. The maximum difference is seen at the peak, where the laser sensor overshoots by approximately $6\mu m$ (10%). The amplitude of the deflection is also very close to that predicted from the finite element modelling. Allowing for the slight DC offset present in the measured signals the difference in amplitude between the finite element model and capacitive sensor is $2\mu m$ (3.3%). This close agreement between the test and the finite element model verifies the estimated material properties and approximated actuator authority calculations that were made while setting up the finite element model.

9.3.2 Load cell

The load cell was used in conjunction with a Vishay P3500 strain amplifier, which provides both a strain readout and an amplified output signal in the range from

Table 9.5 Calibration of load cell using dead weights.

Weight kg	Load N	Strain Readout $\mu\varepsilon$	Voltage Out mV
0	0	3	0.2
5	49.05	47	12.3
10	98.1	96	24.6
19.1	187.37	186	46.9
28.2	276.64	276	69.2

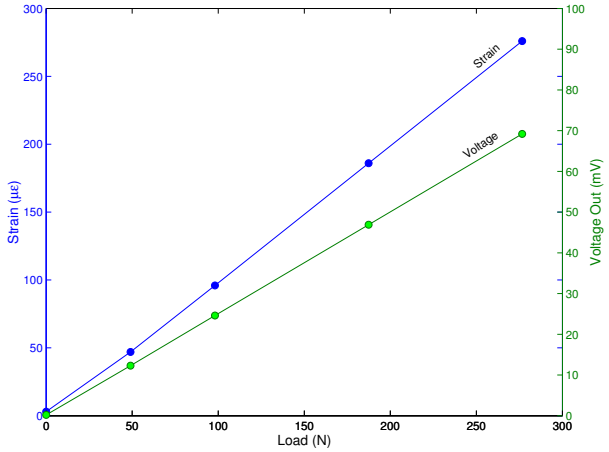

Figure 9.12 Calibration of load cell using dead weights.

0-5 volts. The strain amplifier has both a readout in $\mu\varepsilon$ and an adjustable gain output voltage signal that is proportional to strain. The amplified output gain was set to give a output scale of $4000\frac{N}{volt}$. Calibration was performed by hanging dead weights from the load cell. Due to practical limitations only the lower 5% of the full range of the load cell was calibrated. The gauge factor of the amplifier was set to 1.335 so that $1\mu\varepsilon$ was equivalent to 1N. The measured values from the calibration can be seen in Table 9.5 and Figure 9.12, and are both highly linear.

9.3.3 Pneumatic bellows

The force generated by the bellows is dictated by both air pressure and bellows extension. For this calibration the bellows were extended 77mm, and this exten-

Table 9.6 Load-pressure relationship for pneumatic bellows extended at 77mm.

Load N	Pressure kPa
500	93
1000	177
1250	217
1500	259

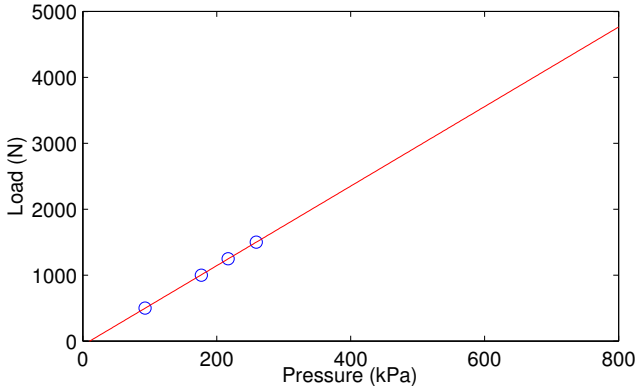

Figure 9.13 Load-pressure relationship for pneumatic bellows extended at 77mm.

sion will change by less than 1mm due to deflection of the plate strip over the course of the tests. Table 9.6 and Figure 9.13 show the results from this test. The relationship is seen to be linear with a slope of approximately $5.88\frac{N}{kPa}$ and zero load offset pressure of 10kPa.

9.3.4 Transport delays

As discussed in Section 7.6.2 the delay in the feedback path is critical to controller performance. Transport delays through components in the feedback path were measured so their effect could be gauged. Table 9.7 lists the measured or manufacturer-specified delays through the main components.

The delay through the DSP processor, including analogue to digital conversions was measured and depends on both the sampling rate (F_S) and level of computation required. Assuming that the algorithm can be fully computed

Table 9.7 Transport delays through hardware in control feedback loop.

Hardware	Delay		Comment
Discrete Filter	$\frac{N \times T_S}{2}$		Approximate delay for a discrete filter with N taps
DSP (I/O + Computation)	$\frac{1}{F_S.\#Channels}$		Minimum delay through DSP card
Piezo Amplifier	140	μs	Step response: -45V to + 45V
	60	μs	Sinusoidal input below 1kHz
Strain Conditioning	35	μs	Rise time (10-90 % full range)
	250	μs	Settling time to 0.1 %
Capacitive Sensor	50	μs	

within one sampling period the maximum delay through the card is $2.T_S$, where T_S is the sampling period. This absolute delay can be kept small relative to the closed loop fundamental frequencies by using high sampling rates and utilising channels near the end of the multiplexer scan list. However, there is still up to two sampling periods between measurement and actuation, which may cause a reduction in peak controllable axial load.

9.4 Digital differentiators and smoothing filters

In order to implement derivative feedback control using displacement sensing it was necessary to design a discrete derivative filter, where the two main parameters that dictate filter performance are the discrete sampling rate and the filter order. Simple derivative filters have frequency responses that resemble a high pass filter and therefore introduce undesired effects such as time delay and high frequency amplification. A comprehensive comparison between various digital derivative filters and design techniques is presented by Chen [31]. Smoothing filters were also designed for the proportional feedback path to reduce electrical noise in the control signal.

To design filters a bandwidth needs to be chosen over which the frequency response is considered important. A bandwidth of 1kHz was chosen as it contained

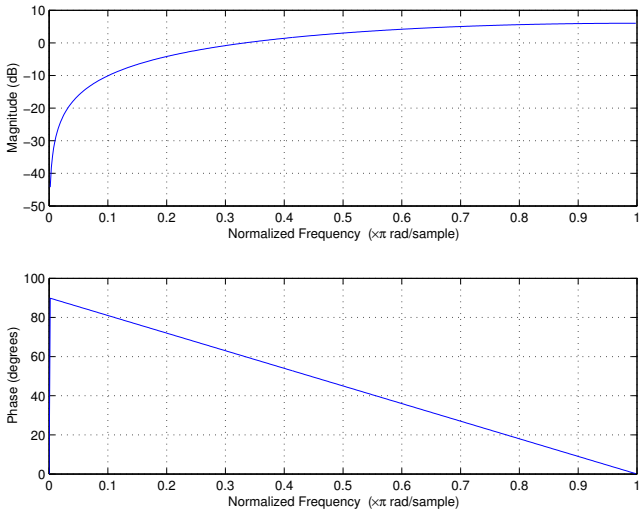

Figure 9.14 Frequency response of a first order FIR direct derivative filter.

the lowest three dynamic vibration modes. For discrete sampling the Nyquist theorem dictates a minimum sampling rate of $2.F_S$, or 2kHz for the chosen bandwidth. This sampling rate was used to design and compare the discrete feedback filters. The coefficients required for implementation of all designed filters can be found in Appendix A.3.

9.4.1 Derivative feedback filtering

Initially, two types of finite impulse response (FIR) derivative filter were modelled. Figure 9.14 shows the frequency response for a simple two point derivative filter. The response of this filter resembles a high pass filter and attenuates frequencies below $0.1 \times F_S$. The phase response for this filter is linear, and the total delay is $\frac{T_S}{2}$, which corresponds to $250\mu s$ with a sampling rate of 2kHz, and the passband spans from approximately 200Hz up to 1kHz. High frequencies are amplified, which resulted in higher mode instabilities excited by high frequency noise in the feedback signal. In addition, low frequencies, as occur when the closed loop system is near buckling, are attenuated.

The second FIR derivative filter was designed with the aim of reducing high

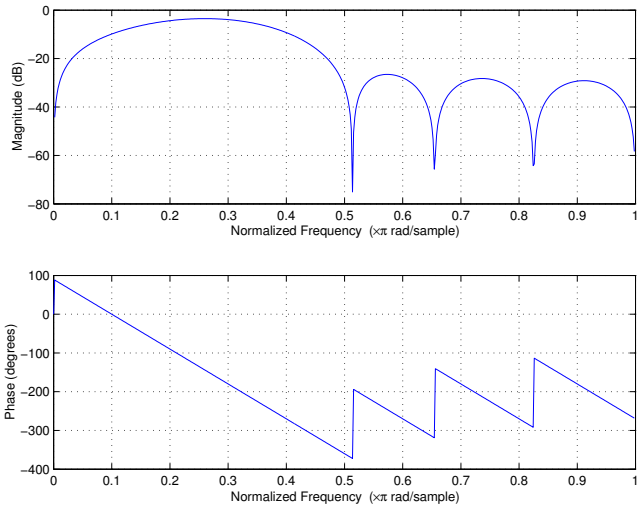

Figure 9.15 Frequency response of a tenth order low pass quadratic FIR digital derivative filter.

frequency amplification through the inclusion of a low pass filter. The design technique makes used of constrained quadratic programming to obtain a best fit to the required response. Figure 9.15 shows the frequency response for a tenth order implementation of this filter. The delay through the filter can be calculated as $\frac{N \times T_S}{2}$, where N is the filter order. Therefore, the delay in the tenth order filter is 10 times that of the simple 2 point filter. Both of these delays are unacceptable at practical sampling rates as the simulations in Section 7.6.2 show a maximum acceptable transport delay of $10\mu s$ before control performance is dramatically reduced.

Due to the unacceptable delay associated with high order FIR filters, infinite impulse response (IIR) filters were designed, which can achieve similar results with a reduced order and hence a lower transport delay. Stability is not guaranteed with IIR filters, and the phase response is nonlinear. The frequency response for a second order IIR derivative filter designed using a combination of Simpson and trapezoidal techniques can be seen in Figure 9.16. The approximate delay through the filter is $\frac{N \times T_S}{2} = 750\mu s$ assuming a sampling rate of 2kHz. This IIR filter is stable and has a wide passband with a reasonably flat magnitude

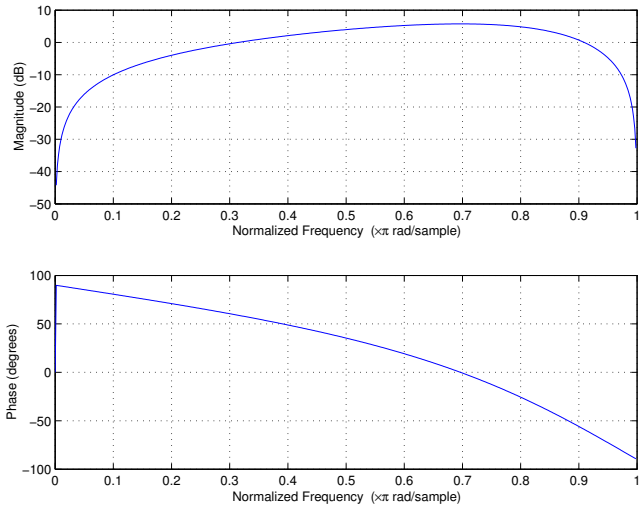

Figure 9.16 Frequency response of a second order inverse Simpson and trapezoidal IIR derivative filter.

response. This filter was determined to be the most suitable for active control as it provided the best magnitude response over the frequency range of interest, although the transport delay is much larger than the $10\mu s$ found to be critical during simulations. Due to the tradeoff between sampling rate and delay, this system can either achieve the desired delay or desired passband frequency, but not both.

9.4.2 Proportional feedback filtering

Two smoothing filters were designed and considered for use in the proportional feedback path. Figure 9.17 shows the frequency response for a ninth order FIR moving average filter. This is a simple and commonly used filter that is used to tradeoff noise against bandwidth. For a sampling rate of 2kHz this filter would reduce the bandwidth to approximately 150Hz and add a time delay of 2.25ms, which is unacceptably high.

Figure 9.18 shows the frequency response for an alternative IIR low pass smoothing filter. The goal of this design was to create a low pass filter with a

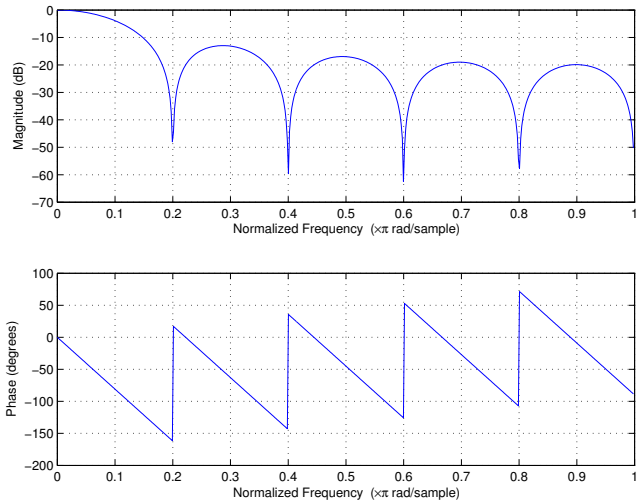

Figure 9.17 Frequency response of a ninth order FIR moving average smoothing filter.

similar phase response, and hence delay, to the second order IIR derivative filter employed. By matching phases between the two filters the proportional and derivative signal paths will remain ninety degrees out-of-phase for the frequency range of interest, which is important for controller stability. This Butterworth IIR filter was designed using the filter design toolbox in Matlab®. The transport delay associated with this filter is $750\mu s$ and the passband is approximately 0 to 800Hz.

The two IIR filters designed for the derivative and proportional feedback paths were implemented in the active controller. Another difficulty that arose during the design of filters for this application was the variation of vibration frequencies due to compressive loading of the plate strip. Under compression the plate strip fundamental frequency will reduce from approximately 270Hz to below 100Hz, and then ultimately to 0Hz when the critical load is reached. Hence, it is very important to keep the lower passband limit as low as possible.

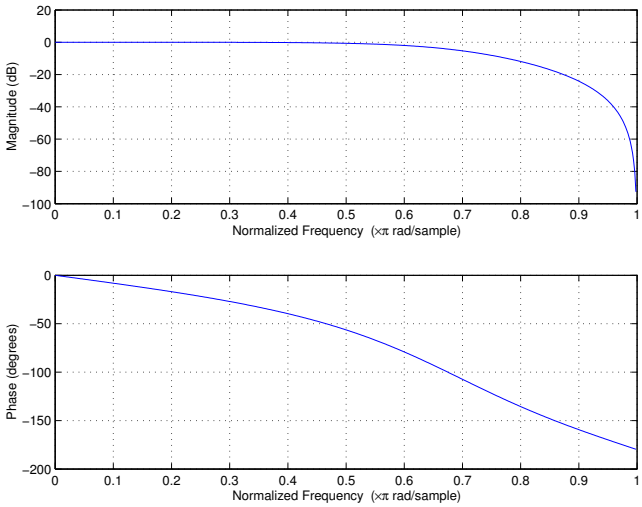

Figure 9.18 Frequency response of a second order low pass Butterworth IIR smoothing filter.

Chapter 10

Laminated plate strip experiments

10.1 Experimental method

The plate strips were loaded in compression using the purpose built test rig described in Section 9.1.2. Sensor details, including calibration constants, operating ranges and power supply requirements are listed in Appendix A.2. Figure 10.1 shows the pneumatic control valve and readout. Table 10.1 lists the available software routines written for Labview® 5.1 and application notes. Both controlled and uncontrolled cases were performed using the following test procedure:

1. Turn on power supplies and signal conditioning equipment. Strain gauge and load cell circuits require time to warm up.

2. Ensure the pneumatic precision regulator is fully open (zero outlet pressure). Open the bottle and line valve, then set both the bottle and line regulators to approximately 6 bar.

3. Balance strain gauge and load cell circuits to give zero output. Strain gauges are balanced by adjusting the potentiometer on the front of the signal conditioning enclosure, and the load cell by adjusting the balance control on the P3500 conditioner.

4. With the computer running load the appropriate Labview® acquisition and

control routine. Before running the routine set static parameters such as sampling rate, filename for data storage, and digital filter definitions.

5. Start the routine. After ensuring the sensors are near the center of their range, set the software offsets to reflect the current zero position and start streaming acquired data to disk.

6. Using the precision regulator shown in Figure 10.1 slowly load the plate strip, while paying attention to the load and plate strip central deflection. A rate up to 50N per second is suitable up to around 1.5kN. Above this load the pressure (load) should be increased slowly while keeping an eye on the out of plane deflection / bending strain to ensure the load is not set well past P_{CR} to protect the laminate.

7. If the system is running closed-loop, it is important to be able to quickly reach the piezo amplifier power switch in case the system becomes unstable.

8. Load the plate strip to the point where buckling occurs, although it is recommended not to exceed a central out-of-plane deflection of 1mm. This limit will ensure that the specimen is not permanently damaged. Unload the plate strip slowly, noting how close zero load deflections reflect those prior to loading.

Table 10.1 Application notes for available control routines.

Filename	Application
Strip_ControlRoutine_FIR_DispBased.vi	Capacitive displacement based control using FIR filters on input signals.
Strip_ControlRoutine_FIR_StrainBased.vi	Bending strain based control using FIR filters on input signals.
Strip_ControlRoutine_IIR_DispBased.vi	Bending strain based control using IIR filters on input signals.
Strip_IIR_FreqRespCompensator_DispBased.vi	Capacitive displacement based control using an IIR compensator based on system frequency response.

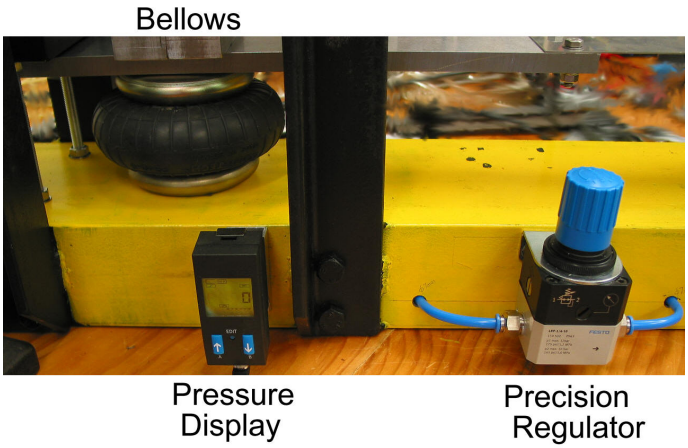

Figure 10.1 Pneumatic loading system and controls.

10.2 Experimental results

For analysis and comparison of experimental results between various strips and configurations a standard gauge of buckling was defined. During calibration of Strip A (Section 9.3.1) it was found that the maximum central deflection that could be induced by a pair of embedded QP10W actuators was $\pm 125 \mu m$, which is approximately 4% of the laminate strip thickness. When deflections are greater than this limit the actuators no longer possess the authority to correct the bending and the strip will buckle. This standard limit was used for all experiments to determine the point of buckling.

10.2.1 Plate Strip A

Substantial effort was required to create the fixed boundary conditions using the original design clamps. There were six bolts in each clamp, which allowed freedom to slide the clamp by several millimeters. This freedom resulted in low repeatability, especially if the clamp was loosened and the plate strip adjusted or reinstalled between runs.

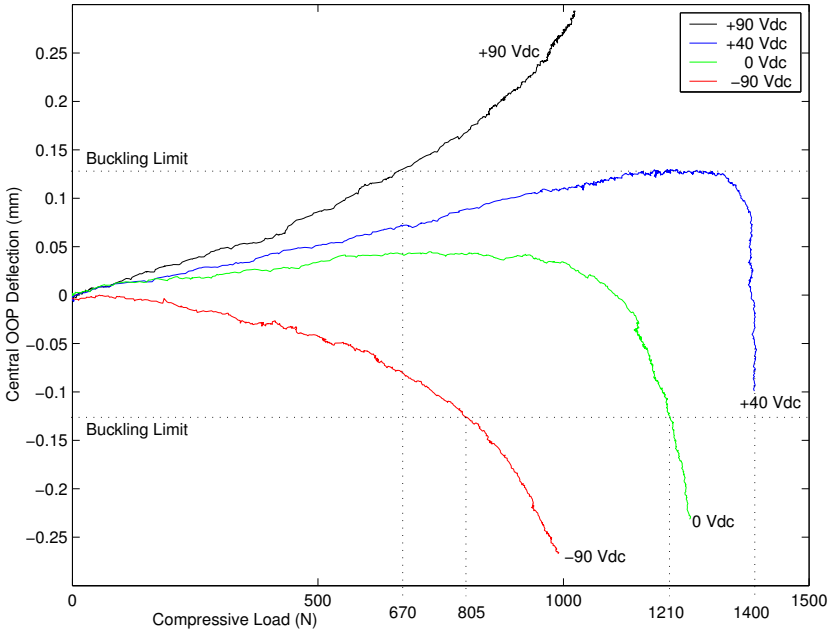

Figure 10.2 Plate Strip A: Central deflection under compressive loading with constant control offset.

Ideal buckling load-deflection curves display very little out-of-plane deflection until the buckling load is reached, where it turns almost vertical before failing. The initial results from Plate Strip A shown in Figure 10.2, for the case with 0Vdc offset, displayed appreciable out-of-plane deflections from the beginning of loading, culminating in premature buckling at 1210N, where the expected load from nonlinear finite element analysis was 1855N. This behaviour is the result of initial curvature in the plate strip. A constant correcting moment from the actuators can correct for initial curvature, providing the magnitude is within the actuator authority range and the deformed shape is compatible with the actuator configuration. The experiment was repeated with various values of constant actuator offset, until the value was found where the resulting curve resembled that of ideal buckling.

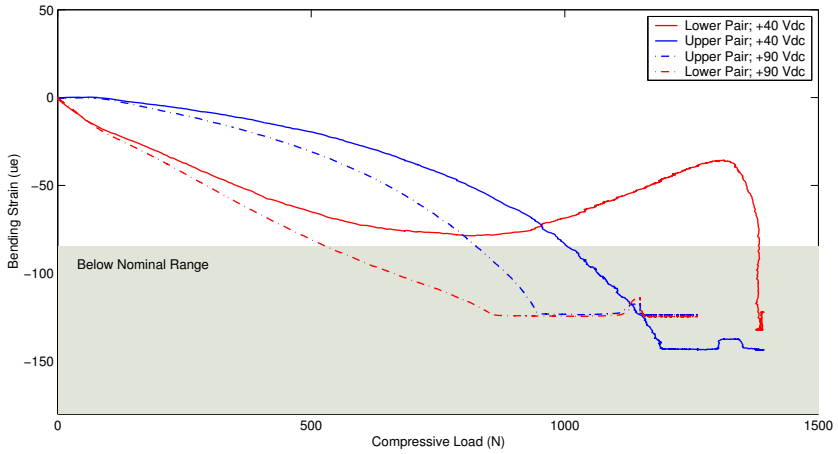

Figure 10.3 Plate Strip A: Measured bending strain under compressive loading with constant control offset of 40Vdc.

Figure 10.2 also shows the effect of different constant bending moments on the buckling behaviour of plate strip A. A constant offset of 40 volts (20% of full range) resulted in a load-deflection curve that resembled that of ideal buckling. The central deflection along this curve is seen to gradually deflect in the positive direction while the load is ramped up, followed by sudden buckling in the negative direction. It is not apparent from this plot alone why the direction of OOP deflection changes at a certain point. One explanation for this could be unaligned loading, which initially pushes the plate strip in one direction, until the plate strip preferential buckling direction takes over at higher loads pushing in the opposite direction.

Bending strain was calculated by finding the difference between strain gauges on opposite surfaces of the laminate. One pair of gauges was bonded to each end of the plate strip so that both an upper and lower end bending strain could be calculated. The upper end bending strain refers to the end closest to the load cell, while the lower end is near the bellows.

Bending strain plots can be seen in Figure 10.3. These plots show the limited nominal range over which the measured strain is known to be linear. The dynamic range of the strain measurements was limited by the high gauge factor, and signal

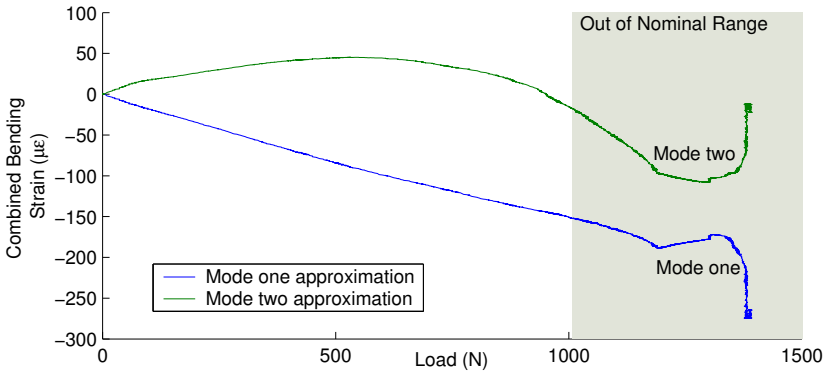

Figure 10.4 Plate Strip A: Approximation of modal amplitudes through combination of upper and lower bending strains. Constant control offset of 40VDC. Nominal range dictated by point where first pair of gauges becomes out of range in Figure 10.3.

conditioning electronics. Overall, these strain gauges were too sensitive for this application; a gauge factor between 10 to 40 would be more suitable.

There is considerable variation between the upper and lower bending strains in Figure 10.3. This variation is probably due to the plate strip deforming in a combination of the first two buckling mode shapes due to the random initial curvature and nonuniform loading. For the first mode, the bending strains would be of equal magnitude and sign, whereas in the second mode the two strains would be of opposite sign. Figure 10.4 displays an approximation of the modal amplitudes for the first and second modes based on the sum and difference of the measured lower and upper bending strains. Mode one shows an almost linear increase from zero load, while mode two initially deflects in one direction before changing direction and deflecting in the opposite direction. Although Figure 10.4 only contains plots for the experiments with a 40Vdc offset, the pattern is similar for other offset voltages.

Figure 10.5 displays a comparison of the experimental results for Plate Strip A to those found in linear and nonlinear finite element analysis. The initial perturbation for the nonlinear analysis was approximately $1\mu m$. Plate Strip A, with no curvature correction applied, buckled at 65% of the load predicted by

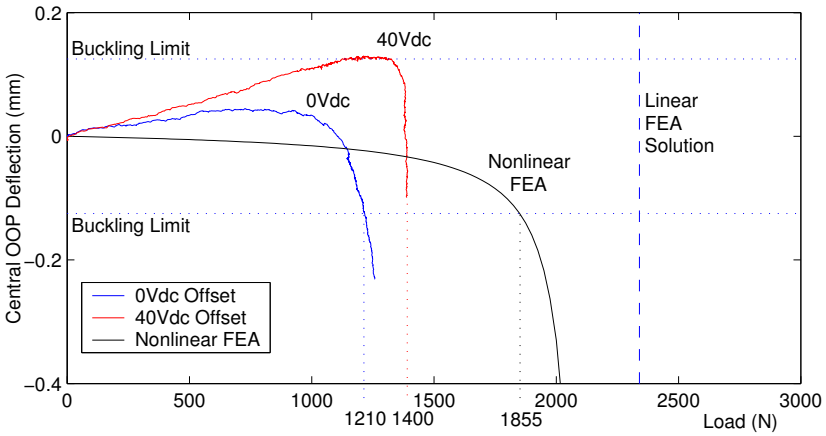

Figure 10.5 Plate Strip A: Comparison to finite element solutions for plate strip model.

the nonlinear model, and 52% of the linear eigenvalue solution. In attempting to correct for the initial curvature the buckling load was increased to 75% of the nonlinear model. The curvature correction was not fully successful due to either the initial curvature not being of a mode one shape, as the actuators can only actuate into a mode one shape, or because the assumed model was too conservative.

The buckling behaviour of Plate Strip A was significantly different from simulations, and displayed little repeatability. It was concluded that one or more of the operations performed to embed the actuators either released residual stress from the laminate manufacture, or accentuated an unsymmetrical layup. Combined with the difficulty encountered setting up the correct boundary conditions with the clamps, this situation resulted in behaviour that was unpredictable and therefore uncontrollable. For this reason it was decided not to embed the actuators on subsequent plate strips, and to redesign the clamping method. An increase in buckling load of 16% was achieved in Plate Strip A, from the correction of initial curvature using a constant actuator offset.

The high gauge factor silicon strain gauges used in Plate Strip A, were too sensitive, resulting in an small operating range of approximately $\pm 80 \mu\varepsilon$. No

gauges were available with an intermediate gauge factor between conventional metal foil gauges that have a gauge factor of around 2 and silicon gauges that have a gauge factor of over 100.

10.2.2 Plate Strip B

Prior to testing of Plate Strip B the upper loading rig clamp was redesigned. Reducing the number of parts and bolted joints made a substantial improvement to the repeatability and the resulting behaviour better resembled a buckling case.

The increase in plate strip flexural stiffness from the addition of unpowered actuators on the surface can be seen by comparing the blank plate strip test to Plate Strip B with no voltage offset. Figure 10.6 shows the buckling load increase from 1465N to 1720N, which is purely from the additional stiffness of the unpowered actuators in the central region of the plate strip. This additional stiffness is not represented in the finite element model and therefore simulation results shown in Figure 10.6 are estimated to be approximately 250N lower than if the additional stiffness was taken into account. The case, where Plate Strip B has no voltage offset, displays relatively good agreement with the nonlinear finite element solution. These results can also be compared to Plate Strip A (Figure 10.5), which used the old upper clamp and had actuators embedded into the laminate. The buckling load from the best curvature correction attempt on Plate Strip A was 1400N.

For Plate Strip B, the best constant offset to correct for initial curvature was found empirically to be 78 volts (78% of full range). This result increases the buckling load from 1720N to 2265N as seen in Figure 10.6. This load is higher than the results of the nonlinear FEA, but the additional stiffness from having the actuators bonded to the surface was not included in the nonlinear model. This buckling load is also approaching the linear eigenvalue solution of 2340N.

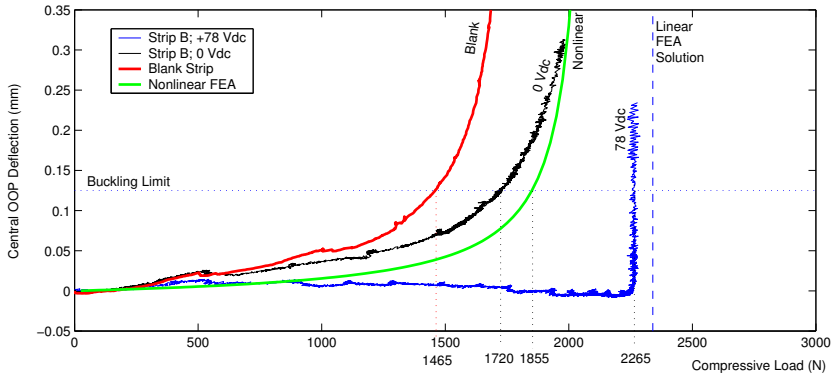

Figure 10.6 Plate Strip B: Central deflection under compressive loading with constant control offset.

The buckling curve for a 78 volt offset is very close to an ideal buckling case and out-of-plane deflection in this case was within $10\mu m$ (0.3% of laminate thickness) until buckling initiated. In addition, this deflection curve in Figure 10.6 is also very close to ideal.

Figure 10.7 shows the measured bending strains for constant curvature correction of Plate Strip B. This plot shows that in both cases the deflection is a combination of modes one and two. The reason for this multi-mode response could be misalignments in the loading rig as shown schematically in Figure 10.8. Part of that misalignment could be due to nonuniform contact between the end plate strip face and the clamp, causing an offset in load transmission, and a second part of it from imperfections in the plate strip. This second mode deflection is subsequently triggering premature mode one buckling as it cannot be controlled with this actuator configuration. As control is only implemented on the first mode, there is nothing that could be done to correct for the second mode deflection.

One major concern with Plate Strip B was that by requiring a constant voltage offset of 78% of actuator authority to correct for initial curvature, only 22% remains for active buckling control. The effect that this reduction in actuator authority would have on controller performance was simulated in Section 8.5.2.

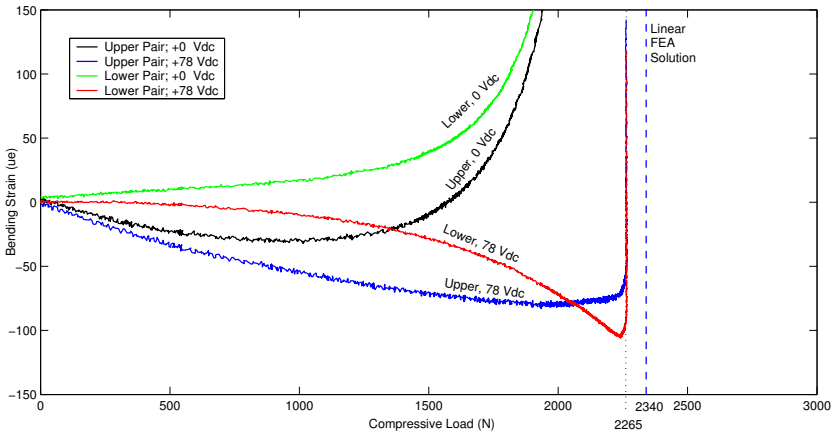

Figure 10.7 Plate Strip B: Measured bending strain under compressive loading with constant control offset.

Figure 10.8 Schematic of misaligned loading causing a second buckling mode deflection.

Closed-loop performance was reduced from a load ratio of 1.62 to 1.28. Keeping this result in mind, the next step was to attempt active buckling control while maintaining the 78 volt curvature correction offset.

The error signal used in the control loop was the average strain signal from the upper and lower gauge pairs. The set point (desired equilibrium position) for control was set at the deflection seen at a load of 2kN (85% of P_{CR}). Initially the optimised control gains (Section 8.4) were trialled. The result was an unstable closed loop system, at zero or any compressive load on the plate strip. When turned on, the feedback loop would oscillate at the fundamental dynamic frequency with an exponentially increasing amplitude. It was found that if the control gains were uniformly lowered, the instability would no longer occur. Various sampling rates and filtering schemes were tried, but the optimal gains did not prove feasible. The reason for this was that possibly the plate strip has been assumed to display Bernoulli-Euler column behaviour when in reality it closer mimics plate bending behaviour. Another possible factor in this instability was a larger than predicted transport delay through the system. The characteristics of the piezo amplifier and signal conditioning amplifiers were not incorporated into simulations, which would account for the underestimation of delay in the model. Other differences between the simulations and experiments include the nonlinear plate strip behaviour, additional stiffness due to actuators mounted on the surface and the limited bandwidth of the controller. Control gains were thereafter found empirically, by finding the control gain stability limit at no load, and using a gain 25% lower than the limit.

Figure 10.9 shows the result of an attempt to actively control buckling using a PD control routine. Empirically determined control gains are given in Table 10.2. The control loop was operating at 100Hz and using 52 point FIR filters for averaging and derivative calculations. This configuration has a very low band-

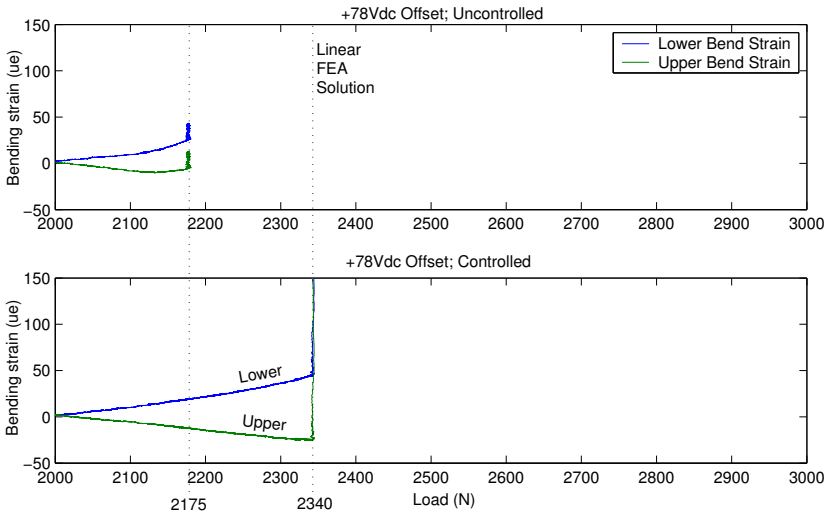

Figure 10.9 Plate Strip B: Results of strain based feedback control.

width of only a few Hertz and therefore will not interact with the dynamics of the plate strip. This low bandwidth controller was found to be more stable than a high bandwidth controller, but will not achieve the designed controlled buckling load due to its inability to control the fundamental vibration modes of the plate strip. The active control has succeeded in increasing the buckling load from around 2175N to 2340N (7.6%). The limited control authority, due to 78 volt offset, would have limited this result.

Table 10.2 Empirically found control gains for Plate Strip B.

G_1 (Proportional)	$0.06V/\mu\varepsilon$
G_2 (Derivative)	$0.02V/\mu\varepsilon$

In Figure 10.7 the 78 volt offset case buckles at 2265N while for the equivalent test case (offset but uncontrolled) in Figure 10.9 the critical load is 2175N. These two tests are equivalent but performed at different times, which shows the level of repeatability that is achievable. After a run where buckling occurs and the plate strip deflects substantially, a semi-permanent deflection remains when unloaded which may disappear very slowly. This has a substantial effect on the

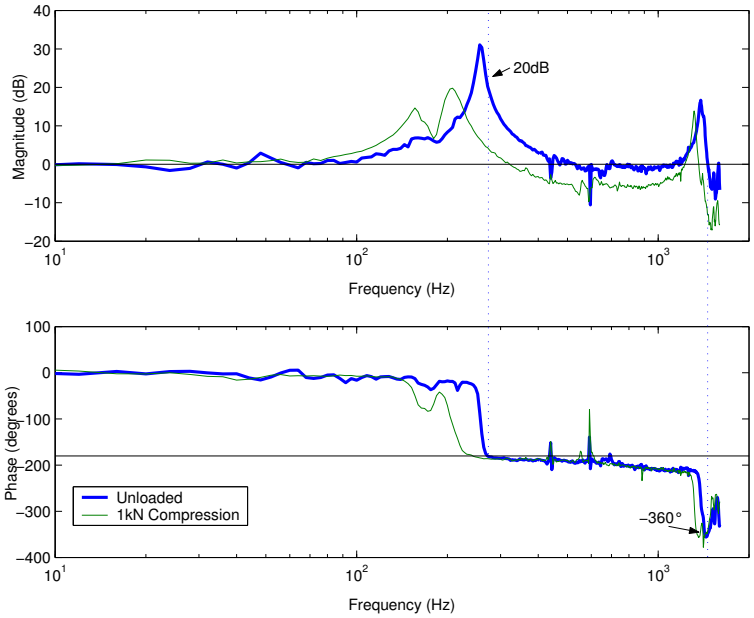

Figure 10.10 Frequency response of Plate Strip B from piezo amplifier input to conditioned bending strain output.

repeatability between tests.

Figure 10.10 shows the frequency response measured between the piezo amplifier input and the combined output from the conventional metal foil strain gauges. The plot is averaged over 50 periods, and the coherence is quite low, which indicates a low signal-to-noise ratio (SNR). Considering the unloaded case, the fundamental vibration mode can be seen at 255Hz, and a higher mode at 1380Hz. Compared to the results from the finite element analysis given in Table 8.6 this measured frequency lies between the fourth and fifth eigenmodes. Not all structural modes are seen in the frequency response plot as only those that are observable by the chosen sensor configuration are measured. Two plots are shown in the figure; one for the unloaded case and the second for a substantial compressive load of 1kN, which is approximately 43% of Pcr. This figure shows the reduction in dynamic frequencies and other small changes to the frequency response due to the application of compressive loading. For buckling control the system will need to remain stable at loads up to and beyond Pcr. The phase

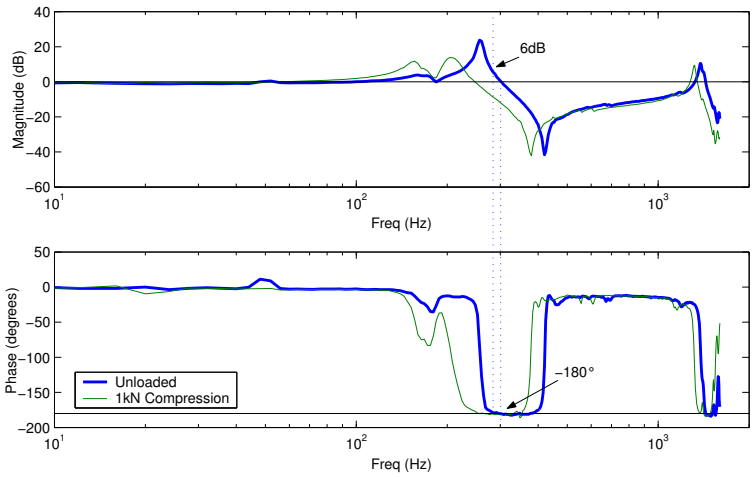

Figure 10.11 Frequency response of Plate Strip B from piezo amplifier input to the amplified output from the capacitive central OOP deflection sensor.

and gain margins for the unloaded case are approximately $-180°$ and -20dB, which indicates an unstable closed-loop system. There are several reasons why the system could be unstable. Gain and phase margin analysis is based on a linear system where the experimental setup could be nonlinear. Also, unmodelled transport delay through the piezo amplifier could add to the reduce the phase margin, resulting in stability concerns.

Figure 10.11 shows the frequency response between the input to the piezo amplifier and the output from the capacitive distance sensor, which is located at the center of the plate strip. The coherence of the averaged response data, and therefore the SNR, is much higher than it was for the conventional strain gauges. The first mode in this plot looks very similar to that of Figure 10.10 for the unloaded case. The antinode seen at approximately 430Hz is the second dynamic mode of the plate strip. This second mode is torsional and has no OOP deflection at the center of the plate strip. This inability to measure the torsional mode results in an antinode in the frequency response. The phase and gain margins for the unloaded case in Figure 10.11 are $0°$ and -6dB. The system is strictly unstable, but margins have improved when compared to the case where

the strain gauges were used for feedback.

10.2.3 Plate Strip C

Plate Strip C was designed to have substantially greater control authority than Plate Strip B. Each actuator used consisted of two PZT wafers, each of which had the same authority as the QP15W used with Plate Strip B. The two wafers are superimposed and encased in a single device as seen in the schematic in Figure 8.7. The two wafers can be driven independently if desired, which would allow the use of one pair of wafers to provide a constant curvature correction offset and the second pair to be used for active control. It was decided for this experiment that the two pairs of wafers would be wired together and run from a single channel. If wired separately, the wafer performing only curvature correction would not be utilising its entire authority, which is considered wasteful. The benefit of separate wiring is that the only capacitance of one wafer is loading the dynamic control channel. A lower capacitance load on the piezo amplifier will result in a better response at high frequencies and reduce delay. This increase in control authority will result in an increase in the control ratio. The resolution of the capacitive sensor was $5\mu m$ and the dual wafer actuators provided a maximum central deflection of approximately $100\mu m$, therefore, the control ratio was 20.

Figure 10.12 shows the results of correction of initial curvature. As intended, these more powerful actuators resulted in a lower percentage of control authority being required for curvature correction. Only 41 volts (20.5% of full range) was needed to achieve good buckling behaviour. Due to the increased thickness of these actuators bonded to the surface of the plate strip, the flexural stiffness was again increased. This can be seen in the test with no offset correction where Plate Strip C buckles at 2100N, compared to 1720N for Plate Strip B. Also, Plate Strip C due to its increased stiffness, now buckles at a higher load than the nonlinear

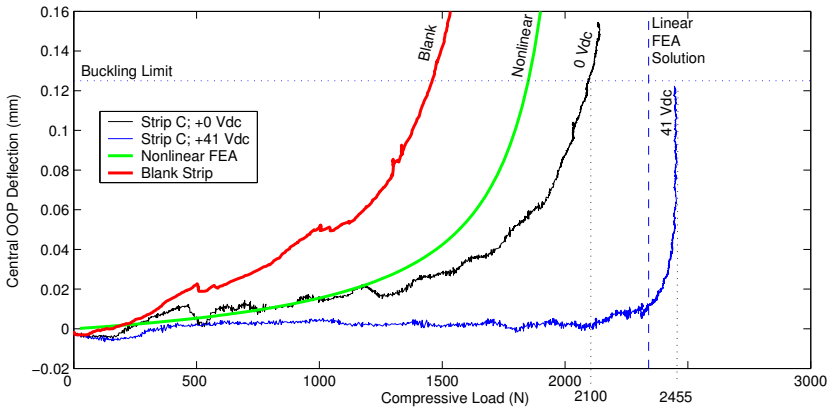

Figure 10.12 Plate Strip C: Central deflection under compressive loading with constant control offset.

FEA results. For Plate Strip C the buckling load is 2455N with a 41 volt offset to correct initial curvature.

Active control was attempted on Plate Strip C superimposed on the 41 volt offset. Figure 10.13 shows the results of several control trials where the control gains were again found empirically and are given in Table 10.3. In the first test the controller is purely proportional and the feedback loop operated at 100Hz. For this low bandwidth controller the result was an increase from 2455N to 2610N (6%). The second active control test operated at a much higher bandwidth given a sampling rate of 10 kHz. This controller incorporated derivative as well as proportional control, enabling it to remain stable with a proportional control gain that was 40% higher than in the low bandwidth controller. The closed-loop buckling load was 2880N, which is a 17% increase on the curvature corrected but uncontrolled case, and a 37% increase over the uncorrected case.

Table 10.3 Empirically found control gains for Plate Strip C.

Low bandwidth controller	G_1 (Proportional)	$25V/mm$
High bandwidth controller	G_1 (Proportional)	$35V/mm$
	G_2 (Derivative)	$30V/(mm.s)$

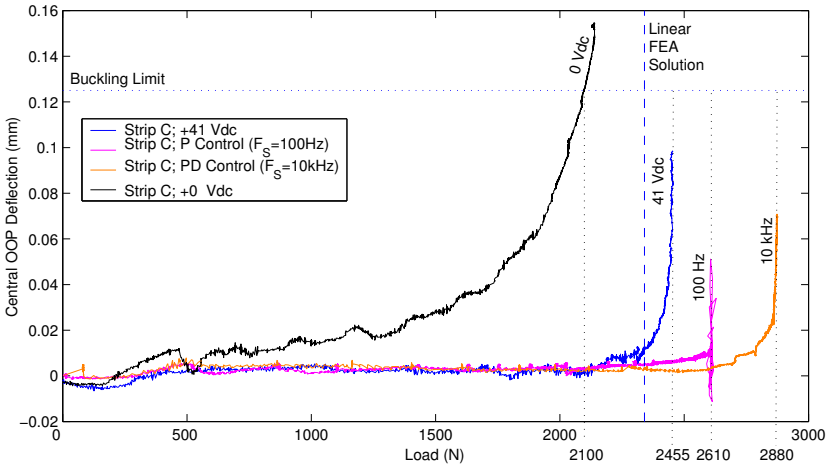

Figure 10.13 Strip C: Results of central deflection based feedback control.

Figure 10.14 shows the controller output for the high bandwidth controller. The range of this output signal is $\pm 10 Vdc$, prior to going through the PZT amplifier, which has a gain of 20. The level of noise in the feedback loop can be seen in this plot. The approximately 20mV of electrical noise in the capacitive sensor, is amplified through feedback and becomes the equivalent of $7.5 \mu m$ of uncertainty in out-of-plane deflection, reducing the ability to control the plate strip at higher loads.

Figure 10.15 shows the frequency response for Plate Strip C, unloaded, between the piezo amplifier input and the central OOP deflection sensor output. The plot is very similar to that from Plate Strip B, although the first mode has slightly lower frequency of 225Hz, compared to 255Hz for Plate Strip B. The phase and gain margins are 0° and -10dB respectively indicating an unstable closed-loop system. Stable control was only achieved as the feedback gains were reduced to below the magnitude required for unity feedback.

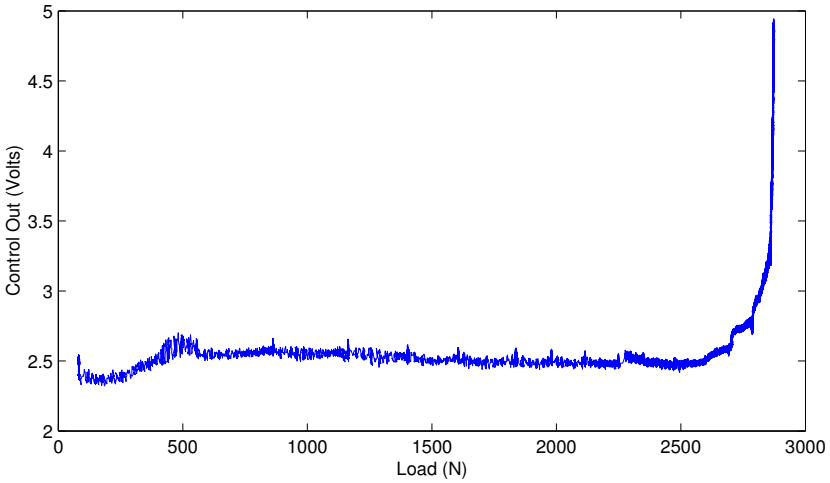

Figure 10.14 Strip C: Control output signal for high bandwidth controller where 10 volts represents full actuator authority.

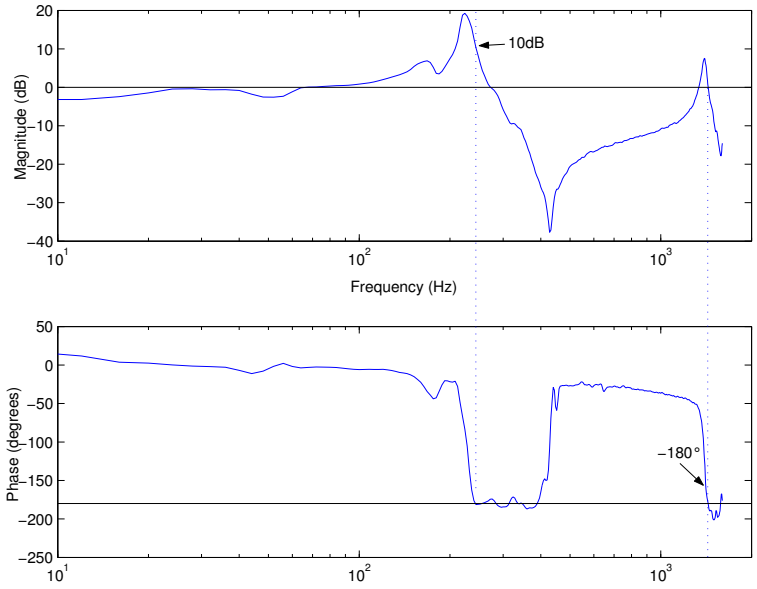

Figure 10.15 Unloaded frequency response of Plate Strip C from piezo amplifier input to capacitive central OOP deflection sensor output.

10.3 Feedback lag and damping effects

Experimental results have shown that active buckling control is extremely sensitive to transport delays or phase lag through the feedback path. This sensitivity results from a combination of the nature of the structure and limited actuator authority, especially when the load is above the critical buckling load. If there is too much delay then by the time the sensed information results in a corrective moment the structure has already moved away from that state, and perhaps beyond the range in which the actuator authority is able to bring the structure back to equilibrium.

The dynamics of the structure play a large part in defining the critical delay. As the plate strips used in this research were approximately 30 times stiffer than any other published experiments [9, 15], their dynamics are substantially faster. Active buckling control has not been attempted on structures of this stiffness before, so difficulties keeping this delay within critical limits have probably not been encountered before, as it has not been reported in the literature. Considering that this glass-polyester laminate fits into the flexible end of the spectrum for fibre-reinforced composites and that joints are usually closer to clamped than pinned, any practical application will have at least this stiffness.

During the simulation of the active plate in Chapter 7 and the design of the experiment in Chapter 9, manufacturer specified values for delay were used for hardware such as the PZT and strain gauge amplifiers. When measured, these delays were found to be considerably larger than specified, therefore violating critical limits found during simulations. Amplifiers also displayed a non-uniform delay over the operating frequency range, and therefore a frequency response function would be more accurate than a pure delay for simulation. Another contributing factor to the increase between assumed and actual delays was the discrete filtering required on feedback signals. To keep noise to an acceptable

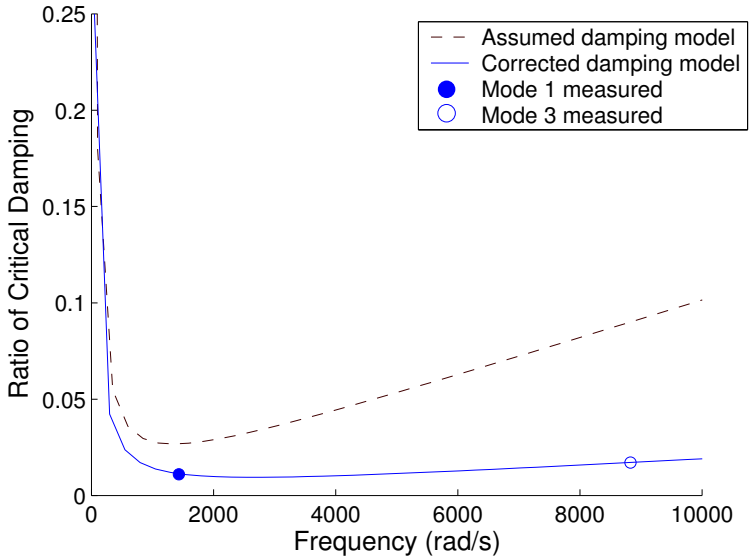

Figure 10.16 Updated damping model based on measured damping of Plate Strip C.

limit, 10 point filters were used to evaluate and smooth the derivative and proportional and signals, while 2 point filters were used during simulation.

The critical delay for the fully constrained plate was found in Section 7.6.2 to be $10\mu s$, and it is clear that this limit was exceeded during experiments. The delay through the PZT amplifier was measured at approximately $60\mu s$ up to 1kHz and the discrete filtering operation delayed the signal approximately $150\mu s$ if sampled at 10kHz (Section 9.4). The DSP based control implementation also contributed substantial delay as it was found that the output of the calculated actuator drive signal based on a discrete measurement did not take place until the subsequent sample period. For a sampling rate of 10kHz this transport delay could be as large as $200\mu s$ (Section 9.3.4).

The structural damping of Plate Strip C was measured during experiments and found to be 1.1% of critical at the fundamental vibration mode of 228Hz and 1.7% at 1405Hz. As these values are considerably lower than original estimates used for simulations shown in Figure 10.16, and due to damping slowing the response of a structure, this overestimation caused simulations to have a larger delay tolerance than the experimental structure.

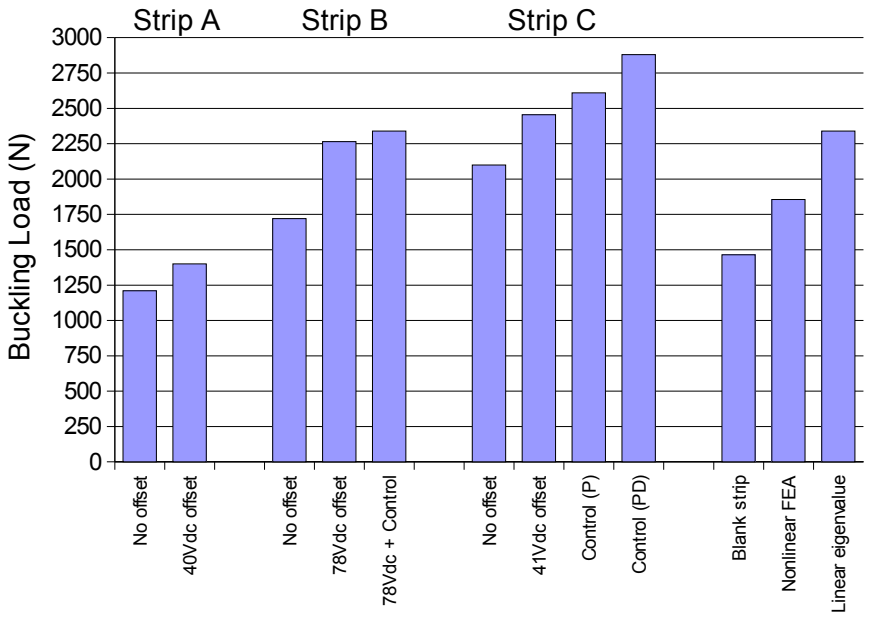

Figure 10.17 Comparison of buckling loads for finite element results, blank and active plate strips.

10.4 Summary of experimental results

Figure 10.17 charts and Table 10.4 lists the measured buckling loads of the three active plate strips both controlled and uncontrolled, the finite element results and blank plate strip test result. Plate Strip A is seen to have the lowest loads, which are substantially lower than predicted by the finite element analysis. It was concluded that machining operations involved in embedding the actuators, combined with loading rig misalignments caused premature buckling in this specimen.

Plate Strip B was successful in achieving buckling loads very close to both the linear and nonlinear finite element critical loads. The constant voltage applied to correct for initial curvature made a substantial improvement to the buckling behaviour of the plate strip, which resembled that of ideal buckling of a straight member. Active buckling control on Plate Strip B was partially successful, but limited by the reduced actuator authority remaining after curvature correction was applied.

Table 10.4 Buckling loads for finite element results, blank and active plate strips.

Description	Offset Vdc	Control	Buckling Load N
Strip A	-	-	1210
Strip A	40	-	1400
Strip B	-	-	1720
Strip B	78	-	2265
Strip B	78	PD: 100Hz	2340
Strip C	0	-	2100
Strip C	41	-	2455
Strip C	41	P: 100Hz	2610
Strip C	41	PD: 10kHz	2880
Blank strip	-	-	1465
Nonlinear FEA	-	-	1855
Linear eigenvalue	-	-	2340

The highest buckling loads were seen in Plate Strip C. Consideration needs to be given to the stiffness that would have been added to the central region of the plate strip due to the relatively thick and stiff piezo actuators bonded to the laminate surface. A low bandwidth proportional controller and a high bandwidth proportional-derivative controller were tested and the latter increased the buckling load by 37% compared to the plate strip without initial curvature correction, and 17% compared to the case with curvature correction applied.

Figure 10.18 shows three frequency response plots for unloaded plate strips between the actuator input and the sensor output. Two plots were determined experimentally for Plate Strips B and C, and the third was simulated using Matlab®. Table 10.5 lists the frequencies and magnitudes of the three modes as seen in Figure 10.18. Mode 1 has good correlation between both the plate strips, and the simulation. For the second mode, Plate Strips B and C are very similar, but the frequency for the simulation is substantially higher than the measured values. One possible reason for this variation is the added stiffness to the central region of the plate strip from bonding actuators to the laminate surface. This mode also has more damping in the simulated model, which can be esti-

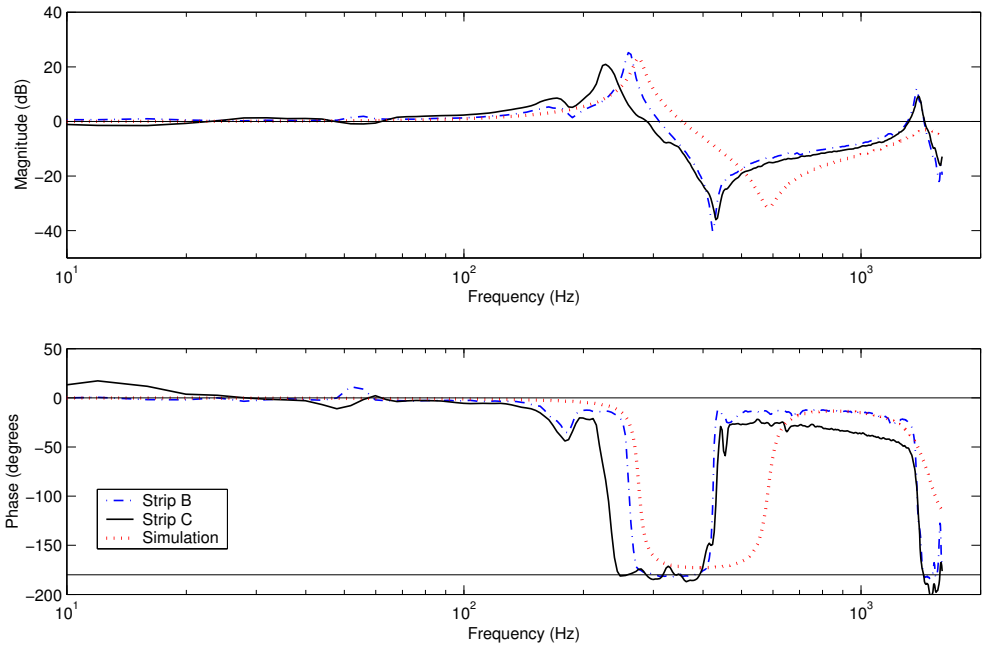

Figure 10.18 Comparison of unloaded frequency response for Plate Strips B and C, and simulation.

mated by the width of the mode peak. The finite element model uses Rayleigh proportional damping, where damping increases with frequency as shown in Figure 5.1. The difference in damping between simulation and experimental results for mode 3 is even more pronounced. It is concluded that damping was overestimated in the finite element model. This is confirmed by the measurements shown in Figure 10.16. One other important difference that exists between the simulation and experimental frequency responses is the phase between modes 1 and 2. The phase margin is 10° in the simulated response, compared to 0° for the experimental cases. Based on the phase and gain margins the simulated system is stable, while the experimental system is marginally unstable.

The transport delay or lag in the feedback loop, which was estimated to be up to an order of magnitude larger in the experiment than the critical delay limit established from simulation-based studies. The consequence of this discrepancy would be a loss of stability margin for the controller, which is consistent with what was observed in these experiments.

Table 10.5 Comparison of frequency and magnitude of modes from frequency response analysis

		Mode 1	Mode 2	Mode 3
Frequency (Hz)	Strip B	255	420	1380
	Strip C	225	430	1400
	Simulation	275	585	1470
Magnitude (dB)	Strip B	24	-42	11
	Strip C	19	-38	8
	Simulation	24	-31	-2

Chapter 11

Conclusions

The results show that for the laminate plate of dimensions 300 by 200 by 3mm that was designed, active control can increase the buckling load to 2.3 times P_{CR}. Through optimisation of plate variables this control was achieved using only four pairs of actuators, which cover 8% of the plate surface and actuate the first two buckling modes. The performance of this controller has been confirmed in numerous simulations, considering the effects of noise, actuator authority, and sampling rate. The result of these simulations was that the active buckling controller required a minimum sampling rate of 10kHz, equivalent noise lower than $12\mu\varepsilon$ or $11\mu m$ of center deflection and a total delay of less than $27\mu s$. Commercially available PZT actuator patches were confirmed to possess the authority to control practical initial curvatures and perturbations of $0.1mm$ and $0.2ms^{-1}$, although the reduction in authority due to initial curvature correction required was not taken into account. The inclusion of mixed continuous-discrete control simulations for active laminate design was unique to this research and provided insight into many problems and interactions that occur when implementing a continuous control strategy in a discrete controlled real-time system.

Previous experimental research in the area of active buckling control has dealt with columns with buckling loads between 10 and 50N. These non-laminate isotropic columns were approximately 30 times more flexible than the laminate

plate strips used in this research. Lower stiffness also has the effect of reducing the dynamic frequencies of the structure, and hence the required controller bandwidth and delay.

A method has been developed for the manufacture of glass fibre reinforced polyester laminates achieving accurate thickness and a high quality surface finish. Embedding of actuators was attempted post-curing by machining a cavity in which actuators were bonded. Although the process worked well, the mechanical properties of the plate were adversely affected. This effect was most likely due to stress release during machining and weakness at the cavity walls.

Calibration of the test rig and active plate strip showed very close correlation with finite element models. Deflections were measured to within $2\mu m$ of the simulation results. This correlation confirms the accuracy of both the sensors and the static finite element model. Silicon strain gauges provided extremely high resolution measuring strains of $0.1\mu\varepsilon$ in the presence of noise. However, this high resolution resulted in a strain measurement range that proved too small for control purposes. Standard metal foil strain gauges were trialled, but with a resolution of around $7\mu\varepsilon$ they were not sensitive enough for control feedback. No commercially available strain gauges had intermediate gains and the majority of feedback control testing was performed using a capacitive displacement sensor, with a resolution of $2\mu m$.

Three active plate strips were constructed and a series of experiments carried out using a custom built compressive loading rig, which approximated fixed-free boundary conditions. Measured buckling loads for Plate Strip A, with embedded actuators, were substantially lower than predicted from finite element analysis. This premature buckling was caused both by the reduction in stiffness from the embedding process and small misalignments in the loading rig. Plate Strip B achieved buckling loads that were very close to the simulations after a constant

actuator correction for initial curvature had been applied.

The curvature corrected buckling behaviour of Plate Strip B closely resembled that of ideal buckling where the out-of-plane deflection remains almost zero until the buckling load is reached and then deflects suddenly with little increase in load. Active buckling control using strain feedback was only partially successful on Plate Strip B achieving an increase of 8%, as the majority of actuator authority was used to correct for initial curvature.

Active control of Plate Strip C proved more successful as the thicker actuators used provided a much larger actuator authority. These thick actuators were mounted on the surface of Plate Strip C which increased the passive column stiffness and hence buckling load by approximately 250N (17%) over a blank plate strip. A low bandwidth proportional controller and a high bandwidth proportional-derivative controller were tested and the latter increased the buckling load by 37% compared to the plate strip without initial curvature correction, and 17% compared to the case with initial curvature correction applied. Control gains for these specimens were found empirically due to instability from unknown interaction between the optimal gains and discrete control system hardware and software.

These active buckling control results are lower than those predicted in initial simulations. The reduction of actuator authority caused by the requirement for initial curvature correction was not considered in simulations. In some cases approximately 80% of the actuator authority was required for this initial curvature correction and simulations showed a dramatic reduction in system performance caused by this reduction in authority. In addition a curvature corrected plate is not a flat plate in terms of actual strain state. Finally, additional dynamics of the experimental hardware and time delays in excess of the simulated requirement resulted in further losses.

Frequency response functions were measured for various components of the unloaded experimental setup in order to gain an appreciation for how well the simulation model resembled the laboratory setup. This analysis was performed from 0 to 1.5kHz, where the lower vibration modes of the structure could be compared. The first mode displayed good correlation in both frequency and magnitude to the model. The second and third vibration modes had peaks at similar frequencies to the model, but the magnitude (width and height) of the peaks were lower in the simulation model. It can be concluded from this comparison that the simulation model displayed higher damping than the structure, for these three modes. The difference between the simulation model and structure becomes larger with increasing frequency. Lower damping results in lower stability margins for the controller. This reduction in stability is apparent in the phase plots where the simulation model boasts a phase margin of approximately 10 degrees, while for the measured structure it is approximately 0 degrees. These differences could also have been due to additional transport delays in the system hardware which were underestimated in the simulation model.

Overall, several small but critical differences between the simulation model and laboratory setup resulted in lower than expected controller performance. Control authority available to the controller was reduced through the need to correct for initial curvature in the plate strips. The designed controller was optimised to provide highest possible increase in buckling load, which places it close to the stability limit.

Chapter 12

Future work opportunities

Throughout the experimental phase of this research numerous issues have arisen, some of which merit further investigation. Two major difficulties that were encountered during experiments were the additional time delays and frequency responses of hardware in the feedback path, and perturbations in buckling mode development caused by laminate imperfections combined with loading rig misalignments. These issues will need to be addressed prior to continuing research into active buckling control of stiff laminates. The following avenues for further improvements and development are suggested.

12.1 Modelling and simulation

As damping can now be measured for the experimental specimen it would be advisable to update the damping model in the simulations so that it better resembles these measured values. Damping has a large effect on controller stability and partially dictates the required system bandwidth.

The simulation model assumed that modal amplitudes were estimated from strain or displacement sensors. A more accurate representation would be to use either strain or displacement feedback directly, therefore removing the assumption that conversions to modal amplitude could be accurately computed.

The transport delays through the DSP controller, PZT amplifier and sensor

signal conditioning have now been measured, and these updated values should be included. But, it would be better to include the frequency response functions for these items so as to achieve a closer representation of the experimental setup.

Reducing the actuator authority, due the requirement for initial curvature correction, would also be a closer representation of the experimental configuration as in some cases a substantial portion of the actuator authority was required to correct for initial curvature. Reducing the actuator authority will have a detrimental effect on the robustness of the controller.

12.2 Controller design

In the control optimisation process, more emphasis could be placed on minimising control effort and maximising damping, which will be at the cost of reducing the closed-loop buckling load. This would result in a controller with increased stability margins, able to tolerate larger discrepancies between simulation and experimental implementation. Increasing the phase margin to over 30 degrees is desirable.

12.3 Sensing architecture

Silicon strain gauges were found to be too sensitive for control purposes and standard metal foil gauges were not sensitive enough. Strain gauges with a gauge factor between 50 and 100 would provide the best solution for a control feedback signal with the conventional signal conditioning equipment. Another improvement in the sensing strategy would be to measure velocity directly, rather than differentiate a discrete displacement measurement. This would provide increased bandwidth, reduced phase lag, and lower noise. Integration of an acceleration sensor would also provide a signal with reduced noise compared to a differenti-

ated displacement signal.

Including additional sensors on the specimen to measure higher mode deflections would confirm the hypothesis that initial curvature and loading misalignments are causing complex higher mode deflections, which impacts the fundamental buckling behaviour of the specimen. It would also allow for the design of a controller that corrected for these complex initial deformations.

12.4 Actuators and imperfections

The embedding of actuator patches to achieve constant flexural stiffness was abandoned after a substantial reduction in the stiffness of the plate strip was found. Two possible solutions exist for this issue. First, the simulation model could be adapted to incorporate the surface mounted actuators, thus reestablishing consistency between the model and experimental specimen. The second solution would be to embed the actuators using a different method that reduced the impact on the stiffness of the surrounding laminate.

12.5 Laminate imperfections and loading misalignments

It has been concluded that higher mode deflections from laminate imperfections and loading misalignment have reduced the buckling load and performance of the active controller. The ability to both sense and actuate into these higher modes would at least confirm these conclusions and potentially overcome them.

Another method of reducing the impact of a second mode deflection would be to change the end boundary conditions from fixed to pinned. This would effectively reduce the stiffness of the first mode, therefore increasing the difference in stiffness between the lowest two modes and ease the development of a proper first mode buckle as load increases.

References

[1] Rao, V. and G. Singh, "A Smart Structures Concept for the Buckling Load Enhancement of Columns", *Smart Materials and Structures* **10(4)**, pp. 843-845, 2001.

[2] Chase, J.G. and S. Bhashyam, "Optimal Stabilization of Indefinite Plate Buckling Problems", *Smart Material and Structures* **10(4)**, pp. 786-793, 2001.

[3] Chase, J.G. and B. Smith, "Design of MEMS-based Stabilization for Buckling Constrained Structures", *Journal of Structural Stability and Dynamics* **1(4)**, pp. 467-484, 2001.

[4] Batra, R. and T. Geng "Enhancement of the dynamic buckling load for a plate by using piezoceramic actuators", *Smart Materials and Structures* **10(5)**, pp. 925-933, 2001.

[5] Varelis, D. and D. Saravanos, "Nonlinear Coupled Mechanics and Initial Buckling of Composite Plates with Piezoelectric Actuators and Sensors", *Smart Materials and Structures* **11(3)**, pp. 330-336, 2002.

[6] Thompson, S.P., J. Loughlan and H. Smith "Buckling control using Embedded Shape Memory Actuators and the Utilisation of Smart Technology in Future Aerospace Platforms", *Composite Structures* **58**, pp. 319-347, 2002.

[7] Mukherjee, A. and S. Chauduri, "Active Control of Dynamic Instability of Piezolaminated Imperfect Columns", *Smart Materials and Structures* **11(6)**, pp. 874-879, 2002.

[8] Sun, Bo-Hua, "Enhancement of Buckling Loads of Smart Structures", *Proceedings of 4th World Congress on Computational Mechanics (WCCM-IV)*, pp. 961-971, International Association of Computational Mechanics, Buenos Aires, Argentina, 1998.

[9] Berlin, Andrew A., *Towards Intelligent Structures: Active Control of Buckling*, Ph.D. Thesis in Electrical Engineering and Computer Science, Massachusetts Institute of Technology, 1994. (Also available as MIT Artificial Intelligence Laboratory Technical Report #1590)

[10] Berlin, Andrew A., "Active Control of Buckling using Piezo-Ceramic Actuators", *Industrial and Commercial Applications of Smart Structures Technologies*, Smart Structures and Materials SPIE Proceedings **2447**, pp. 141-154, SPIE, San Diego, 1995.

[11] Baz, A.M. and T. Chen, "Active Control of the Lateral Buckling of Nitinol-Reinforced Composite Beams", *Active Materials and Smart Structures,* SPIE Proceedings **2427**, pp. 30-48, SPIE, San Diego, 1995.

[12] Thompson, S.P. and J. Loughlan, "The Active Buckling Control of Some Composite Column Strips using Piezoceramic Actuators", *Composite Structures* **32**, pp. 59-67, 1995.

[13] Chase, J.G., A.A. Berlin, M.H. Yim, B.J. Maclean, M. Olivier and S.C. Jacobsen. "MEMS-Based Control of Structural Dynamic Instability", *Proc. of 1997 International Mechanical Engineering Congress & Exposition*, Dallas, TX, 1997.

[14] Berlin A.A., J.G. Chase, M.H. Yim, S.C. Jacobsen, M. Olivier, B.J. Maclean, "MEMS-based control of structural dynamic instability", *Journal of Intelligent Material Systems and Structures* **9**, pp. 574-586, 1998.

[15] Chase, J.G. and M. Yim, "Optimal Stabilization of Column Buckling", *Journal of Engineering Mechanics* **132**, pp. 987-993, 1999.

[16] Thompson, Danniella Muheim and O. Hayden Griffin Jr., "Finite Element Predictions of Active Buckling Control of Stiffened Panels", *Journal of Intelligent Material Systems and Structures* **4**, pp. 243-247, 1993.

[17] Ro, J. and A. Baz, "Nitinol-Reinforced Plates - II. Static and Buckling Characteristics", *Composites Engineering* **5**, pp. 77-90, 1995.

[18] Ro, J. and A. Baz, "Nitinol-Reinforced Plates - III. Dynamic Characteristics", *Composites Engineering* **5**, pp. 91-106, 1995.

[19] Birman, Victor, "Theory and Comparison of the Effect of Composite and Shape Memory Alloy Stiffeners on Stability of Composite Shells and Plates", *International Journal of Mechanical Sciences* **39**, pp. 1139-1149, 1997.

[20] Chandrashekhara, K. and K. Bhatia, "Active Buckling Control of Smart Composite Plates - Finite Element Analysis", *Smart Materials and Structures* **2**, pp. 31-39, 1993.

[21] Chase, J.G. and S. Bhashyam, "Optimal stabilization of plate buckling", *Smart Material and Structures* **8**, pp. 204-211, 1999.

[22] Shames, I. and C. Dym, "Energy and Finite Element Methods in Structural Mechanics", *Taylor & Francis*, pp. 597-639, 1991.

[23] Carey, M., *Dynamic Analysis of an Optical MEM's Device*, M.E. Thesis in Mechanical Engineering, University of Canterbury, 2002.

[24] Young, W., "Roarks's Formulas for Strss and Strain", *McGraw-Hill*, pp. 683-688, 1989.

[25] Boyd, S. and L. VandenBerghue, "Semidefinite Programming", *SIAM*, Philidelphia, PA, 1996.

[26] Boyd, S. and S. Wu, "sdpsol. User's Guide", Stanford University, Stanford, CA, 1996. Available from http://www.stanford.edu/~boyd/SDPSOL.html

[27] Cook, R., "Concepts and Applications of Finite Element Analysis. Second Edition", *John Wiley and Sons*, pp. 254, 1981.

[28] Humar, J.L., "Dynamics of Structures". Series in Civil and Engineering Mechanics, *Prentice Hall International*, 1990.

[29] Hull, D. and T.W. Clyne, "An Introduction to Composite Materials ", *Cambridge University Press*, 1996.

[30] Franklin G., D. Powell and A. Emami-Naeini, "Feedback Control of Dynamic Systems", *Addison-Wesley*, pp. 375-400, 1994.

[31] Chen Y.Q., "Dr YangQuan Chen's Digital Differentiator (DD) Webpage", *Utah State University*, Accessed 22/9/03. [http://www.csois.usu.edu/people/yqchen/dd/index.html]

Appendix A

Experimental loading rig details

A.1 Test rig clamp redesign

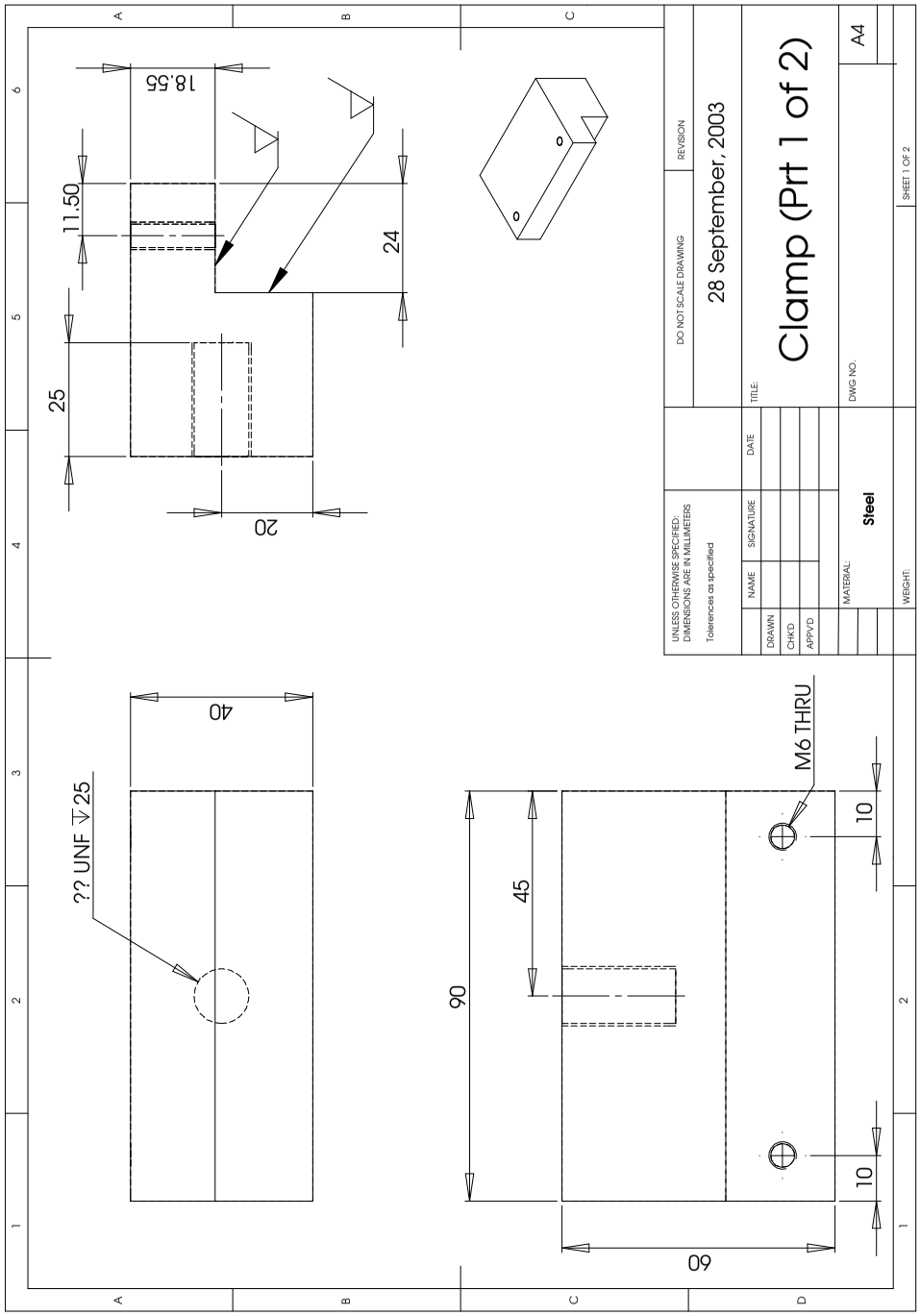

Figure A.1 Redesigned upper clamp (pg 1/2).

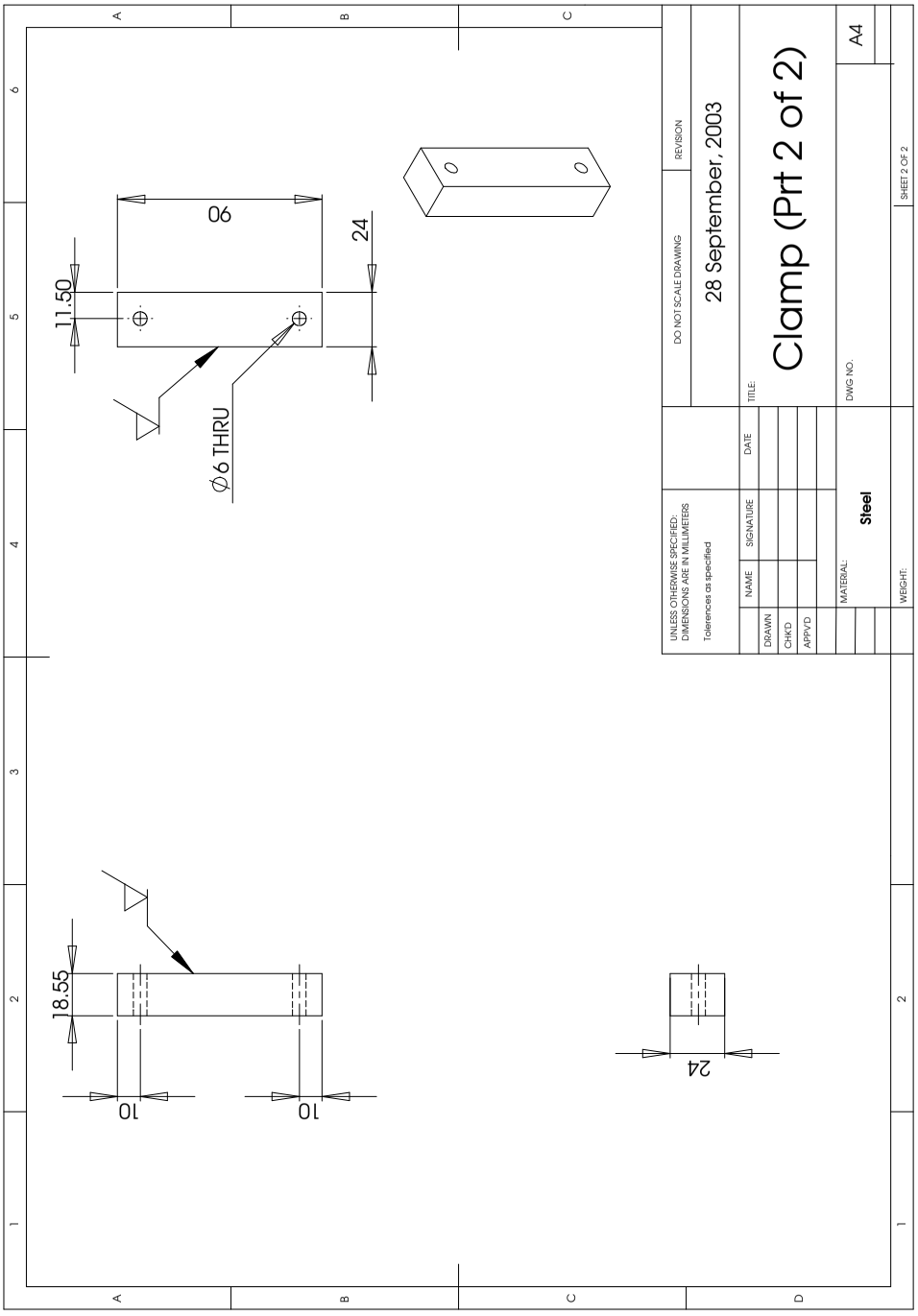

Figure A.2 Redesigned upper clamp (pg 2/2).

A.2 Hardware specifications and setup parameters

The following hardware calibration factors, offsets, electrical and mechanical operating ranges are required for setup of the test rig and control feedback loop.

Load cell

- Sensotec Model 41/572-01, S/N: 554502, [0-2000lbs], V_{EXC} = 10V DC
- Full strain bridge configuration
- Excitation = 10 Volts
- Resistance = 350 ohm
- Gauge Factor = 1.335
- P3500 Readout; 1ue = 1N
- Calibration (V to Newtons) = ×4350

LVDT crosshead displacement sensor

- Solartron DG-2.5, S/N: M922940B041-07
- Supply voltage = 10 Vdc (blue / red)
- Mechanical operating range = 0 to 6mm
- Voltage output range = -2.5V to 3v
- Calibration Factor (V to mm) = ×1.125

Capacitive sensor (OOP deflection at center)

- Bently Nevada 5mm Proximitor
- Scale Factor = 8.9 V / mm (using 1/3 voltage divider: 2.667 V/mm)
- Mechnical range = 2mm
- Output Range = -24 to -5 Volts
- Input range = 0 - 2 mm (set zero offset @ -3.80 Volts to get ±1mm)
- Supply voltage = -24V
- Calibration Factor (V to mm) = ×0.37

Laser distance sensor (OOP deflection at center)

- Banner LG5B65PI, 54712-12
- Supply voltage = 12-30 VDC (using 20V)
- Output voltage = 0.742 to 4.522 VDC (set zero offset @ 2.632 V)
- Mechanical range = 0-15mm
- Calibration factor (V to mm) = 3.97 @ 20V supply

Si strain gauges

- BLH Semiconductor SR-4 (SPB3-18-100)
- Gauge factor = 143.7
- Mechanical range = ± 83 ue (±5V output limit)
- 5B module amp factor = 500
- Excitation = 3.333 volts
- Calibration factor (V to $\mu\varepsilon$) = ×16.67

Metal foil strain gauges

- Micro Measurements S2K-00-125AC-10C
- Gauge factor = 2.04
- 5B module amp factor = 500
- Excitation = 3.333 volts
- Calibration factor (V to $\mu\varepsilon$) = ×1176.6

Pneumatic bellows

- Festo EB-145-60
- With bellows at 80mm extension, 1kPa = 7 Newtons applied force
- Calibration factor (Volts to kPa) = ×97

Midé PZT patches

- ACX Quickpak QP10W
- Input range = ±200 volts

- Theoretical max strain = ± 278 ue
- Capacitance = 0.1uF
- Max bending moment per node = 0.0462 Nm/node
- Calibration (Nm/node -/+ 10V Out to Amp) = ×21.65

Bending strain to modal amp conversion (QP10W actuators)

The following conversions are based on experimental data from the 1Hz 100V peak-to-peak (P2P) actuator calibration test:

Mode 1:

- Bending Strain 1 (BS1) + Bending Strain 2 (BS2) = 87 ue P2P
- Unit amplitude mode one creates 3.8mm central UZ.
- Measured to be 0.125mm for by applying 200V P2P.
- Conversion from (BS1+BS2) to Mode 1 Amp = $\frac{0.125}{87\times3.8}$ = 3.781E-4

A.3 Digital filter implementation coefficients

The following coefficients can be used to implement the digital filters designed in Section 9.4:

First order FIR derivative filter:

Num = [1]

Den = [1 -1]

Tenth order low pass FIR derivative filter:

Num = [1]

Den = [0.0355 0.0038 -0.0825 -0.1572 -0.1309 0 0.1309
0.1572 0.0825 -0.0038 -0.0355]

Second order Simpson and trapezoidal IIR derivative filter:

Num = [1 0.6378 0.1017]

Den = [0.8698 0 -0.8698]

Ninth order FIR smoothing (low pass) filter:

Num = [1]

Den = [0.1 0.1 0.1 0.1 0.1 0.1 0.1 0.1 0.1 0.1]

Second order IIR smoothing (low pass) filter:

Num = [1 0.51930 0.21965]

Den = [0.43474 0.86948 0.43474]